

A TWO-DIMENSIONAL MODEL FOR THE DYNAMICS OF GRANULAR AVALANCHES

Stefano De Toni



UNIVERSITÀ DEGLI STUDI DI TRENTO

Dipartimento di Ingegneria Civile
e Ambientale

2005

Based on the Doctoral thesis in Environmental Engineering (XVII cycle) defended in February 2005 at the Faculty of Engineering of Trento

Supervisor: Paolo Scotton

On the cover: The avalanche site of Lavina Granda Valley, Trento, Italy.

© Stefano De Toni (text and images, when not differently specified)

Direttore della collana: Marco Tubino

Segreteria di redazione: Laura Martuscelli

Dipartimento di Ingegneria Civile e Ambientale

Università degli Studi di Trento

Anno 2005

To my family.

“As early pioneers in the knowing,
that when you lose your reason,
you attain highest perfect knowing”
by Jack Kerouac.

Acknowledgements

I am thankful to Paolo Scotton for taking me as Ph. D. student, for his guidance and supervision, for his support in academic and scientific features, for the complete availability to place his knowledge, time and resources at my disposal.

I must express my gratitude to Mario Gallati and to Stefano Falappi of the Department of Hydraulic and Environmental Engineering of the University of Pavia, for their useful advices about the meshless methods, and to all the other guys of the Department, and in particular Federica Cappabianca and Matteo Pagliardi.

I am thankful to Enrico Bertolazzi of the Department of Mechanical and Structural Engineering of the University of Trento, for his support on numerical matters.

I am grateful to Mauro Barberi for his presence during the first field surveys at the avalanche site of Lavina Granda, for the knowledges and the experience in equipping avalanche sites he passed to me.

Field instrumentations, logistic support and important data have been supplied by the Snow, Avalanche and Meteorology Office of the Autonomous Province of Trento, in the persons of Mauro Gaddo, Mauro Mazzola and Giorgio Tecilla . My gratitude goes to them and to the Commune of Vigolo Vattaro and the District Forest Office of Pergine Valsugana, and in particular to Aldo Bianchini, for the logistic and technical support.

I would like to thank Ugo Helfer and the personnel of the Hydraulic Laboratory of the University of Trento, Andrea Bampi, Lorenzo Forti, Patrick Giovannelli, Fabio Sartori and Paolo Scarfiello, for their fundamental support in setting up the “avalanche chute” and all the instrumentations used in the field surveys.

Most of the data reported in the thesis have been collected in collaboration with students during the preparation of their thesis. My acknowledgments go to Samantha Benfatto, Ilaria Bezzi, Sabina De Biasio, Luca Musner, Daniele Rossi and Jacopo Sanfilippo.

All the people who took part to the surveys to the Lavina Granda site provided us a fundamental help. I would like to thank Giacomo Bertoldi, Alberto Bonomi, Valentina Broëll, Emiliano Casagrande, Stefano Serafin, Silvia Simoni and Fabrizio Zanotti among them.

Various groups and persons of the Department of Civil and Environmental Engineering gave their support to me. The hydrology group, and in particular Riccardo Rigon, Javier Yebrin, Silvia Franceschi, for the provided satellite ortho-photo and for the advices on Grass GIS; the topography group (Alfonso Vitti and Paolo Zatelli) and Marco Tubino for the lent instrumentations. Maurizio Righetti for the hints on the preparation of laboratory implements. I am very grateful to them and to the secretaries of the Department of Civil

and Environmental Engineering, Laura Martuscelli, Barbara Tognolli and Elena Uber, for helping in the administrative business.

To Maurizio Lutterotti, for sharing joys and sorrows of the doctorate, my gratitude.

Finally, I cannot forget the backing of my family, of the office-mates (Alessio, Andrea, Bruno, Doroteia, Giuseppe, Maddalena, Mahn, Marta, Martina, Oscar, Reza), of all the flat-mates of these last three years, of the friends of “GIM”, of “Volontari di Strada” and of all the homeless friends of Trento.

Contents

List of Figures	xxii
List of Tables	xxiv
List of Symbols	xxiv
1 Introduction	1
1.1 The physical and mathematical model	3
1.1.1 The hypotheses	3
2 A one-dimensional model with variable width	5
2.1 Introduction	5
2.2 The mathematical model	6
2.2.1 The mass balance equation	6
2.2.2 Momentum balance equations	7
2.2.3 Motion equations in non-dimensional form	9
2.2.4 The definition of the stress tensor	12
2.2.5 Motion equations averaged over η	18
2.2.6 Motion equations averaged over the section	19
2.3 The numerical model	22
2.4 Comparison of numerical results with experiments	24
2.4.1 Slump on horizontal plane	24
2.4.2 Double slope chute	28
2.4.3 Convex and concave curved chute	33
2.4.4 Concluding remarks	41
3 The two-dimensional model	43
3.1 The original model	43

3.1.1	The three-dimensional motion equations	43
3.1.2	Internal pressure distribution	44
3.1.3	Mohr–Coulomb closure	47
3.1.4	The integrated equations of motion	50
3.1.5	The numerical model	51
3.2	The orientation of the absolute coordinate system	52
3.2.1	Chute with a small lateral curvature	52
3.3	The definition of the secondary principal stress	58
3.3.1	Double slope unconfined chute	58
3.4	The distortion of the mesh	61
3.5	Final considerations	61
4	The application of meshless numerical methods	63
4.1	What are meshless methods?	63
4.1.1	The properties of the shape functions	67
4.1.2	Smoothed Particle Hydrodynamics (SPH) shape functions	67
4.1.3	Moving Least Square Particle Hydrodynamics (MLSPH) shape functions	69
4.2	The application of MLS approximants to the prediction of snow distribution	71
4.3	The MLSPH equations	80
4.4	A MLSPH one–dimensional model with constant width	84
4.4.1	The original equation of motion	84
4.4.2	The one–dimensional MLSPH equation of motion	86
4.4.3	Time integration	89
4.4.4	The initial condition	91
4.4.5	The time evolution of support domains	92
4.4.6	Comparison with experiments	92
	Convex and concave curved chute	92
4.4.7	Final remarks	99
5	Field activity	101
5.1	The Vigolana mountain range	101
5.2	The avalanche site of Lavina Granda	102
5.3	Available data	107
5.3.1	Avalanche registers and the Map of Likely Avalanche Location . . .	107
5.3.2	The starting zone	109
	The main features of the terrain: slope, aspect, vegetation	109

The assessment of initial volumes	112
5.3.3 The track	114
5.3.4 The runout zone	115
5.4 Monitoring of avalanche activity	118
5.4.1 Field instrumentations	118
5.4.2 The topographic surveys	121
The detailed topographic surveys	121
The quick topographic survey	123
5.4.3 Surveyed events	129
Winter season 2002–2003	129
Summer season 2003	129
Winter season 2003–2004	132
Autumn–winter 2004–2005	137
5.5 Final considerations	142
6 Concluding remarks	143
References	148

List of Figures

1.1	Granular deposit surveyed at the avalanche site of Lavina Granda, in mountainous range of Vigolana, close to Trento (Italy) (February 6 th 2004). . . .	2
2.1	The three-dimensional coordinate system.	6
2.2	Fluxes of mass.	7
2.3	The variation of \mathbf{g}_ξ and \mathbf{g}_ζ along ξ	8
2.4	Volume and surface forces on the infinitesimal curvilinear volume.	10
2.5	(Ξ, H) -local coordinate systems relevant to the orientation of the banks. .	13
2.6	The definition of the stress tensor components on the plane $\Xi\zeta$ according to the Savage–Hutter rheology (28).	14
2.7	The definition of the stress tensor components on the plane ΞH according to the Savage–Hutter rheology (28).	14
2.8	The curvilinear computational grid used to discretize the granular mass. . .	23
2.9	Slump on horizontal plane. Comparison of experimental data and numerical simulations produced by the one-dimensional models with constant width ($1d$) and variable width ($1dvar$), assuming no frictional interaction at lateral walls. The values of rheological parameters used in different simulations are shown in Table 2.1 and Table 2.2.	26
2.10	Slump on horizontal plane. Comparison of experimental data and numerical simulations produced by the one-dimensional models with constant width ($1d$) and variable width ($1dvar$), adding lateral friction at banks. The values of rheological parameters used in different simulations are shown in Table 2.1 and Table 2.2.	27
2.11	The experimental apparatus used by Hutter et al. (From (12)).	28
2.12	Initial shape of the granular mass.	29

2.13	Double slope chute. Positions of the front and the rear of the mass plotted versus time for <i>exp.29</i> . Comparison between experimental data and numerical simulations produced by the one-dimensional models with constant width (<i>1d</i>) and variable width (<i>1dwvar</i>), with no lateral friction at the lateral banks. The values of the rheological parameters used in different simulations are shown in Table 2.3 and Table 2.4. The curvilinear coordinate ξ is non-dimensionalized through $L_s = 0.149 m$, the initial length of the mass, time through $T_s = \sqrt{L_s/g} = 0.12 s$	31
2.14	Double slope chute. Positions of the front and the rear of the mass plotted versus time for <i>exp.29</i> . Comparison between experimental data and numerical simulations produced by the one-dimensional models with constant width (<i>1d</i>) and variable width (<i>1dwvar</i>), adding lateral friction at the lateral banks. The values of the rheological parameters used in different simulations are shown in Table 2.3 and Table 2.4. The curvilinear coordinate ξ is non-dimensionalized through $L_s = 0.149 m$, the initial length of the mass, time through $T_s = \sqrt{L_s/g} = 0.12 s$	32
2.15	Convex and concave curved chute. The bed inclination angle $\beta[^\circ]$ versus the absolute dimensional coordinate $x[mm]$. The circles highlight the positions of maximum and minimum slope along the bump.	36
2.16	Convex and concave curved chute. The bed geometry in the (x, y) -absolute dimensional coordinate system. The circles highlight the positions of maximum and minimum slope along the bump.	36
2.17	Convex and concave curved chute. <i>Exp.16</i> . Position of the front, the rear and the maximum height of the mass. Comparison of experimental data and numerical simulations of models <i>1d</i> and <i>1dwvar</i> , with the numerical parameters shown in Table 2.5 and Table 2.6. ξ is non-dimensionalized through $L_s = 0.375 m$, time t through $T_s = L_s/U_s = L_s/\sqrt{gH_s} = 0.42 s$, being $H_s = 0.08 m$	37
2.18	Convex and concave curved chute. <i>Exp.16</i> . Temporal evolution of the maximum depth of the granular mass. Comparison of experimental data and numerical simulations of models <i>1d</i> and <i>1dwvar</i> , with the numerical parameters shown in Table 2.5 and Table 2.6. h is non-dimensionalized through $H_s = 0.08 m$, time t through $T_s = L_s/U_s = L_s/\sqrt{gH_s} = 0.42 s$, being $L_s = 0.375 m$	38

2.19	Convex and concave curved chute. <i>Exp.29</i> . Comparison of experimental and numerical profiles obtained with models <i>1d</i> and <i>1dwvar</i> , with the numerical parameters shown in Table 2.5 and Table 2.6. h is non-dimensionalized through $H_s = 0.1\text{ m}$, ξ through $L_s = 0.3\text{ m}$, t through $T_s = L_s/U_s = L_s/\sqrt{gH_s} = 0.30\text{ s}$. The circles signal the positions of points of maximum and minimum slope.	39
2.20	Convex and concave curved chute. <i>Exp.36</i> . Comparison of experimental and numerical profiles obtained with models <i>1d</i> and <i>1dwvar</i> , with the numerical parameters shown in Table 2.5 and Table 2.6. h is non-dimensionalized through $H_s = 0.09\text{ m}$, ξ through $L_s = 0.33\text{ m}$, the time t through $T_s = L_s/U_s = L_s/\sqrt{gH_s} = 0.35\text{ s}$. The circles signal the positions of the points of maximum and minimum slope.	40
3.1	Absolute and curvilinear coordinate systems.	48
3.2	Local coordinate system $\Xi H\zeta$ relevant to the velocity vector, adopted to define the stress tensor.	48
3.3	Definition scheme of the stress tensor components in the coordinate system $\Xi H\zeta$	49
3.4	The triangular mesh which discretizes the fluid domain.	51
3.5	Comparison between experiment <i>V05</i> performed by Wieland et al. (1999) and numerical simulations obtained by correcting the bottom friction angle δ through equation (3.6). The values of the applied numerical parameters are shown in Table 3.1. All the geometrical dimensions are non-dimensionalized by h_c , the initial depth of the mass. β is the inclination angle of the thalweg line on the horizontal.	54
3.6	Comparison between experiment <i>V05</i> performed by Wieland et al. (1999) and numerical simulations obtained by adding an offset of 0.2 s to the time. The values of the applied numerical parameters are shown in Table 3.1. All the geometrical dimensions are non-dimensionalized by h_c , the initial depth of the mass. β is the inclination angle of the thalweg line on the horizontal.	55

3.7	Comparison between experiment <i>V05</i> performed by Wieland et al. (1999) and numerical simulations obtained applying the horizontal coordinate system and the coordinate system inclined at 40° . The values of the applied numerical parameters are shown in Table 3.1. All the geometrical dimensions are non-dimensionalized by h_c , the initial depth of the mass. β is the inclination angle of the thalweg line on the horizontal.	57
3.8	Experimental apparatus at the Hydraulic Laboratory of the Department of Civil and Environmental Engineering of the University of Trento.	58
3.9	The two-axial pneumatic moving system, carrying a laser distance sensor, used to automatically map the final deposit of experiments performed on the double-slope unconfined chute at the Hydraulic Laboratory of the University of Trento.	59
3.10	Comparison between experimental data, collected at the Hydraulic Laboratory of the University of Trento, and numerical simulations (plan, longitudinal section and amplified (factor 5) longitudinal section at $y/R = -0.023$). Simulation <i>DT.2d.1</i> is obtained applying Hutter's approach to the calculation of p_{HH} (equation (3.5)). In simulation <i>DT.2d.2</i> it is assumed $p_{HH} = p_1$. All geometrical dimensions are non-dimensionalized by R , the lower base radius of the truncated conical holder (Figure 3.8), equal to 21.8 cm.	60
3.11	The distortion of the mesh when the mass collides with a dihedral obstacle. From Musner (22).	61
4.1	The definition of the support domain centered in the point of interest \mathbf{x} . Both the nodes 1 and 2 are included in the support domain of the point of interest.	66
4.2	The definition of the influence domain for nodes 1 and 2. The point of interest is contained in the influence domain of node 1, but is excluded from the influence domain of node 2.	66
4.3	The incorrect parabolic extrapolation at low values of z (continuous line), when known nodes (empty circles) are absent in that region. Adding the fictitious node represented by the filled circle, the approximation retains a monotone trend in the whole region of interest (dashed line).	73

4.4	Digital Elevation Model of the Province of Trentino (Italy), with the snow and meteorologic stations used for the estimation of the snow distribution. Identifiers of stations are indicated in Table 4.1. The stations marked with the symbol indicated in the legend are excluded from computations, because they have no snow depth measure on January 10 th 2004.	77
4.5	The snow distribution evaluated by MLS approximants, using a linear polynomial base and varying s up to have at least 4 neighboring nodes for each calculation point.	77
4.6	The snow distribution evaluated by MLS approximants, using a quadratic polynomial base and varying s up to have at least 11 neighboring nodes for each calculation point.	78
4.7	The snow distribution evaluated by MLS approximants, using a quadratic polynomial base and varying s up to have at least 11 neighboring nodes for each calculation point. 5 fictitious stations are indicated on the map through red crosses. They have been introduced in order to correct the increase of snow depth at low altitudes due to the quadratic trend in absence of known values of snow depth along the valley floors. The snow depth assigned to these fictitious nodes is 0.	78
4.8	The snow distribution evaluated by MLS approximants, using a base mildly non-linear, varying s to have at least 11 neighboring nodes for each calculation point.	79
4.9	The snow distribution evaluated by MLS approximants, , with s constant ($= 17000 m$), using a variable base order. The position of the snow stations is indicated through red crosses.	79
4.10	The dependence of the artificial viscosity Π_{ij} on ξ_{ij} (from (22))	89
4.11	Convex and concave curved chute. <i>Exp.29</i> . Comparison of experimental and numerical profiles obtained with the one-dimensional MLSPH model and with the original finite difference one-dimensional model. The comparison is between the numerical simulations <i>g29.mlsph1d.2</i> , characterized by the parameters reported in Table 4.3 and <i>g29.1d.2</i> , reported in Table 2.5. h is non-dimensionalized through $H_s = 0.1 m$, ξ through $L_s = 0.3 m$, t through $T_s = L_s/U_s = L_s/\sqrt{gH_s} = 0.30 s$. Circles signal the positions of points of maximum and minimum slope.	95

4.12	Convex and concave curved chute. <i>Exp.29</i> . Comparison of experimental and numerical profiles obtained with the one-dimensional MLSPH model. The comparison is between the numerical simulation <i>g29.mlsph1d.3</i> and <i>g29.mlsph1d.2</i> , characterized by the parameters indicated in Table 4.3. Both the simulations have the same value of α_s . The artificial viscosity is introduced in simulation <i>g29.mlsph1d.3</i> . h is non-dimensionalized through $H_s = 0.1 m$, ξ through $L_s = 0.3 m$, t through $T_s = L_s/U_s = L_s/\sqrt{gH_s} = 0.30 s$. Circles signal the positions of points of maximum and minimum slope.	96
4.13	Convex and concave curved chute. <i>Exp.29</i> . Comparison of experimental and numerical profiles obtained with the one-dimensional MLSPH model. The comparison is between the numerical simulations <i>g29.mlsph1d.1</i> and <i>g29.mlsph1d.2</i> , characterized by the parameters reported in Table 4.3. Both the simulations are without viscosity. The simulation <i>g29.mlsph1d.1</i> has $\alpha_s = 10$, <i>g29.mlsph1d.2</i> has $\alpha_s = 3$. h is non-dimensionalized through $H_s = 0.1 m$, ξ through $L_s = 0.3 m$, t through $T_s = L_s/U_s = L_s/\sqrt{gH_s} = 0.30 s$. Circles signal the positions of points of maximum and minimum slope.	97
4.14	Convex and concave curved chute. <i>Exp.29</i> . Comparison of experimental and numerical profiles obtained with the one-dimensional MLSPH model. The comparison is between the numerical simulations <i>g29.mlsph1d.4</i> and <i>g29.mlsph1d.2</i> , characterized by the parameters reported in Table 4.3. In the simulation <i>g29.mlsph1d.4</i> the number of base function is incremented to 3, against the 2 base function of simulation <i>g29.mlsph1d.2</i> . The simulation <i>g29.mlsph1d.4</i> has $\alpha_s = 6$, while <i>g29.mlsph1d.2</i> has $\alpha_s = 3$. h is non-dimensionalized through $H_s = 0.1 m$, ξ through $L_s = 0.3 m$, t through $T_s = L_s/U_s = L_s/\sqrt{gH_s} = 0.30 s$. Circles signal the positions of points of maximum and minimum slope.	98
5.1	The Vigolana range and the Lavina Granda Valley on the black and white ortho-photo of 1994.	103
5.2	The Digital Elevation Model with resolution of 10 m of the Lavina Granda valley.	104
5.3	The slope map. The slope angle is measured in sexagesimal degrees on the horizontal.	105
5.4	The aspect map. The aspect angle is measured in counterclockwise sexagesimal degrees from east.	106

5.5	The deposit of a granular avalanche in Lavina Granda site (January 16 th 2004).	108
5.6	The effects of a powder avalanche in Lavina Granda site (March 21 st 2004).	108
5.7	Map of Likely Avalanche Location. From Autonomous Province of Trento (http://www.gis.provincia.tn.it/).	108
5.8	The steep slope below the Madonnina Refuge (December 12 th 2004).	110
5.9	The slope map of the starting zone. The slope angle is measured in degrees on the horizontal. The assumed two sub-catchments are delimited by the white line.	111
5.10	The ortho-photo of the starting zone, with the two assumed sub-catchments, delimited by the yellow and the red lines.	112
5.11	The altimetric profile of the channel, the trend of the width and of the slope angle vs. the horizontal cumulative distance. They have been obtained through the analysis of the ortho-photo, of the DEM and of the Provincial Technical Map.	116
5.12	6 different paths of the avalanche on the alluvial fan, used for the numerical simulations. Plan view and altimetric profiles	117
5.13	The two graduated poles, located in the two sub-catchments in order to estimate the snow depth in the starting zone (October 29 th 2002).	118
5.14	The coloured tracers, spread over the two sub-catchments in order to monitor the avalanches flowing paths (October 29 th 2002).	119
5.15	The chronographs placed along the channel in order to measure the avalanches flowing velocity (December 6 th 2002).	120
5.16	The flowing depth measuring section equipped at the second chronograph (December 6 th and 18 th 2002).	120
5.17	The theodolite for the measure of inclined distances, zenith angles and azimuth distances.	121
5.18	The snow depth distribution, obtained through the elaboration of the data of the two detailed topographic surveys, carried out along the segment of the Lavina Granda channel, above the lower dirt road at the altitude of 1110 <i>m a.s.l.</i> . The points of the winter topographic survey are represented through red crosses. The contour lines derive from the Digital Terrain Model obtained from the summer survey.	122

5.19	The comparison between the morphology of the channel at the end of the autumn (December 18 th 2002) and after the passage of an avalanche (January 16 th 2004), in the segment between the intermediate and the upper chronographs.	123
5.20	The comparison between the morphology of the channel in autumnal conditions (November 5 th 2004) and in snowy conditions (January 2 nd 2005), about the cliffs just below the lower chronograph.	124
5.21	Survey of distance between two points on the thalweg is performed by means of a laser distancemeter; the measurement of the angle on the vertical plane is performed by means of a clinometer; the angle on the horizontal plane is measured by means of a compass.	126
5.22	Survey of the cross-sections, performed by means of a laser distancemeter and of a clinometer.	126
5.23	Compass (on the left) and clinometer (on the right) for the measure of the angle on the horizontal plane (Figure 5.21, on the left) and the angle on the vertical plane (Figure 5.21, on the right).	127
5.24	A 3-D view of Lavina Granda bottom survey, realised on July 29 th 2004.	127
5.25	Slope profiles along the Lavina Granda avalanche channel, in the case of the summer survey (July 29 th 2004) and in the case of the winter survey (May 21 st 2004).	128
5.26	Comparison of the slope profiles along the Lavina Granda avalanche channel, obtained from the summer survey (July 29 th 2004) and the Digital Elevation Model (DEM).	128
5.27	The morphologic evolution in the initiation zone of the debris flow. The two images show the same channel in autumn 2002 (October 29 th 2002) and in summer 2003 (July 18 th 2003).	130
5.28	An intermediate deposit of the debris flow, at the intersection between the channel and the dirt road at the altitude of 1280 <i>m a.s.l.</i> (August 10 th 2003).	130
5.29	Erosion and lateral depositions due to the debris flow along the channel (July 18 th 2003).	130
5.30	The feeding areas and the paths of the debris flow of the summer 2003.	131
5.31	The final deposit of the avalanche that occurred on December of 2003, at the altitude of 1110 <i>m a.s.l.</i> (January 16 th 2004).	132
5.32	The maximum flowing depth for the granular avalanche occurred on December (photo taken on January 16 th 2004).	132

5.33	The tree debris transported by the powder avalanche. Entire plants have been uprooted (May 12 th 2004).	133
5.34	The signs of the powder avalanche on the left side of the channel, opposite the third chronograph, at the altitude of 1400 <i>m a.s.l.</i> . All the trees are bended downstream (March 21 st 2004).	133
5.35	The two edges of the iron cable, torn by the powder avalanche at the flowing depth measuring section, in the Lavina Granda channel (May 12 th 2004).	134
5.36	A satellite image, dated March 30 th 2004, where are recognizable the area interested by the powder avalanches in Lavina Granda and Lavinella sites.	135
5.37	The runout zone of the avalanche that occurred in the Lavinella channel. In the background the uprooted beech plants are recognizable (March 21 st 2004).	135
5.38	The final granular deposit of the avalanche that flew down at the beginning of May of 2004 (May 12 th 2004).	135
5.39	The locations of the final deposits of the 4 avalanches occurred during the winter season 2003–2004. In green the granular avalanche of December 2003; in yellow the granular avalanche of February 2004; in red the powder avalanche of March 2004; in cyan the granular avalanche of May 2004.	136
5.40	The debris flow deposit that formed opposite the intermediate chronograph during the event of the November 2004 (November 5 th 2004).	137
5.41	A rotational ground failure at the base of the dirt road at the altitude of 1110 <i>m a.s.l.</i> , occurred during the debris flow event of the November 2004 (November 5 th 2004).	137
5.42	The crown fractures of two slab avalanches, started in the right sub-catchment. In the lower picture the graduated pole is recognizable (December 12 th 2004).	138
5.43	The fraction line of a slab avalanche not still triggered (December 12 th 2004).	138
5.44	Aggregate of particles of a previous deposit, entrained but not broken up by the avalanche of the end of December (January 2 nd 2005).	140
5.45	The full sliding sections at the lower chronograph (January 2 nd 2005).	140
5.46	The external face of the lateral bank, inclined at ϕ on the horizontal (January 2 nd 2005).	140
5.47	The sub-vertical smooth lateral bank left by the avalanche at the upper dirt road 1280 <i>m a.s.l.</i> . The flowing depth is about 3 <i>m</i> (January 2 nd 2005).	140

5.48	A slab-type movement of the granular material deposited by the avalanche along the channel. The smooth sliding bottom appears on the surface (January 2 nd 2005).	140
5.49	The locations of the final deposits of the 2 avalanches occurred during the winter season 2004–2005. In yellow the granular avalanche of the beginning of December 2004; in red the granular avalanche of the end of December 2004.	141

List of Tables

2.1	Values of the rheological parameters used in the numerical simulations of the experiments of D'Accordi (4) with the one-dimensional model with constant width ($1d$). ϕ is the internal friction angle, δ the bottom friction angle, k the coefficient of the corrective factor of δ proposed by Savage and Hutter (28) (see equation (2.18)).	25
2.2	Values of the rheological parameters used in the numerical simulations of the experiments of D'Accordi (4) with the one-dimensional model with variable width ($1dwvar$). ϕ is the internal friction angle, δ_b the bottom friction angle, δ_l and δ_r are the lateral friction angles at the left and right sides respectively.	25
2.3	Values of the rheological parameters used in the numerical simulations of the experiment of Hutter et al. (12) with the one-dimensional model with constant width ($1d$). ϕ is the internal friction angle, δ the bottom friction angle, k the coefficient of the corrective factor of δ proposed by Savage and Hutter (28) (see equation (2.18)).	29
2.4	Values of the rheological parameters used in the numerical simulations of the experiment of Hutter et al. (12) with the one-dimensional model with variable width ($1dwvar$). ϕ is the internal friction angle, δ_b the bottom friction angle, δ_l and δ_r are the lateral friction angles at left and right sides respectively.	30
2.5	Values of the rheological parameters used in the numerical simulations of the experiments of Greve and Hutter (10) with the one-dimensional model with constant width ($1d$). ϕ is the internal friction angle, δ the bottom friction angle, k_w the coefficient of the corrective factor of δ proposed by Greve and Hutter (10) (see equation (2.19)), k the coefficient of the corrective factor of δ proposed by Savage and Hutter (28) (see equation (2.18)).	34

2.6	Values of the rheological parameters used in the numerical simulations of the experiments of Greve and Hutter (10) with the one-dimensional model with variable width (<i>1dvwvar</i>). ϕ is the internal friction angle, δ_b the bottom friction angle, δ_l and δ_r the lateral friction angles at left and right sides respectively.	34
3.1	The values of the parameters which characterize the different numerical simulations of experiment V05, described in Wieland (34). m_δ is the coefficient of the corrective term of the bottom friction angle δ , represented by equation (3.6). Time offset represents the delay introduced in the numerical simulation. β_r is the inclination on the horizontal of the rotated coordinate system.	53
4.1	The list of snow and meteorologic stations in Trentino, used for the elaborations. For each station the identifier used in Figure 4.4, the name, the elevation above mean sea level, the measured snow depth on the 10 th of January of 2001 are reported.	76
4.2	The standard and the mean deviation of the residuals and the computed volume for different types of MLS approximants.	76
4.3	The numerical parameters characterizing the simulations performed with the model <i>mlsph1d</i> . All the other parameters are the same for all the simulations: the number of nodes $n = 40$, the coefficients of time step corrections $\tau_u = 0.2$, $\tau_f = 0.1$, $\tau_c = 0.2$. The physical parameter are $\phi = 37^\circ$, $\delta = 26.5^\circ$ and $k = 0.4$. It is to point out that k , the corrective factor used to keep into account the lateral friction, is the one proposed by Savage and Hutter (28) (see equation (2.18)).	93
5.1	The distinction between different types of avalanches occurring at different slope angles of the mountainside.	109

List of Symbols

δ the bottom friction angle [$^\circ$];

δ_i^j the Kronecker delta;

$\delta(\mathbf{x})$ the Dirac delta function;

Δt the computational time step [s];

$\partial\Omega$ the boundary of the spatial domain;

ε the ratio between depth scale and longitudinal scale;

Γ the boundary of the spatial domain;

Γ_{ij}^k the Christoffel symbols [1/m];

ν linear particle concentration;

ρ the bulk density of the granular material [kg/m^3];

ρ_p the particle density [kg/m^3];

ρ_s the density scale [kg/m^3];

σ the particle diameter [m];

ϕ the internal friction angle [$^\circ$];

ϕ_d the dynamic internal friction angle [$^\circ$];

ϕ_s the static internal friction angle [$^\circ$];

Ω the spatial domain;

$\nabla \cdot$ the divergence operator [1/m];

∇ the gradient operator $[1/m]$;
 ∇_k the covariant derivative with respect to the coordinate x_k $[1/m]$;
 f_1 function of the granular concentration;
 f_2 function of the granular concentration;
 Fr_s the Froude number scale;
 g the modulus of the gravity acceleration vector $[m/s^2]$;
 \mathbf{g} the gravity acceleration vector $[m/s^2]$;
 h the flow depth $[m]$;
 H_s the depth scale $[m]$;
 $k_{a/p}$ the active/passive stress coefficient;
 k_{ij} the stress coefficient relevant to the surface normal to i , in the direction j ;
 L_s the longitudinal length scale $[m]$;
 \mathbf{n} outward normal unit vector;
 p_{ij} the component of the stress tensor relevant to the surface normal to i , in the direction j $[N/m^2]$;
 p_s quasi-static contribution to the normal stress $[N/m^2]$;
 P_s the pressure scale $[N/m^2]$;
 \mathbf{P} the stress tensor $[N/m^2]$;
 \hat{q} the generic variable q non-dimensionalized;
 q_b the generic variable q evaluated at the bottom surface;
 q_h the generic variable q evaluated at the free surface;
 q_i the variable q evaluated at the grid node identified by i ;
 $q_{,x}$ the partial derivative of the variable q with respect to the generic coordinate x ;
 q^n the variable q evaluated at the n^{th} calculation instant;

t the time [s];
 T_s the time scale [s];
 u_η the component of the velocity vector along η [m/s];
 u_ξ the component of the velocity vector along ξ [m/s];
 u_ζ the component of the velocity vector along ζ [m/s];
 \mathbf{u} the velocity vector [m/s];
 U_s the scale for the velocity modulus [m/s];
 $U_{\eta s}$ the scale for velocity along η [m/s];
 $U_{\xi s}$ the scale for velocity along ξ [m/s];
 $U_{\zeta s}$ the scale for velocity along ζ [m/s];
 \mathbf{x} the position vector of a generic point in the spatial domain [m];

The one-dimensional model with variable width

$(\alpha)_{l/r}$ the inclination of the left/right bank with respect to the direction ξ [°];
 β the local slope angle of the channel [°];
 δ_{eff} the bottom friction angle corrected in order to take account of the friction at the lateral sides [°];
 η the coordinate of the curvilinear coordinate system orientated along the channel section [m];
 H the coordinate of the local ortho-normal coordinate system normal to the lateral side wall [m];
 λ the ratio between longitudinal scale and curvature radius scale;
 ξ the coordinate of the curvilinear coordinate system orientated along the channel [m];
 Ξ the coordinate of the local ortho-normal coordinate system tangential to the lateral side wall [m];
 χ the local curvature of the bottom [1/m];

- ζ the coordinate of the curvilinear coordinate system orientated normally to the bottom
[m];
- b the width of the channel, function of ξ [m];
- B_s the transversal length scale [m];
- \mathbf{g}_η the unit vector that defines the local orientation of η ;
- \mathbf{g}_ξ the unit vector that defines the local orientation of ξ ;
- \mathbf{g}_ζ the unit vector that defines the local orientation of ζ ;
- k parameter of the correction factor of the bottom friction angle δ [$1/m$];
- $k_{a/p}^H$ the active/passive stress coefficient, relevant to the plane ΞH .
- $k_{a/p}^\zeta$ the active/passive stress coefficient, relevant to the plane $\Xi\zeta$;
- K_{ij} the stress coefficient relevant to the surface normal to i , in the direction j , averaged
over the entire section;
- k_w parameter of the correction factor of the bottom friction angle δ [$^\circ$];
- k_{wall} parameter of the correction factor of the bottom friction angle δ [$1/m$];
- N the number of cells of the numerical grid that discretizes the granular mass;
- P_{ij} the component of the stress tensor relevant to the surface normal to i , in the direction
 j , averaged over the entire section [N/m^2];
- \bar{q} the generic variable q averaged over η ;
- $q_{i+1/2}$ the variable q evaluated at the midpoint between the grid nodes i and $i + 1$;
- q_l the generic variable q evaluated on the left side of the rectangular channel;
- q_r the generic variable q evaluated on the right side of the rectangular channel;
- $\tilde{\mathbf{Q}}$ the generic tensor \mathbf{Q} defined in the local coordinate system (Ξ, H) ;
- R the local curvature radius of the bottom [m];
- R_s the scale for the curvature radius of the bottom [m];

U_η the component along η of the velocity vector averaged over the entire section [m/s];
 U_ξ the component along ξ of the velocity vector averaged over the entire section [m/s];
 U_ζ the component along ζ of the velocity vector averaged over the entire section [m/s];
 $V_{i+1/2}$ the volume of granular material included between the grid nodes i and $i + 1$ [m³].
 x the horizontal coordinate of the absolute ortho-normal coordinate system lying on the vertical plane containing ξ and ζ [m];
 y the horizontal coordinate of the absolute ortho-normal coordinate system normal to the vertical plane containing ξ and ζ [m];
 z the vertical coordinate of the absolute ortho-normal coordinate system [m];

The two-dimensional model

δ_0 the bottom friction angle at the front [°];
 η coordinate of the curvilinear coordinate system defined by the intersection between the basal surface and the plane normal to x [m];
 H the coordinate of the ortho-normal coordinate system normal to ζ and to the velocity vector [m];
 ζ coordinate of the curvilinear coordinate system normal to the basal surface [m];
 b the elevation of the bottom above the plane xy [m];
 f the elevation of the free surface above the plane xy [m];
 \mathbf{f} the external force per unit volume [kg/m²/s²];
 \mathbf{g}_η the “cellar” base vector that defines the local direction of the coordinate line η ;
 \mathbf{g}_ξ the “cellar” base vector that defines the local direction of the coordinate line ξ ;
 \mathbf{g}_ζ the “cellar” base vector that defines the local direction of the coordinate line ζ ;
 \mathbf{g}^η the “roof” base vector relevant to coordinate η ;
 \mathbf{g}^ξ the “roof” base vector relevant to coordinate ξ ;
 \mathbf{g}^ζ the “roof” base vector relevant to coordinate ζ ;

h_i the depth defined at the generic triangle i of the mesh [m];
 k_1 the maximum principal stress coefficient;
 k_2 the intermediate principal stress coefficient;
 k_3 the minimum principal stress coefficient;
 m_δ the parameter for the corrective term of the friction angle δ [$^\circ/m$];
 p_1 the maximum principal stresses [N/m^2];
 p_2 the intermediate principal stresses [N/m^2];
 p_3 the minimum principal stresses [N/m^2];
 q_f the generic variable q evaluated at the free surface;
 q_i the i^{th} “cellar” component of the generic vector \mathbf{q} ;
 q_{ij} the generic “cellar” component of the tensor \mathbf{Q} ;
 q^i the i^{th} “roof” component of the generic vector \mathbf{q} ;
 q^{ij} the generic “roof” component of the tensor \mathbf{Q} ;
 $q^{(i)}$ the i^{th} “physic” component of the generic vector \mathbf{q} ;
 $q^{(ij)}$ the generic “physic” component of the tensor \mathbf{Q} ;
 $\tilde{\mathbf{Q}}$ the generic tensor \mathbf{Q} defined in the local coordinate system (Ξ, H, ζ) ;
 U_x the component along x of the velocity vector averaged over z [m/s];
 U_y the component along y of the velocity vector averaged over z [m/s];
 \mathbf{U}_j the velocity vector defined at the generic vertex of the mesh j [m/s];
 x horizontal coordinate of the absolute coordinate system [m];
 x_n the x coordinate of the front of the granular mass [m];
 x_r the x coordinate of the rear of the granular mass [m];
 y horizontal coordinate of the absolute coordinate system [m];
 z vertical coordinate of the absolute coordinate system [m];

Meshless methods

α_s the dimensionless size of the support domain;

ϕ_i the meshless shape function relevant to node i ;

$\nabla_j \phi_i$ the gradient of the i^{th} shape function evaluated at the node j $[1/m]$;

a_i the i^{th} coefficient of the linear combination used to approximate a generic field variable;

\mathbf{a} the set of coefficient a_i ;

\mathbf{A} the system matrix of the MLS approximants;

A_s the initial estimation of the support domain area in two dimensions;

\mathbf{B}_i the i^{th} known term of the system of the MLS approximants;

\mathbf{B} the set of known terms of the system of the MLS approximants;

d_c characteristic length associated to the nodal spacing $[m]$;

d_i the influence domain size $[m]$;

d_s the support domain size $[m]$;

D_s the initial estimation of the support domain size in one dimension $[m]$;

\mathbf{D} the re-normalization matrix;

\mathbf{E} the inverse of the re-normalization matrix;

J the weighted summation of the squared residuals, minimized in the MLS approach;

m the number of base functions;

n the number of computational nodes;

n_{A_s} the number of nodes covered by the domain of size A_s in two dimensions;

n_{D_s} the number of nodes covered by the domain of size D_s in one dimension;

n_{V_s} the number of nodes covered by the domain of size V_s in three dimensions;

p_i the i^{th} base function;

\mathbf{p}^T the set of base functions $p_i(\mathbf{x})$;

q_i the value of the generic variable q at the node i ;
 q^s the approximated value of the generic field variable q through the use of meshless shape functions depending on the parameter s ;
 \mathbf{q} the set of known value q_i of the field variable q ;
 r_i the distance of the generic point \mathbf{x} from node i , non-dimensionalized through s ;
 s the smoothing length [m];
 V_i the volume associated to the generic node i [m^3];
 V_s the initial estimation of the support domain volume in three dimensions [m^3];
 W the kernel or weight or smoothing function;
 $x^{(k)}$ the k^{th} spatial variable [m];

The MLSPH one-dimensional model with constant width

α_v parameter of the artificial viscosity ;
 β the slope angle of the channel [$^\circ$];
 β_v parameter of the artificial viscosity;
 $\partial Q(\cdot)$ the surface quadrature rule;
 γ_v parameter of the artificial viscosity;
 λ the ratio between longitudinal scale and curvature radius scale;
 μ_{ij} factor of the artificial viscosity [m/s];
 ξ the coordinate of the curvilinear coordinate system orientated along the slope [m];
 Π_{ij} the artificial viscosity term relevant to nodes i and j [m^2/s^2];
 τ_a coefficient for the definition of the time step bound relevant to the acceleration;
 τ_c coefficient for the definition of the time step bound relevant to the celerity;
 τ_u coefficient for the definition of the time step bound relevant to the velocity;
 ζ the coordinate of the curvilinear coordinate system normal to the bottom [m];

a_i the MLSPH acceleration of node i [m/s^2];
 A_i the constant area of particle i [m^2];
 \mathcal{B} the set of boundary nodes;
 B_{ij} coefficient of the flux terms in the MLSPH equations;
 c_i the celerity of the generic node i [m/s];
 C_{ij} coefficient of the flux terms in the MLSPH equations;
 dA the infinitesimal surface element on the boundary of the domain $\Gamma = \partial\Omega$ [m^2];
 \mathbf{f} the source/sink term in the hydrodynamic equations of motion;
 \mathbf{F} the flux term in the hydrodynamic equations of motion;
 \mathcal{G} the driving gravitational force [m^2/s^2];
 h_i^0 the initial depth of the granular mass at node i [m];
 l_i the numerical particle length of node i [m];
 l_i^0 the initial length associated to node i [m];
 l_{tot}^0 the initial total length of the granular mass [m];
 P_{ij} the depth averaged stress tensor components [N/m^2];
 q_b the generic variable q evaluated at the bottom;
 q_h the generic variable q evaluated at the free surface;
 \mathcal{P} the stress flux term [m^3/s^2];
 $Q(\cdot)$ the volume quadrature rule;
 R_s the curvature radius scale [m];
 \mathcal{R} the resistance term of the momentum balance [m^2/s^2];
 s_i^0 the initial dimension of the support domain of node i [m];
 u_ξ the component along ξ of the velocity vector [m/s];

U_ξ the depth averaged component along ξ of the velocity vector [m/s];

u_ζ the component along ζ of the velocity vector [m/s];

\mathbf{y} the vector of conserved quantities in the typical hydrodynamic equations of motion;

$\mathbf{y}_{(k)}$ the unknown vector \mathbf{y} evaluated at the k^{th} try of the numerical iterative procedure;

Field activity

β_0 mean slope angle of the starting zone [$^\circ$];

ρ_a the density of the air [kg/m^3]

ρ_s the density of the snow [kg/m^3]

dw the snow drift [m];

C the volume concentration of the snow;

f corrective factor of h_0^* to take into account the effect of the slope;

h_0 snow depth in the starting zone [m];

h_o^* snow depth at the altitude of 2000 *m a.s.l.* [m];

z elevation above the sea level [*m a.s.l.*];

1 Introduction

The zoning of hydrogeological risk areas is one of the main tasks of land-use planning in alpine areas. Snow avalanches are natural phenomena which can seriously affect human settlements in mountainous regions. In Italy avalanche historical databases collect records of avalanche events only since a short period of time and the low frequency of avalanches in some sites makes it difficult to perform a statistical analyses of these data. Old documents, interviews with the inhabitants, dendrochronological analysis supply further informations, useful for avalanche risk area mapping. Simulations made with physical and mathematical models can improve the knowledge of the dynamics of these events. For given topography, bed roughness and initial characteristics of the snow mass (volume, initiation zone, material properties), physical and mathematical models can be used to estimate the final deposit configuration, impact forces on obstacles and other dynamic parameters.

In this thesis, three different mathematical and numerical models, based on the rheological theory of Savage and Hutter (28) for granular flows, are introduced. The choice of this type of rheology is justified by the consideration that the vast majority of snow avalanches, which take place in alpine regions, are granular avalanches (see Figure 1.1).

In chapter §2, a one-dimensional model with variable width, suitable for the simulation of confined avalanches, is described. It has been implemented in a curvilinear coordinate system. New rheological hypotheses have been introduced in order to describe the frictional interaction with vertical sides. The model has been tested against experimental data relevant to cases with constant width, collected in literature.

In chapter §3, the two-dimensional model, implemented by the writer during his degree thesis, has been developed. It was originally written in a horizontal coordinate system, assuming a linear stress tensor distribution and the constancy of the velocity along the vertical instead of along the normal to the bottom direction. The model has been improved by defining a rotated absolute coordinate system, which best fits the sliding surface, especially in the run-out zone. Alternative choices of the structure of the stress tensor have been tested against experimental data. The two-dimensional model cannot still be applied to real cases. The severe distortion of the mesh, due to strong planimetric gradients of



Figure 1.1: Granular deposit surveyed at the avalanche site of Lavina Granda, in mountainous range of Vigolana, close to Trento (Italy) (February 6th 2004).

velocity, causes the crash of the model in presence of complex topographies.

In order to solve this type of problems, we focused our attention on meshless methods, introduced in chapter §4. In meshless methods, the computational nodes, which discretize the fluid domain, are not bounded by topological relations, as in finite difference and finite element schemes. This makes them suitable for problems characterized by mass separations, strong deformations and discontinuities, like high velocity impacts, high Mach number compressible fluid dynamics, elastic–plastic flows, crack growth problems. The Moving Least Square Particle Hydrodynamics (MLSPH) method, created by Dilts, (7) and (8), has been applied to the one–dimensional model developed at the Department of Civil and Environmental Engineering of Trento. In the MLPSH model the equations of motion are written in weak form and the field variables of the problem are approximated by means of the Moving Least Square Approximants (MLSA) (Lancaster and Salkauskas (16)). The MLSA have been applied to the reconstruction of the snow distribution in the Trentino Province, in order to test their behaviour.

The avalanche site of Lavina Granda, in Vigolana range, has been equipped to measure the dynamic parameters of real avalanches, in order to understand the behaviour of an

avalanche site and to provide parameters for the calibration of the models. In chapter §5 the monitoring activity, observations and collected data are reported.

1.1 The physical and mathematical model

1.1.1 The hypotheses

Assuming that snow balls, which form during the initial phase of motion, are small compared to the avalanche depth, the medium is treated as a continuum. The granular mass is considered incompressible. A dilatation of the mass (not more than 30% in volume, according to laboratory experiments performed with zeolite by Scotton (29)) occurs mainly at the very initial instants, therefore the assumption of incompressibility applies during most of the motion.

To describe the internal rheology, Savage and Hutter (27) proposed a Mohr–Coulomb type yield criterion. To represent the dependence of the tangential stress $p_{\zeta\xi}$ on the normal stress $p_{\zeta\zeta}$, they reported in their article the following relation:

$$\tan \phi = \frac{p_{\zeta\xi}}{p_{\zeta\zeta}} = \frac{p_s(\nu) \tan \phi_s(\nu) + f_2(\nu) \rho_p \sigma^2 \left(\frac{du_\xi}{d\zeta} \right)^2}{p_s(\nu) + f_1(\nu) \rho_p \sigma^2 \left(\frac{du_\xi}{d\zeta} \right)^2},$$

Through experiments performed by means of an annular shear cell, they observed a dependence of the internal friction angle ϕ on the velocity gradient and on the linear granular concentration ν . p_s is the quasi-static contribution to the normal stress $p_{\zeta\zeta}$, σ is the particle diameter, ρ_p is the particle density. They noticed that, incrementing the velocity, a strong dilatation and fluidization takes place. Frictional interactions between particles are substituted by collisional interactions. Nevertheless, as $du_\xi/d\zeta$ grows, the proportionality between tangential and normal stresses is conserved. When $du_\xi/d\zeta$ is very big, the internal frictional angle ϕ asymptotically goes to a dynamic constant value ϕ_d , function of the concentration ν and not of the velocity gradient:

$$\tan \phi_d(\nu) = \frac{f_2(\nu)}{f_1(\nu)}$$

Hungr and Morgenstern (11) performed experiments in open channels in order to investigate the behaviour of granular flows at high velocity. They observed that, as the velocity grows, the momentum transfer mechanism changes, passing from a frictional type to a collisional type. Along the normal to the bottom direction, the linear velocity profile is

substituted by a constant profile (“plug–flow”), with shearing concentrated close to the sliding surface. They stated that the interaction of the granular mass with the bottom can be described through a Coulomb–type relation, with a bottom friction angle δ that is smaller than the internal friction angle ϕ .

All these observations support the hypotheses of our models. A Mohr–Coulomb type internal yield criterion, with internal friction angle ϕ , is applied; a Coulomb–type frictional interaction is assumed along solid boundary surfaces, with a friction angle δ smaller than ϕ ; the velocity is considered constant along the normal to the bottom direction.

Thermodynamic aspects, related to frictional heat production and snow fusion and to granulation processes in the initial phases of natural events, are omitted. Moreover, the model doesn’t simulate mass exchanges with the snow at the bottom and the related variations of momentum, of mass and of the geometry and roughness of the sliding surface.

2 A one-dimensional model with variable width

2.1 Introduction

In this chapter a one-dimensional model for rectangular channels with variable width is developed. The model can be adopted for the study of the dynamic of granular avalanches along narrow valley with variable section. The extension of the original one-dimensional model with constant width implies new rheological hypotheses in order to describe the components of the stress tensor on vertical banks. Continuity and motion equations are simplified in the hypothesis of “shallow water” and averaged in the transversal direction and normally to the bottom.

A three-dimensional curvilinear coordinate system is defined with ζ normal to the bottom, ξ orientated along the channel, and η normal to ξ and ζ (Figure 2.1). The thalweg of the channel is supposed to lie on a vertical plane, i.e. transversal curvature is neglected. The cross section is assumed rectangular with left and right lateral banks defined by:

$$\begin{aligned}\phi_l(\xi, \eta) &= \eta - \frac{b(\xi)}{2} = 0, \\ \phi_r(\xi, \eta) &= \eta + \frac{b(\xi)}{2} = 0,\end{aligned}$$

where b is the width of the channel.

In the curvilinear coordinate system the velocity vector is defined as $\mathbf{u} = (u_\xi, u_\eta, u_\zeta) = u_\xi \mathbf{g}_\xi + u_\eta \mathbf{g}_\eta + u_\zeta \mathbf{g}_\zeta$, where \mathbf{g}_ξ , \mathbf{g}_η e \mathbf{g}_ζ are the versors which define locally the directions of ξ , η e ζ respectively.

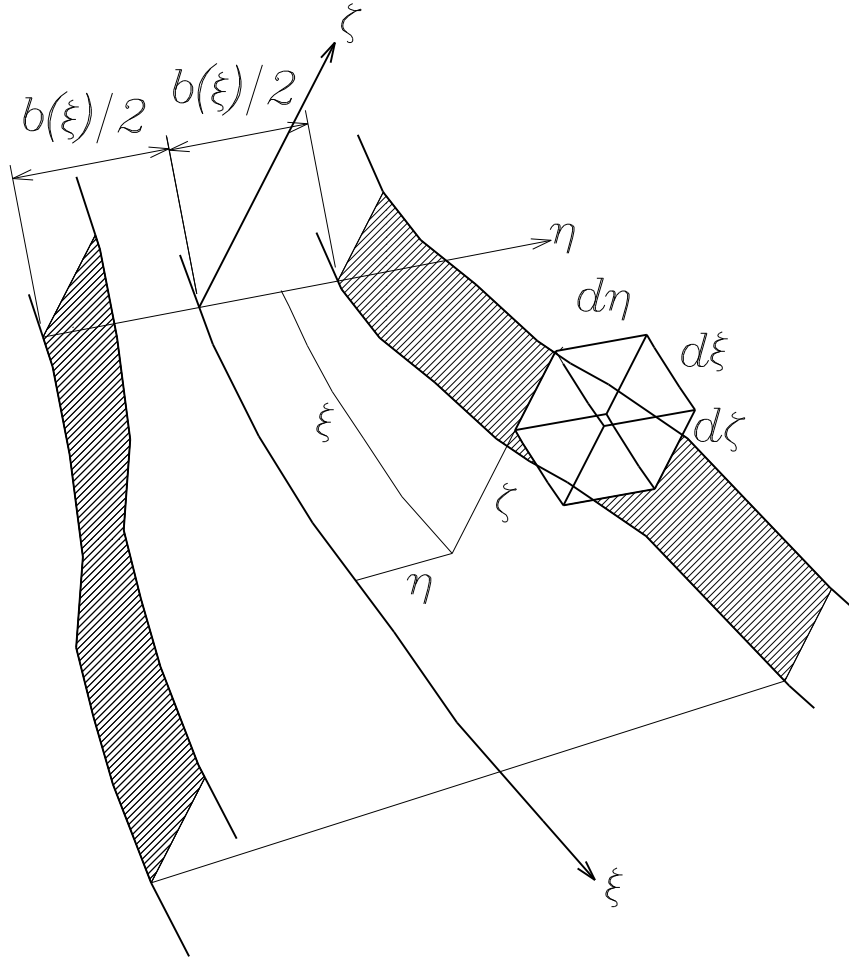


Figure 2.1: The three-dimensional coordinate system.

2.2 The mathematical model

2.2.1 The mass balance equation

We consider an infinitesimal curvilinear volume with edges $d\xi$, $d\eta$ and $d\zeta$ long. The balance of mass fluxes through lateral surfaces gives (see Figure 2.2):

$$\begin{aligned}
 & -u_\xi d\eta d\zeta + \left(u_\xi + \frac{\partial u_\xi}{\partial \xi'} d\xi' \right) d\eta d\zeta - u_\eta \frac{d\xi' + d\xi''}{2} d\zeta + \left(u_\eta + \frac{\partial u_\eta}{\partial \eta} d\eta \right) \frac{d\xi' + d\xi''}{2} d\zeta + \\
 & -u_\zeta d\xi' d\eta + \left(u_\zeta + \frac{\partial u_\zeta}{\partial \zeta} d\zeta \right) d\xi'' d\eta = 0.
 \end{aligned}$$

Being $R = R(\xi)$ the local curvature radius and $\chi = \chi(\xi) = 1/R$ the curvature, one

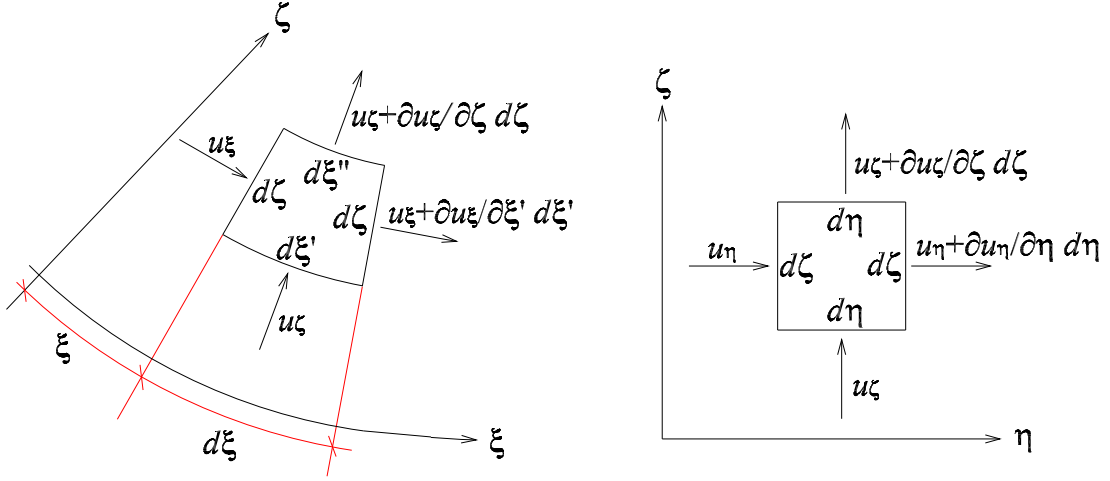


Figure 2.2: Fluxes of mass.

obtains:

$$\begin{aligned} \frac{d\xi}{R} &= \frac{d\xi'}{R-\zeta} = \frac{d\xi''}{R-\zeta-d\zeta} \Rightarrow \\ \Rightarrow d\xi' &= (1-\chi\zeta) d\xi \quad \text{and} \quad d\xi'' = (1-\chi\zeta-\chi d\zeta) d\xi. \end{aligned}$$

Finally, neglecting infinitesimal terms of superior order:

$$\frac{1}{(1-\chi\zeta)} \frac{\partial u_\xi}{\partial \xi} + \frac{\partial u_\eta}{\partial \eta} + \frac{\partial u_\zeta}{\partial \zeta} - \frac{\chi}{(1-\chi\zeta)} u_\zeta = 0. \quad (2.1)$$

2.2.2 Momentum balance equations

The momentum balance equations, in vectorial form, are:

$$\frac{d\mathbf{u}}{dt} = \mathbf{g} + \frac{1}{\rho} \nabla \cdot \mathbf{P}. \quad (2.2)$$

The inertial terms can be developed as follow:

$$\begin{aligned} \frac{d\mathbf{u}}{dt} &= + \frac{\partial u_\xi}{\partial t} \mathbf{g}_\xi + \frac{\partial u_\eta}{\partial t} \mathbf{g}_\eta + \frac{\partial u_\zeta}{\partial t} \mathbf{g}_\zeta + \frac{\partial}{\partial \xi'} (u_\xi \mathbf{g}_\xi + u_\eta \mathbf{g}_\eta + u_\zeta \mathbf{g}_\zeta) \frac{d\xi'}{dt} + \\ &+ \frac{\partial}{\partial \eta} (u_\xi \mathbf{g}_\xi + u_\eta \mathbf{g}_\eta + u_\zeta \mathbf{g}_\zeta) \frac{d\eta}{dt} + \frac{\partial}{\partial \zeta} (u_\xi \mathbf{g}_\xi + u_\eta \mathbf{g}_\eta + u_\zeta \mathbf{g}_\zeta) \frac{d\zeta}{dt} \end{aligned}$$

2. A one-dimensional model with variable width

In the curvilinear system:

$$\frac{\partial \mathbf{g}_\xi}{\partial \xi'} = -\frac{d\beta}{d\xi'} \mathbf{g}_\zeta = \frac{1}{R-\zeta} \mathbf{g}_\zeta, \quad \frac{\partial \mathbf{g}_\eta}{\partial \xi'} = 0, \quad \frac{\partial \mathbf{g}_\zeta}{\partial \xi'} = \frac{d\beta}{d\xi'} \mathbf{g}_\xi = -\frac{1}{R-\zeta} \mathbf{g}_\xi,$$

$$\frac{\partial \mathbf{g}_\xi}{\partial \eta} = \frac{\partial \mathbf{g}_\eta}{\partial \eta} = \frac{\partial \mathbf{g}_\zeta}{\partial \eta} = 0,$$

$$\frac{\partial \mathbf{g}_\xi}{\partial \zeta} = \frac{\partial \mathbf{g}_\eta}{\partial \zeta} = \frac{\partial \mathbf{g}_\zeta}{\partial \zeta} = 0,$$

$$\frac{d\xi'}{dt} = u_\xi, \quad \frac{d\eta}{dt} = u_\eta, \quad \frac{d\zeta}{dt} = u_\zeta.$$

where $\beta = \beta(\xi)$ is the angle upon the horizontal (see Figure 2.3).

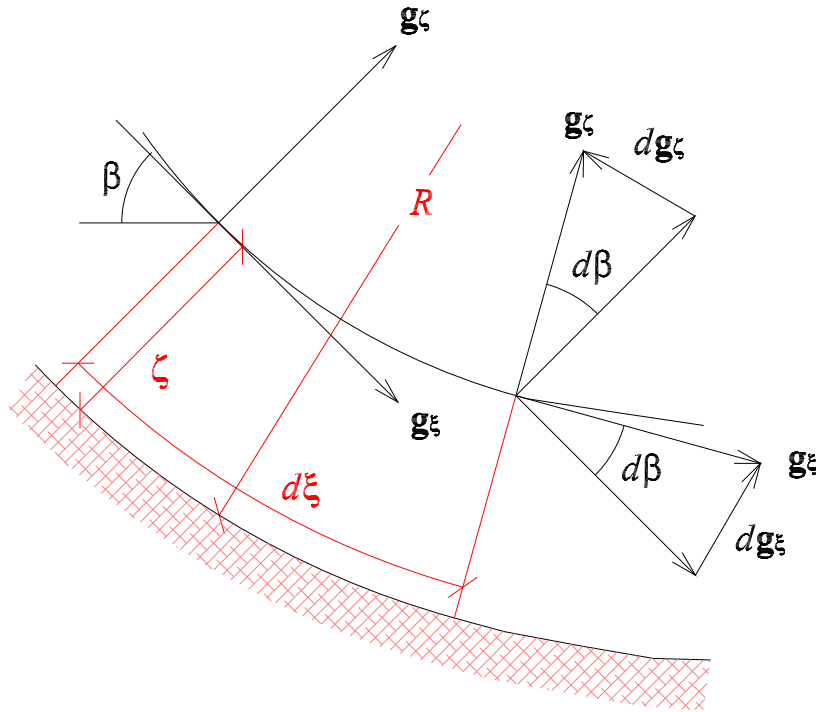


Figure 2.3: The variation of \mathbf{g}_ξ and \mathbf{g}_ζ along ξ .

So we obtain:

$$\begin{aligned}
 \text{along } \mathbf{g}_\xi: & \frac{\partial u_\xi}{\partial t} + \frac{u_\xi}{1-\chi\zeta} \frac{\partial u_\xi}{\partial \xi} + u_\eta \frac{\partial u_\xi}{\partial \eta} + u_\zeta \frac{\partial u_\xi}{\partial \zeta} - \frac{\chi}{1-\chi\zeta} u_\xi u_\zeta; \\
 \text{along } \mathbf{g}_\eta: & \frac{\partial u_\eta}{\partial t} + \frac{u_\xi}{1-\chi\zeta} \frac{\partial u_\eta}{\partial \xi} + u_\eta \frac{\partial u_\eta}{\partial \eta} + u_\zeta \frac{\partial u_\eta}{\partial \zeta}; \\
 \text{along } \mathbf{g}_\zeta: & \frac{\partial u_\zeta}{\partial t} + \frac{u_\xi}{1-\chi\zeta} \frac{\partial u_\zeta}{\partial \xi} + u_\eta \frac{\partial u_\zeta}{\partial \eta} + u_\zeta \frac{\partial u_\zeta}{\partial \zeta} + \frac{\chi}{1-\chi\zeta} u_\xi^2.
 \end{aligned} \tag{2.3}$$

The terms on the right side of equation (2.2) become (calculation details are not reported):

$$\begin{aligned}
 \text{along } \mathbf{g}_\xi: & g \sin \beta + \frac{1}{\rho} \left(\frac{1}{1-\chi\zeta} \frac{\partial p_{\xi\xi}}{\partial \xi} + \frac{\partial p_{\eta\xi}}{\partial \eta} + \frac{\partial p_{\zeta\xi}}{\partial \zeta} - \frac{2\chi}{1-\chi\zeta} p_{\zeta\xi} \right), \\
 \text{along } \mathbf{g}_\eta: & + \frac{1}{\rho} \left(\frac{1}{1-\chi\zeta} \frac{\partial p_{\xi\eta}}{\partial \xi} + \frac{\partial p_{\eta\eta}}{\partial \eta} + \frac{\partial p_{\zeta\eta}}{\partial \zeta} - \frac{\chi}{1-\chi\zeta} p_{\zeta\eta} \right), \\
 \text{along } \mathbf{g}_\zeta: & -g \cos \beta + \frac{1}{\rho} \left(\frac{1}{1-\chi\zeta} \frac{\partial p_{\xi\zeta}}{\partial \xi} + \frac{\partial p_{\eta\zeta}}{\partial \eta} + \frac{\partial p_{\zeta\zeta}}{\partial \zeta} + \frac{\chi}{1-\chi\zeta} (p_{\xi\xi} - p_{\zeta\zeta}) \right).
 \end{aligned} \tag{2.4}$$

2.2.3 Motion equations in non-dimensional form

Non-dimensionalization is executed through scale values of quantities which characterize the phenomenon:

- L_s : the longitudinal length scale;
- B_s : the transversal length scale;
- H_s : the depth scale;
- R_s : the scale for the radius of curvature of bed profile;
- $U_s = U_{\xi s}$: the scale for the velocity along ξ ;
- $U_{\eta s}$: the scale for the velocity along η ;
- $U_{\zeta s}$: the scale for the velocity along ζ ;
- $T_s = L_s/U_{\xi s}$: the time scale;
- P_s : the pressure scale;
- ρ_s : the density scale.

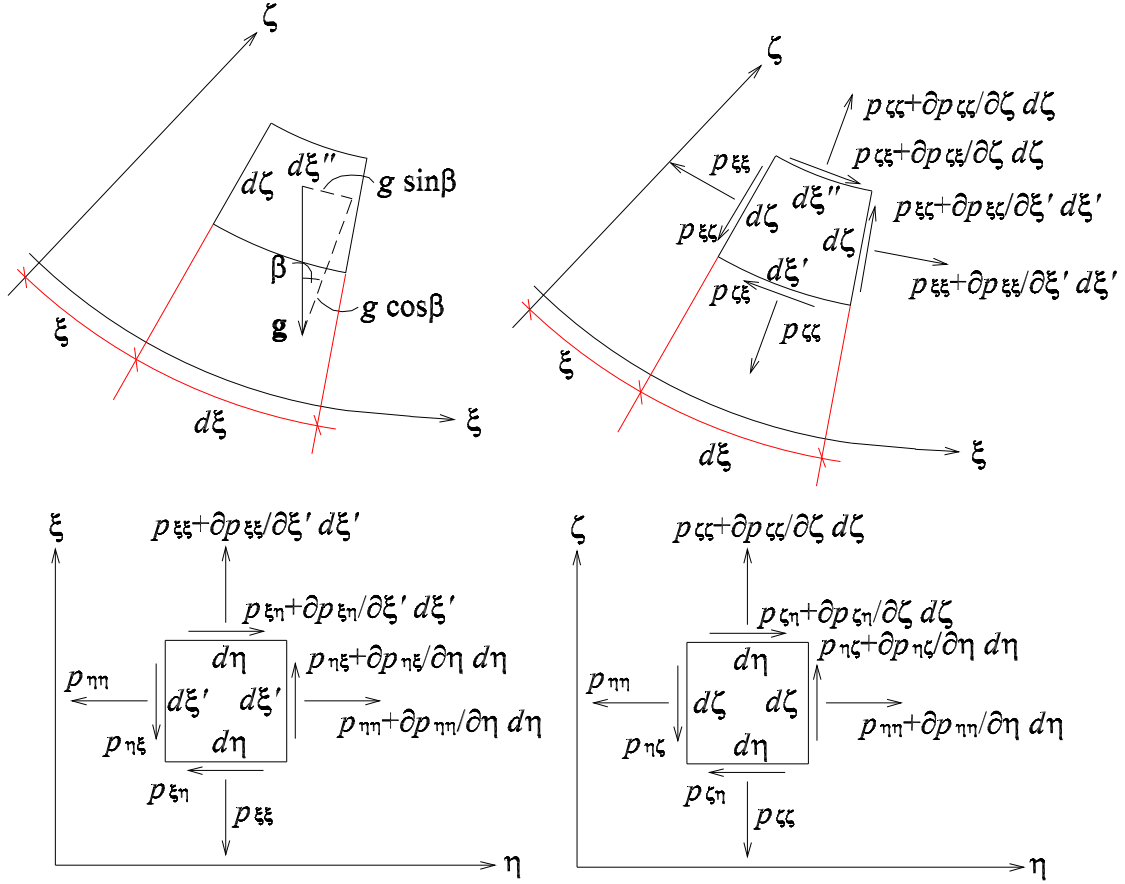


Figure 2.4: Volume and surface forces on the infinitesimal curvilinear volume.

Non-dimensionalized variables are indicated with superscript $\hat{\cdot}$. The ratio between depth and longitudinal scale is defined as $\varepsilon = H_s/L_s$. Assuming $B_s \cong H_s$ it results $B_s/L_s \cong \varepsilon$. The ratio between longitudinal scale and curvature radius scale is $\lambda = L_s/R_s$. The continuity equation becomes:

$$\frac{1}{(1 - \lambda \varepsilon \hat{\chi} \hat{\zeta})} \frac{\partial \hat{u}_\xi}{\partial \hat{\xi}} + \frac{1}{\varepsilon} \frac{U_{\eta s}}{U_{\xi s}} \frac{\partial \hat{u}_\eta}{\partial \hat{\eta}} + \frac{1}{\varepsilon} \frac{U_{\zeta s}}{U_{\xi s}} \frac{\partial \hat{u}_\zeta}{\partial \hat{\zeta}} - \lambda \frac{U_{\zeta s}}{U_{\xi s}} \frac{\hat{\chi}}{(1 - \lambda \varepsilon \hat{\chi} \hat{\zeta})} \hat{u}_\zeta = 0.$$

Fluxes in different directions are of the same order of magnitude if $U_{\eta s}/U_{\xi s} \cong B_s/L_s \cong \varepsilon$ and $U_{\zeta s}/U_{\xi s} \cong \varepsilon$.

In the same way motion equation in ξ direction can be non-dimensionalized. The left member becomes:

$$\frac{U_s^2}{L_s} \left(\frac{\partial \widehat{u}_\xi}{\partial \widehat{t}} + \frac{\widehat{u}_\xi}{1 - \lambda \varepsilon \widehat{\chi} \widehat{\zeta}} \frac{\partial \widehat{u}_\xi}{\partial \widehat{\xi}} + \widehat{u}_\eta \frac{\partial \widehat{u}_\xi}{\partial \widehat{\eta}} + \widehat{u}_\zeta \frac{\partial \widehat{u}_\xi}{\partial \widehat{\zeta}} - \lambda \varepsilon \frac{\chi}{1 - \lambda \varepsilon \widehat{\chi} \widehat{\zeta}} \widehat{u}_\xi \widehat{u}_\zeta \right).$$

The right one gives:

$$g \sin \beta + \frac{P_s}{\rho_s H_s} \frac{1}{\widehat{\rho}} \left(\frac{\varepsilon}{1 - \lambda \varepsilon \widehat{\chi} \widehat{\zeta}} \frac{\partial \widehat{p}_{\xi\xi}}{\partial \widehat{\xi}} + \frac{H_s}{B_s} \frac{\partial \widehat{p}_{\eta\xi}}{\partial \widehat{\eta}} + \frac{\partial \widehat{p}_{\zeta\xi}}{\partial \widehat{\zeta}} - 2 \lambda \varepsilon \frac{\widehat{\chi}}{1 - \lambda \varepsilon \widehat{\chi} \widehat{\zeta}} \widehat{p}_{\xi\zeta} \right).$$

The inertial terms of motion equation in η direction become:

$$\frac{U_s^2}{L_s} \varepsilon \left(\frac{\partial \widehat{u}_\eta}{\partial \widehat{t}} + \frac{\widehat{u}_\xi}{1 - \lambda \varepsilon \widehat{\chi} \widehat{\zeta}} \frac{\partial \widehat{u}_\eta}{\partial \widehat{\xi}} + \widehat{u}_\eta \frac{\partial \widehat{u}_\eta}{\partial \widehat{\eta}} + \widehat{u}_\zeta \frac{\partial \widehat{u}_\eta}{\partial \widehat{\zeta}} \right). \quad (2.5)$$

The external forces terms:

$$= + \frac{P_s}{\rho_s H_s} \frac{1}{\widehat{\rho}} \left(\frac{\varepsilon}{1 - \lambda \varepsilon \widehat{\chi} \widehat{\zeta}} \frac{\partial \widehat{p}_{\xi\eta}}{\partial \widehat{\xi}} + \frac{H_s}{B_s} \frac{\partial \widehat{p}_{c\eta\eta}}{\partial \widehat{\eta}} + \frac{\partial \widehat{p}_{\zeta\eta}}{\partial \widehat{\zeta}} - \lambda \varepsilon \frac{\widehat{\chi}}{1 - \lambda \varepsilon \widehat{\chi} \widehat{\zeta}} \widehat{p}_{\zeta\eta} \right). \quad (2.6)$$

The governing equation along ζ can be treated in a similar way. The left member in non-dimensional form appears as:

$$\frac{U_s^2}{L_s} \varepsilon \left(\frac{\partial \widehat{u}_\zeta}{\partial \widehat{t}} + \frac{\widehat{u}_\xi}{1 - \lambda \varepsilon \widehat{\chi} \widehat{\zeta}} \frac{\partial \widehat{u}_\zeta}{\partial \widehat{\xi}} + \widehat{u}_\eta \frac{\partial \widehat{u}_\zeta}{\partial \widehat{\eta}} + \widehat{u}_\zeta \frac{\partial \widehat{u}_\zeta}{\partial \widehat{\zeta}} + \frac{\lambda}{\varepsilon} \frac{\widehat{\chi} \widehat{u}_\xi^2}{1 - \lambda \varepsilon \widehat{\chi} \widehat{\zeta}} \right).$$

The right member:

$$= -g \cos \beta + \frac{P_s}{\rho_s H_s} \frac{1}{\widehat{\rho}} \left(\frac{\varepsilon}{1 - \lambda \varepsilon \widehat{\chi} \widehat{\zeta}} \frac{\partial \widehat{p}_{\xi\zeta}}{\partial \widehat{\xi}} + \frac{H_s}{B_s} \frac{\partial \widehat{p}_{\eta\zeta}}{\partial \widehat{\eta}} + \frac{\partial \widehat{p}_{\zeta\zeta}}{\partial \widehat{\zeta}} + \lambda \varepsilon \frac{\widehat{\chi}}{1 - \lambda \varepsilon \widehat{\chi} \widehat{\zeta}} (\widehat{p}_{\zeta\zeta} - \widehat{p}_{\xi\xi}) \right).$$

λ is assumed of order 1 (i.e. the radius of curvature, R_s , is comparable to L_s) and $\varepsilon \ll 1$ ("shallow water" hypothesis). It is assumed that inertial, gravitational and pressure forces are comparable. It descends that $U_s^2/L_s \cong g \cong P_s/\rho_s H_s$ and so the Froude number scale is $Fr_s = U_s/\sqrt{gH_s} \cong 1/\sqrt{\varepsilon}$ and the pressure scale $P_s \cong \rho_s U_s^2$. It follows that, in the motion equation along η , all inertial terms are negligible in (2.5), and, discarding all terms depending on ε in the second member (2.6), the result is:

$$\frac{\partial p_{\eta\eta}}{\partial \eta} + \frac{\partial p_{\zeta\eta}}{\partial \zeta} = 0. \quad (2.7)$$

Similarly in motion equation along ζ , neglecting terms of order ε , one gets:

$$\frac{\partial p_{\zeta\zeta}}{\partial \zeta} + \frac{\partial p_{\eta\zeta}}{\partial \eta} = +\rho (g \cos \beta + \chi u_\xi^2) . \quad (2.8)$$

The continuity equation and the motion equation along ξ will be simplified later, in the averaged form.

2.2.4 The definition of the stress tensor

To define the stress tensor we rely on the rheology proposed by Hutter and Savage (28), modified to keep into consideration the effects on vertical banksides. A Mohr–Coulomb type yield criterion, with internal friction angle ϕ , is applied to the granular material. The bottom and the lateral sides are treated as sliding surfaces with a Coulomb type frictional law. δ_b , δ_l , δ_r are the friction angles at the bottom, left side and right side respectively. Relying on these boundary conditions the stress tensor can be exactly defined at basal corners of the rectangular section. At each side a local coordinate system, with Ξ orientated along the bank and H normal to it, can be defined (see Figure 2.5).

The stress tensor at the left and right corner in the corresponding local coordinate system $\Xi H \zeta$, can be defined as:

$$\left(\tilde{\mathbf{P}} \right)_{l/r} = \begin{pmatrix} p_{\Xi\Xi} & (p_{\Xi H})_{l/r} & p_{\Xi\zeta} \\ (p_{H\Xi})_{l/r} & (p_{HH})_{l/r} & p_{H\zeta} \\ p_{\zeta\Xi} & p_{\zeta H} & p_{\zeta\zeta} \end{pmatrix} .$$

Assuming secondary circulations and stresses of little magnitude, we can consider $p_{\zeta H} \cong p_{H\zeta} \cong 0$.

Frictional boundary conditions at the bottom and at the left and right sides give:

$$\begin{aligned} p_{\zeta\Xi} &= +\text{sgn}(u_\xi) \tan \delta_b p_{\zeta\zeta} , \\ (p_{H\Xi})_l &= +\text{sgn}(u_\xi) \tan \delta_l (p_{HH})_l , \\ (p_{H\Xi})_r &= -\text{sgn}(u_\xi) \tan \delta_r (p_{HH})_r . \end{aligned}$$

The Mohr–Coulomb type yield criterion, applied to the coordinate planes ΞH and $\Xi \zeta$, allows to evaluate $p_{\Xi\Xi}$'s dependence on $p_{\zeta\zeta}$ and p_{HH} .

On the Mohr diagram, the circle which defines the stress state on the plane $\Xi \zeta$ must pass through the point $(-p_{\zeta\zeta}, |p_{\zeta\Xi}|)$ and has to be tangential to the yield envelope with slope ϕ (Figure 2.6). Two circles respect the imposed conditions. The one which corresponds to

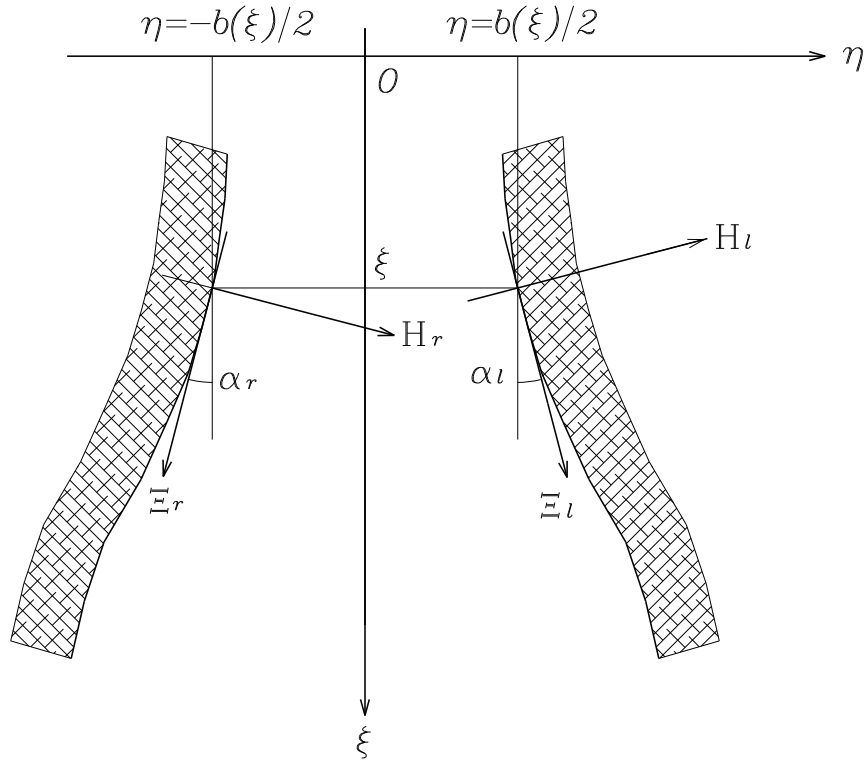


Figure 2.5: (Ξ, H) -local coordinate systems relevant to the orientation of the banks.

a greater value of $-p_{\Xi\Xi}$ is associated to the passive state, which, in the theory of Savage and Hutter, takes place when $\partial u_{\xi}/\partial \xi < 0$. The other circle represents the stress state when $\partial u_{\xi}/\partial \xi > 0$ (active state). It means that:

$$p_{\Xi\Xi} = k_{a/p}^{\zeta} p_{\zeta\zeta}, \quad (2.9)$$

where $k_{a/p}^{\zeta}$ is equal to k_a or k_p defined as:

$$\left. \begin{array}{l} k_p \\ k_a \end{array} \right\} = \frac{2}{\cos^2 \phi} \left[1 \pm \sqrt{1 - \frac{\cos^2 \phi}{\cos^2 \delta}} \right] - 1, \quad \text{if } \begin{array}{l} \frac{\partial u_{\xi}}{\partial \xi} < 0 \\ \frac{\partial u_{\xi}}{\partial \xi} > 0 \end{array}. \quad (2.10)$$

Similar hypotheses can be used to define stress tensor components on the plane ΞH . Two circles, tangential to material yield locus defined by the internal frictional angle ϕ , can be drawn through the point $(-p_{HH}, |p_{H\Xi}|)$ (see Figure 2.7). The criterion of selection between the two corresponding states is not as clear as on plane $\Xi\zeta$ and has to be experimentally tested. One idea could be to assume as discrimination element the sign

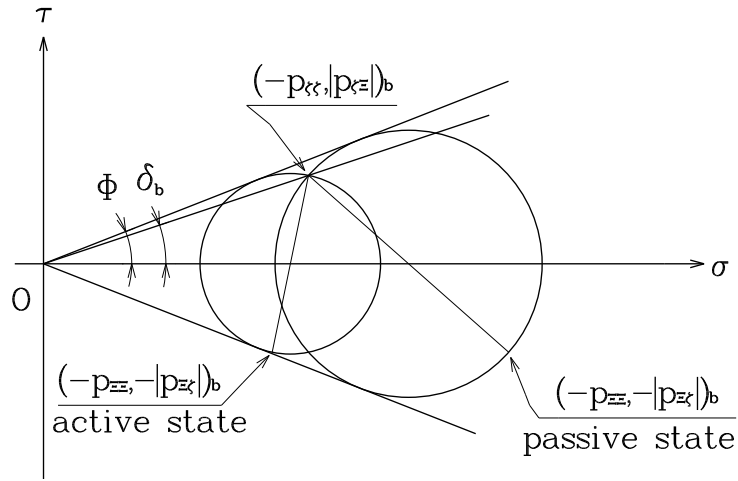


Figure 2.6: The definition of the stress tensor components on the plane $\Xi\zeta$ according to the Savage–Hutter rheology (28).

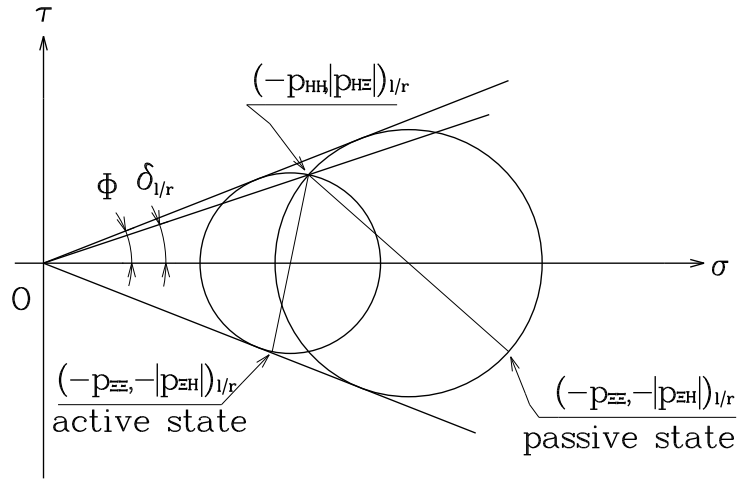


Figure 2.7: The definition of the stress tensor components on the plane ΞH according to the Savage–Hutter rheology (28).

of $\partial u_\xi / \partial \xi$, just as on $\Xi\zeta$ plane. The result is that:

$$p_{\Xi\Xi} = k_{a/p}^H p_{HH},$$

where $k_{a/p}^H$ is identical to $k_{a/p}^\zeta$. According to this approach:

$$p_{HH} = p_{\zeta\zeta} \quad \text{and so} \quad k_{HH} = 1.$$

Another possible choice is to take $k_{a/p}^H$ equal to k_a or k_p as defined by equation (2.10), according to the sign of $\partial b/\partial \xi$.

$$\left(k_{a/p}^H\right)_{l/r} = \begin{cases} k_a \\ k_p \end{cases} \quad \text{if } \frac{\partial b}{\partial \xi} \begin{matrix} > 0 \\ < 0 \end{matrix}.$$

For example, if lateral banks converge ($\partial b/\partial \xi < 0$), passive state takes place and $p_{\Xi\Xi} = (k_p)_{l/r} (p_{HH})_{l/r}$. In this way one obtains that:

$$(p_{HH})_{l/r} = \frac{p_{\Xi\Xi}}{\left(k_{a/p}^H\right)_{l/r}} = \frac{k_{a/p}^\zeta}{\left(k_{a/p}^H\right)_{l/r}} p_{\zeta\zeta} = (k_{HH})_{l/r} p_{\zeta\zeta}.$$

On the left and right banks the pressure p_{HH} can be different because of unequal friction angles δ_l and δ_r .

Finally, we can write the stress tensor at each corner at the bottom of the section as:

$$\left(\tilde{\mathbf{P}}\right)_{l/r} = \begin{pmatrix} k_{\Xi\Xi} & (k_{\Xi H})_{l/r} & k_{\Xi\zeta} \\ (k_{H\Xi})_{l/r} & (k_{HH})_{l/r} & k_{H\zeta} \\ k_{\zeta\Xi} & k_{\zeta H} & k_{\zeta\zeta} \end{pmatrix} p_{\zeta\zeta} = \left(\tilde{\mathbf{K}}\right)_{l/r} p_{\zeta\zeta}.$$

where

$$\begin{aligned} k_{\Xi\Xi} &= k_{a/p}^\zeta, \\ (k_{\Xi H})_{l/r} &= (k_{H\Xi})_{l/r} = \pm \text{sgn}(u_\xi) \tan \delta_{l/r} k_{a/p}^\zeta / k_{a/p}^H, \\ k_{\Xi\zeta} &= k_{\zeta\Xi} = -\text{sgn}(u_\xi) \tan \delta_b, \\ (k_{HH})_{l/r} &= k_{a/p}^\zeta / \left(k_{a/p}^H\right)_{l/r}, \\ k_{H\zeta} &= k_{\zeta H} = 0, \\ k_{\zeta\zeta} &= 1. \end{aligned}$$

Every component of $\left(\tilde{\mathbf{P}}\right)_{l/r}$ depends linearly on $p_{\zeta\zeta}$.

The components of $\left(\mathbf{P}\right)_{l/r}$ in (ξ, η, ζ) -coordinate system are obtained rotating the stress tensor by the angle $(\alpha)_{l/r}$ between $(\Xi)_{l/r}$ and ξ (see Figure 2.5):

$$\left(\mathbf{P}\right)_{l/r} = \left(\mathbf{R} \tilde{\mathbf{P}} \mathbf{R}^T\right)_{l/r} = \left(\mathbf{R} \tilde{\mathbf{K}} \mathbf{R}^T\right)_{l/r} p_{\zeta\zeta} = \left(\mathbf{K}\right)_{l/r} p_{\zeta\zeta}.$$

where $(\mathbf{R})_{l/r}$ is the rotation matrix:

$$(\mathbf{R})_{l/r} = \begin{pmatrix} \cos(\alpha)_{l/r} & -\sin(\alpha)_{l/r} & 0 \\ \sin(\alpha)_{l/r} & \cos(\alpha)_{l/r} & 0 \\ 0 & 0 & 1 \end{pmatrix}.$$

$(\alpha)_{l/r}$ can be calculated as:

$$(\alpha)_{l/r} = \pm \arcsin \frac{db/d\xi}{2\sqrt{1 + (d(b)_{l/r}/d\xi)^2}}. \quad (2.11)$$

The components of $(\mathbf{K})_{l/r}$, the tensor of stress coefficients, in the (ξ, η, ζ) -coordinate system, result:

$$(k_{\xi\xi})_{l/r} = \cos^2(\alpha)_{l/r} (k_{\Xi\Xi})_{l/r} - 2 \sin(\alpha)_{l/r} \cos(\alpha)_{l/r} (k_{H\Xi})_{l/r} + \sin^2(\alpha)_{l/r} (k_{HH})_{l/r},$$

$$(k_{\xi\eta})_{l/r} = (k_{\eta\xi})_{l/r} = \sin(\alpha)_{l/r} \cos(\alpha)_{l/r} \left((k_{\Xi\Xi})_{l/r} - (k_{HH})_{l/r} \right) + \left(\cos^2(\alpha)_{l/r} - \sin^2(\alpha)_{l/r} \right) (k_{H\Xi})_{l/r},$$

$$(k_{\xi\zeta})_{l/r} = (k_{\zeta\xi})_{l/r} = \cos(\alpha)_{l/r} (k_{\zeta\xi})_{l/r},$$

$$(k_{\eta\eta})_{l/r} = \sin^2(\alpha)_{l/r} (k_{\Xi\Xi})_{l/r} - 2 \sin(\alpha)_{l/r} \cos(\alpha)_{l/r} (k_{H\Xi})_{l/r} + \cos^2(\alpha)_{l/r} (k_{HH})_{l/r},$$

$$(k_{\eta\zeta})_{l/r} = (k_{\zeta\eta})_{l/r} = \sin(\alpha)_{l/r} (k_{\zeta\xi})_{l/r}.$$

Deriving equation (2.8) over ζ and equation (2.7) over η and then subtracting the two equations, one obtains:

$$\frac{\partial^2 p_{\eta\eta}}{\partial \eta^2} + \frac{\partial^2 p_{\zeta\zeta}}{\partial \zeta^2} = 0, \quad (2.12)$$

and so if $p_{\zeta\zeta}$ were linearly distributed along ζ , $p_{\eta\eta}$ should be linearly distributed over η .

It can be noticed from (2.11) that $\sin(\alpha)_{l/r} = O(\varepsilon)$ and so $(k_{\zeta\eta})_{l/r}$ is negligible compared with the other coefficients. Integrating the governing equation along ζ (equation (2.8))

over η , in the range between $-b/2$ and $b/2$, and then over ζ , in the range between ζ and h , the hydrostatic distribution of pressure is obtained:

$$\begin{aligned} \frac{\partial \bar{p}_{\zeta\zeta}}{\partial \zeta} &= \rho (g \cos \beta + \chi \bar{u}_{\xi}^2) \Rightarrow \\ \Rightarrow \bar{p}_{\zeta\zeta} &= -\rho (g \cos \beta + \chi \bar{u}_{\xi}^2) (h(\xi, t) - \zeta), \end{aligned}$$

where

$$\phi_h(\xi, \zeta, t) = \zeta - h(\xi, t) = 0 \quad (2.13)$$

represents the equation of free surface, and

$$\bar{p}_{\zeta\zeta} = \frac{1}{b} \int_{b_r}^{b_l} p_{\zeta\zeta} d\eta$$

is the value of $p_{\zeta\zeta}$ averaged over η . According to the “plug-flow” hypothesis, u_{ξ} is supposed constant over ζ and η , and h constant over η . On this basis it seems reasonable to suppose $p_{\zeta\zeta}$ linear along ζ . As a consequence, equation (2.12) tells that $p_{\eta\eta}$ has to be linear along η . Being the stress tensor proportional to $p_{\zeta\zeta}$ at the inferior corners of the section, a linear dependence of all the components of the stress tensor from ζ and η can be hypothesized. It is possible to separate the dependence from ξ and ζ in different factors, such as:

$$\begin{aligned} \mathbf{P}(\xi, \eta, \zeta, t) &= -\mathbf{K}(\xi, \eta, t) p_{\zeta\zeta}(\xi, \zeta, t) = \\ &= -\frac{\mathbf{K}_l(\xi, t) (\eta - b_r(\xi)) + \mathbf{K}_r(\xi, t) (b_l(\xi, t) - \eta)}{b_l(\xi, t) - b_r(\xi)} \cdot \\ &\quad \cdot \rho (g \cos \beta(\xi) + \chi(\xi) u_{\xi}^2(\xi, t)) (h(\xi, t) - \zeta). \end{aligned} \quad (2.14)$$

2.2.5 Motion equations averaged over η

Now it is possible to integrate over η the mass and momentum balance equations. The averaged components of the velocity vector are:

$$\begin{aligned}\bar{u}_\xi &= \frac{1}{b} \int_{-b/2}^{b/2} u_\xi d\eta, \\ \bar{u}_\eta &= \frac{1}{b} \int_{-b/2}^{b/2} u_\eta d\eta, \\ \bar{u}_\zeta &= \frac{1}{b} \int_{-b/2}^{b/2} u_\zeta d\eta,\end{aligned}$$

The kinematic boundary conditions at the sides are:

$$\begin{aligned}(\mathbf{u})_{l/r} \cdot \nabla (\phi)_{l/r} &= 0 \Rightarrow \\ \Rightarrow \pm \frac{1}{2} \frac{(u_\xi)_{l/r}}{1 - \chi \zeta} \frac{db}{d\xi} + (u_\eta)_{l/r} &= 0.\end{aligned}$$

Multiplying by $(1 - \chi \zeta)$ the continuity equation (2.1) and integrating over η , one obtains:

$$\frac{\partial}{\partial \xi} (b \bar{u}_\xi) + b \frac{\partial}{\partial \zeta} (\bar{u}_\zeta (1 - \chi \zeta)) = 0. \quad (2.15)$$

In order to integrate the inertial terms of the motion equation in the direction ξ (2.3), it is useful to write them in conservative form, summing the continuity equation (2.1) multiplied by u_ξ :

$$\frac{\partial u_\xi}{\partial t} + \frac{1}{1 - \chi \zeta} \frac{\partial}{\partial \xi} (u_\xi^2) + \frac{\partial}{\partial \eta} (u_\xi u_\eta) + \frac{\partial}{\partial \zeta} (u_\xi u_\zeta) - 2 \frac{\chi}{1 - \chi \zeta} u_\xi u_\zeta.$$

Then, they can be integrated over η , simplified invoking kinematic boundary conditions, and, at last, re-written in non-conservative form, subtracting the averaged continuity equation (2.15) multiplied by $\bar{u}_\xi / (1 - \chi \zeta)$:

$$b \left(\frac{\partial \bar{u}_\xi}{\partial t} + \frac{\bar{u}_\xi}{1 - \chi \zeta} \frac{\partial \bar{u}_\xi}{\partial \xi} + \bar{u}_\zeta \frac{\partial \bar{u}_\xi}{\partial \zeta} - \frac{\chi \bar{u}_\xi \bar{u}_\zeta}{1 - \chi \zeta} \right).$$

The integration of the terms of forces requires more work. The generic component of the stress tensor can be written as (see (2.14)):

$$p_{ij} = -\rho A \frac{(k_{ij})_l (\eta + b/2) + (k_{ij})_r (b/2 - \eta)}{b} (h(\xi, t) - \zeta),$$

where:

$$A = A(\xi, t) = g \cos \beta + \chi \bar{u}_\xi^2,$$

being u_ξ nearly constant over the section (“plug-flow” condition).

The averaged value of p_{ij} over η results:

$$\bar{p}_{ij} = \frac{1}{b} \int_{-b/2}^{b/2} p_{ij} d\eta = \dots = -\rho A \frac{(k_{ij})_l + (k_{ij})_r}{2} (h - \zeta).$$

The member of forces (2.4) integrated over η gives:

$$\begin{aligned} g b \sin \beta - & \left[\frac{1}{1 - \chi \zeta} \frac{\partial}{\partial \xi} \left(b A \frac{(k_{\xi\xi})_l + (k_{\xi\xi})_r}{2} (h - \zeta) \right) + \right. \\ & - \frac{A (h - \zeta)}{2} \frac{1}{1 - \chi \zeta} \frac{\partial b}{\partial \xi} ((k_{\xi\xi})_r + (k_{\xi\xi})_l) + \\ & + A (h - \zeta) ((k_{\eta\xi})_l - (k_{\eta\xi})_r) + \\ & \left. - b A \frac{(k_{\xi\zeta})_l + (k_{\xi\zeta})_r}{2} \left(1 + \frac{2\chi b}{1 - \chi \zeta} \right) \right]. \end{aligned}$$

2.2.6 Motion equations averaged over the section

We define the components of velocity averaged over the entire section:

$$U_\xi = \frac{1}{h} \int_0^h \bar{u}_\xi d\zeta,$$

$$U_\eta = \frac{1}{h} \int_0^h \bar{u}_\eta d\zeta,$$

$$U_z = \frac{1}{h} \int_0^h \bar{u}_\zeta d\zeta,$$

In order to average over ζ , it is necessary to invoke the kinematic boundary conditions:

- at the bottom:

$$(u_\zeta)_b = 0.$$

- at free surface, from (2.13):

$$\begin{aligned} & \frac{\partial \phi_h}{\partial t} + \nabla \phi_h \cdot \bar{\mathbf{u}} = 0 \Rightarrow \\ \Rightarrow & -\frac{\partial h}{\partial t} - \frac{\bar{u}_\xi}{1 - \chi h} \frac{\partial h}{\partial \xi} + \bar{u}_\zeta = 0. \end{aligned}$$

The continuity equation becomes:

$$b \frac{\partial h}{\partial t} + \frac{1}{1 - \chi h} \frac{\partial}{\partial \xi} (b h U_\xi).$$

The inertial terms of the motion equation along ξ :

$$b h \left(\left(1 - \chi \frac{h}{2}\right) \frac{\partial U_\xi}{\partial t} + U_\xi \frac{\partial U_\xi}{\partial \xi} - \chi U_\xi U_z \right).$$

The averaged value of the generic component of the stress tensor is:

$$P_{ij} = \frac{1}{h} \int_0^h p_{ij} d\zeta = -\rho A \frac{(K_{ij})_l + (K_{ij})_r}{2} \frac{h^2}{2},$$

where, assuming \bar{u}_ξ , $(k_{ij})_l$ and $(k_{ij})_r$ nearly uniform along ζ :

$$A = A(\xi, t) = g \cos \beta + \chi U_\xi^2,$$

$$(K_{ij})_l = \frac{1}{h} \int_0^h (\bar{k}_{ij})_l d\zeta \cong (k_{ij})_l \quad \text{and}$$

$$(K_{ij})_r = \frac{1}{h} \int_0^h (\bar{k}_{ij})_r d\zeta \cong (k_{ij})_r.$$

The member of forces is given by:

$$\begin{aligned} & g \sin \beta b h \left(1 - \frac{\chi h}{2}\right) - \left[\frac{\partial}{\partial \xi} \left(\frac{A b h^2}{4} ((K_{\xi\xi})_l + (K_{\xi\xi})_r) \right) + \right. \\ & \quad - \frac{A h^2}{4} \frac{\partial b}{\partial \xi} ((K_{\xi\xi})_r + (K_{\xi\xi})_l) + \\ & \quad + \frac{A h^2}{2} \left(1 - \frac{\chi h}{3}\right) ((K_{\eta\xi})_l - (K_{\eta\xi})_r) + \\ & \quad \left. - \frac{A h b}{2} \left(1 + \frac{\chi h}{2}\right) ((K_{\zeta\xi})_l + (K_{\zeta\xi})_r) \right]. \end{aligned}$$

Neglecting all the terms depending on $\lambda \varepsilon$, the final versions of the continuity equation and of the motion equation along ξ , divided by $b h$ are:

$$\frac{\partial (b h)}{\partial t} + \frac{\partial (b h U_\xi)}{\partial \xi} = 0, \quad (2.16)$$

$$\begin{aligned} \frac{\partial U_\xi}{\partial t} + U_\xi \frac{\partial U_\xi}{\partial \xi} - \chi U_\xi U_z = \\ = g \sin \beta + \frac{1}{b h} \left[\frac{\partial (b h P_{\xi\xi})}{\partial \xi} + \frac{\partial b}{\partial \xi} ((P_{\xi\xi})_r - (P_{\xi\xi})_l) + \right. \\ \left. + h ((P_{\eta\xi})_l - (P_{\eta\xi})_r) - 2 b P_{\zeta\xi} \right]. \end{aligned} \quad (2.17)$$

2.3 The numerical model

Motion equations are solved by means of a lagrangian finite difference scheme. The granular mass is discretized in a number N of cells, delimited through $N + 1$ surfaces normal to the bottom (see Figure 2.8). The computational grid moves with the mass. The averaged velocity of each grid node i ,

$$U_{\xi i} = U_{\xi i}(x(t), t) = U_{\xi i}(t) ,$$

is calculated at instant t^{n+1} , solving the averaged momentum balance equation along ξ (equation (2.17)) through a Collatz scheme (see (32)). The Equation of motion along ξ is an ordinary differential equation of first order, and can be written as:

$$\frac{dU_{\xi}}{dt} = f(U_{\xi}, t) .$$

According to the Collatz scheme, such type of equations are integrated in two steps:

$$U_{\xi i}^{n+1} = U_{\xi i}^n + \Delta t f\left(\hat{U}_{\xi i}^{n+1/2}, t^{n+1/2}\right) , \quad \text{where}$$

$$\hat{U}_{\xi i}^{n+1/2} = U_{\xi i}^n + \frac{\Delta t}{2} f\left(\hat{U}_{\xi i}^n, t^n\right) \quad \text{and}$$

$$\Delta t = t^{n+1} - t^n .$$

Afterwards the position of the generic node i can be updated:

$$\xi_i^{n+1} = \xi_i^n + \frac{U_{\xi i}^{n+1} + U_{\xi i}^n}{2} \Delta t .$$

The conservation of mass is ensured imposing the constancy of volume for each cell. It follows that the depth of the generic cell $i + 1/2$ at instant $n + 1$ comes from:

$$h_{i+1/2}^{n+1} = \frac{\mathbb{V}_{i+1/2}}{b_{i+1/2}^{n+1} (\xi_{i+1}^{n+1} - \xi_i^{n+1})} ,$$

being $\mathbb{V}_{i+1/2}$ the constant volume for cell $i+1/2$ and $b_{i+1/2}^{n+1}$ the channel width at $(\xi_i^{n+1} + \xi_{i+1}^{n+1})/2$.

Some conditions are imposed on the integration time step Δt to guarantee the stability of the model. In order to prevent the overlapping of neighbour cells, the generic node must not go over the subsequent nodes during a single time step. Furthermore, the informations relevant to changes of the motion field in a node must not cover distances greater than the extension of adjacent cells. The velocity of such informations is the celerity of propagation of little gravitational waves and so this appears as a Courant–Friedrichs–Levy type stability

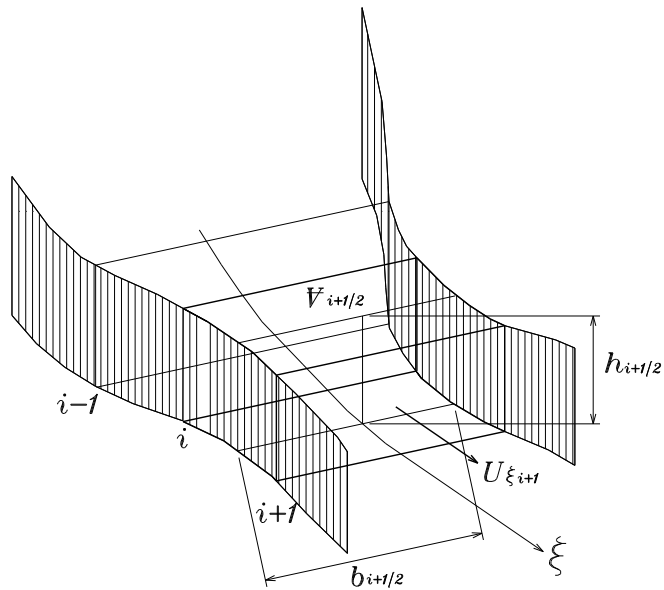


Figure 2.8: The curvilinear computational grid used to discretize the granular mass.

condition. To smooth the instabilities arising during the run-out phase, Δt is reduced up to prevent the inversion of motion during a single time step.

In spite of all these conditions on the time step Δt , further instabilities can arise develop in presence of shocks induced by abrupt slowing down due to slope reductions or to narrowings of the channel. They are reduced through an adding diffusive term.

A detailed description of the numerical scheme, used for the one-dimensional model with constant width $1d$ and applied, with little changes, to the variable-width model $1dwvar$, can be found in (6).

The numerical model is implemented in a C++ code. To treat half integer numbers (i.e. numbers which can be represented as the sum of an integer and constant $1/2$), we resorted to the HINT class, developed by dr. Enrico Bertolazzi and available on the web site <http://www.ing.unitn.it/~bertolaz>.

2.4 Comparison of numerical results with experiments

The rheological hypotheses, applied to describe the frictional interactions with the vertical side banks of the channel, have been tested against data of different laboratory experiments, executed in constant width chutes:

- a slump test on horizontal plane, reported in (4);
- one experiment in a double slope chute, described in (12);
- three experiments with different granular materials in a convex and concave curved chute (see (10)).

Simulations of the variable width model *1dwvar*, developed by the author, are compared with simulations obtained by the original one-dimensional model with constant width $1d$, implemented at the Department of Civil and Environmental Engineering. In the $1d$ model, to take account of the lateral friction, two different corrective factors for the bottom friction angle δ have been tried. One approach was proposed by Savage and Hutter (28):

$$\tan \delta_{eff} = \left(1 + k \frac{H_s}{B_s} h \right) \tan \delta = (1 + \varepsilon k_{wall} h) \tan \delta, \quad \text{where} \quad (2.18)$$

$$k_{wall} = \frac{L_s}{B_s} k.$$

The other one, due to Greve and Hutter (10), proposes:

$$\delta_{eff} = \delta + \varepsilon k_w \frac{h}{H_s}. \quad (2.19)$$

2.4.1 Slump on horizontal plane

The experiments were carried out at the Hydraulic Laboratory of the University of Trento in a $0.3m$ wide chute, with the lateral vertical walls and the bottom in perspex, a transparent plastic material. The mass of granular material is initially confined by a rotating gate, that can be instantaneously opened by the recalling force of a spring. The gate is initially inclined of 55° on the horizontal plane. D'Accordi made experiments with two granular materials: gravel and zeolite. We present the results obtained with zeolite, an anionic synthetic resin, having dimensions which range from $0.1mm$ to $2mm$ and a mean diameter of $1mm$. Internal and bottom static friction angles were estimated through a

shear box:

$$\phi = 28^\circ \pm 0.75^\circ ;$$

$$\delta = 18^\circ \pm 0.75^\circ .$$

Depth are non-dimensionalized through $H_s = 0.17 m$, the initial depth of the mass. The longitudinal scale L_s is taken equal to $0.119 m$, the horizontal projection of the frontal inclined part of the initial deposit. The transversal length scale is $B_s = 0.3 m$, the width of the chute.

Simulation	$\phi[^\circ]$	$\delta[^\circ]$	$k[-]$
d.1d.1	26	18	0
d.1d.2	26	18	0.4

Table 2.1: Values of the rheological parameters used in the numerical simulations of the experiments of D'Accordi (4) with the one-dimensional model with constant width (*1d*). ϕ is the internal friction angle, δ the bottom friction angle, k the coefficient of the corrective factor of δ proposed by Savage and Hutter (28) (see equation (2.18)).

Simulation	$\phi[^\circ]$	$\delta_b[^\circ]$	$\delta_l[^\circ]$	$\delta_r[^\circ]$
d.1dwvar.1	26	18	0	0
d.1dwvar.2	26	18	18	18

Table 2.2: Values of the rheological parameters used in the numerical simulations of the experiments of D'Accordi (4) with the one-dimensional model with variable width (*1dwvar*). ϕ is the internal friction angle, δ_b the bottom friction angle, δ_l and δ_r are the lateral friction angles at the left and right sides respectively.

Numerical simulations of *1d* and *1dwvar*, obtained neglecting the lateral friction, are compared in Figure 2.9. The results are identical, but fitting of experimental data is worse than in the simulations shown in Figure 2.10, where a coefficient $k = 0.4$ is used in the corrective factor equation (2.18) of δ in the *1d* model, while a lateral friction angle equal to 18° is applied at the lateral sides of the chute in the *1dwvar* model. The *1dwvar* model gives a better prediction than the *1d* model.

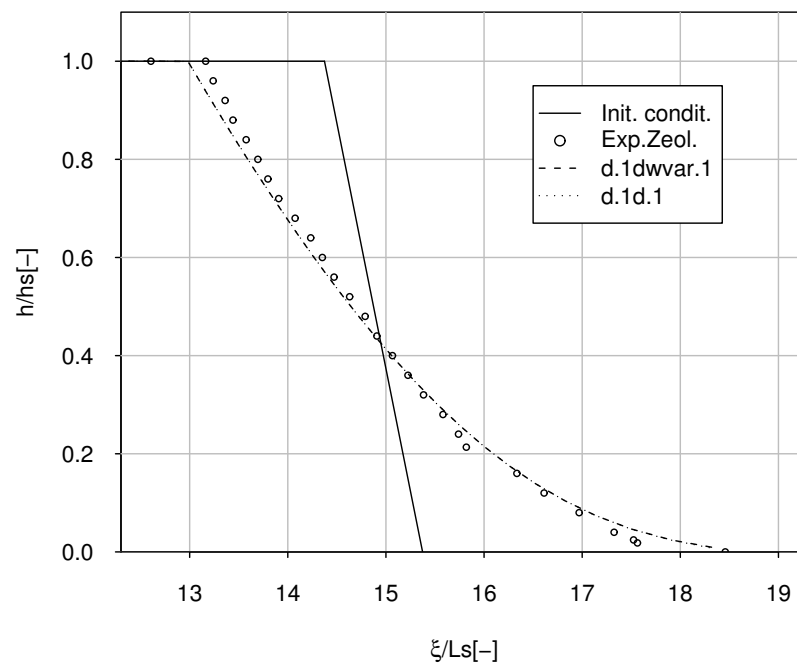


Figure 2.9: Slump on horizontal plane. Comparison of experimental data and numerical simulations produced by the one-dimensional models with constant width ($1d$) and variable width ($1dwvar$), assuming no frictional interaction at lateral walls. The values of rheological parameters used in different simulations are shown in Table 2.1 and Table 2.2.

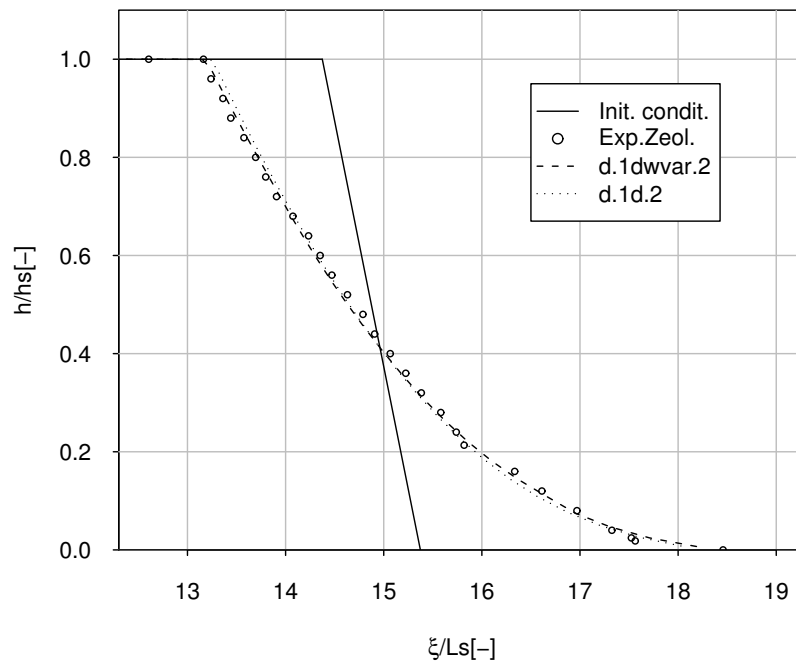


Figure 2.10: Slump on horizontal plane. Comparison of experimental data and numerical simulations produced by the one-dimensional models with constant width ($1d$) and variable width ($1dvar$), adding lateral friction at banks. The values of rheological parameters used in different simulations are shown in Table 2.1 and Table 2.2.

2.4.2 Double slope chute

The data of these laboratory experiments are collected from Hutter et al. (12).

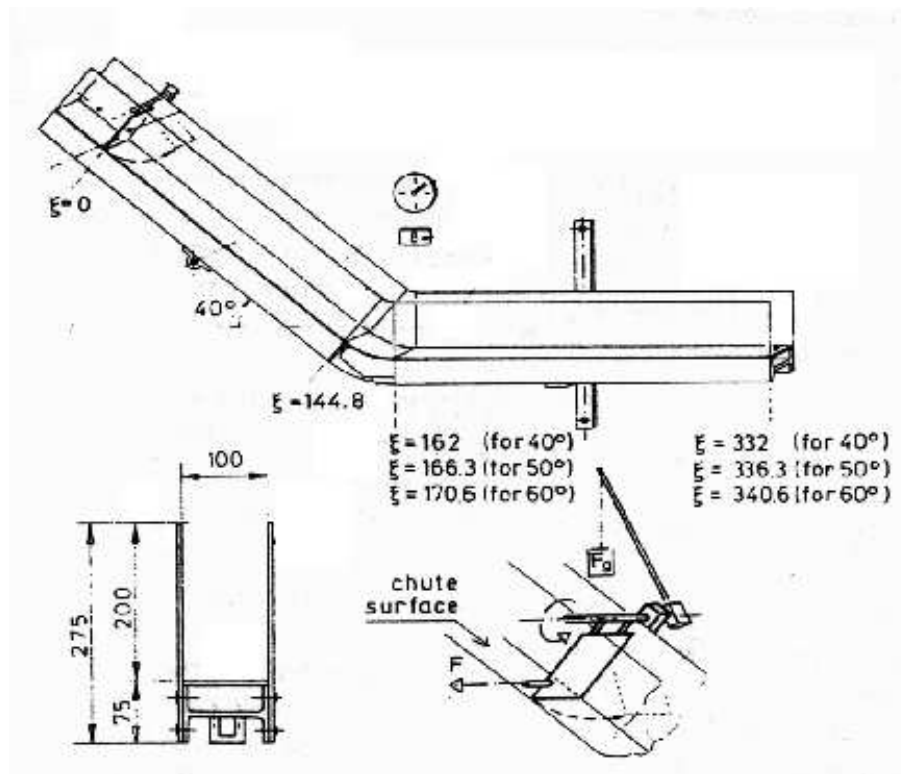


Figure 2.11: The experimental apparatus used by Hutter et al. (From (12)).

The experimental chute is made up of two straight segments, connected by a curved replaceable one. The first segment has an inclination angle adjustable from 40° to 60° ; the second one is horizontal (see Figure 2.11). The bottom, in PVC, can be covered with different linings (drawing paper or sandpaper), in order to modify the basal roughness. One side wall is in plexiglass to make it possible to photograph. The other one is in PVC, coated with a gray plastic folio. The mass is held in its initial position by a gate, kept normal to the bottom by a bolt. When the bolt is removed, the gate rotates around a horizontal axis, dragged by the angular momentum exerted by a weight, hung to a lever arm applied at the axle of the gate. The mass is instantaneously released on the inclined segment and comes to a complete stop on the horizontal one.

One-dimensional models have been tested against *exp.29*, executed by releasing a mass of 500 g of Vestolen, a granular material made up of white plastic particles of lense-

type shape (diameter 4 mm , height 2.5 mm , density 950 kg/m^3 and highest bulk density 540 kg/m^3). The measured internal friction angle ϕ is $29^\circ - 36^\circ$. Using different procedures to estimate the bottom friction angle on PVC, Hutter et al. obtained $\delta_b = 19.0^\circ \pm 2.0$ and $\delta_b = 22.5^\circ$. No information is supplied on the values of the lateral friction angle at the frontal and back wall sides.

The initial shape of the released mass is assumed to be triangular with an horizontal upper surface, as in Figure 2.12. The geometrical scales L_s and H_s are assumed equal to the initial length of the mass 0.149 m . The width of the chute 0.1 m is assigned to the transversal geometrical scale B_s . The scale for velocity is $U_s = \sqrt{gH_s} = 1.21\text{ m/s}$ and so the scale for time results $T_s = L_s/U_s = 0.12\text{ s}$.

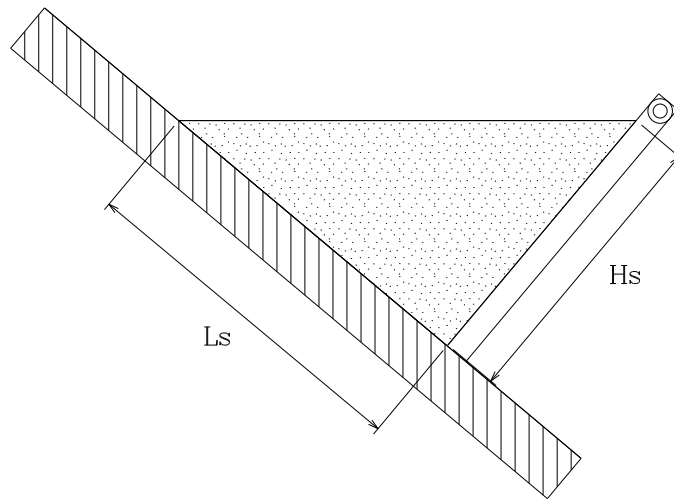


Figure 2.12: Initial shape of the granular mass.

Simulation	$\phi[^\circ]$	$\delta[^\circ]$	$k[-]$
h.1d.1	29	19.5	0
h.1d.2	29	19.5	0.453

Table 2.3: Values of the rheological parameters used in the numerical simulations of the experiment of Hutter et al. (12) with the one-dimensional model with constant width (1d). ϕ is the internal friction angle, δ the bottom friction angle, k the coefficient of the corrective factor of δ proposed by Savage and Hutter (28) (see equation (2.18)).

2. A one-dimensional model with variable width

Simulation	ϕ [$^\circ$]	δ_b [$^\circ$]	δ_l [$^\circ$]	δ_r [$^\circ$]
h.1dwvar.1	29	19.5	0	0
h.1dwvar.2	29	19.5	19.5	14

Table 2.4: Values of the rheological parameters used in the numerical simulations of the experiment of Hutter et al. (12) with the one-dimensional model with variable width (*1dwvar*). ϕ is the internal friction angle, δ_b the bottom friction angle, δ_l and δ_r are the lateral friction angles at left and right sides respectively.

Hutter et al. obtained the best numerical simulations using $\phi = 26^\circ$, $\delta = 19.5^\circ$ and $k = 0$ (see (12)). In Figure 2.13 the temporal evolution of the position of the front and the rear of the mass for *exp.29* is compared to numerical simulations obtained neglecting lateral friction. During the flowing phase the computed mass is more spread than in experimental data, while during the run-out phase roles are inverted, so that the computed final length results underestimated with respect to experimental data. Best results are given by the *1dwvar* model.

Applying to δ the correction given by equation (2.18), with $k = 0.453$, in the *1d* model, and using the lateral friction angles $(\delta)_{l/r} = 18^\circ$ in *1dwvar*, numerical simulations give worse predictions of the final position of the front and better predictions of the final position of the rear and of the mean position of the deposit (see Figure 2.14); the final length remains nearly the same as in cases without lateral friction. Model *1dwvar* returns better fittings again.

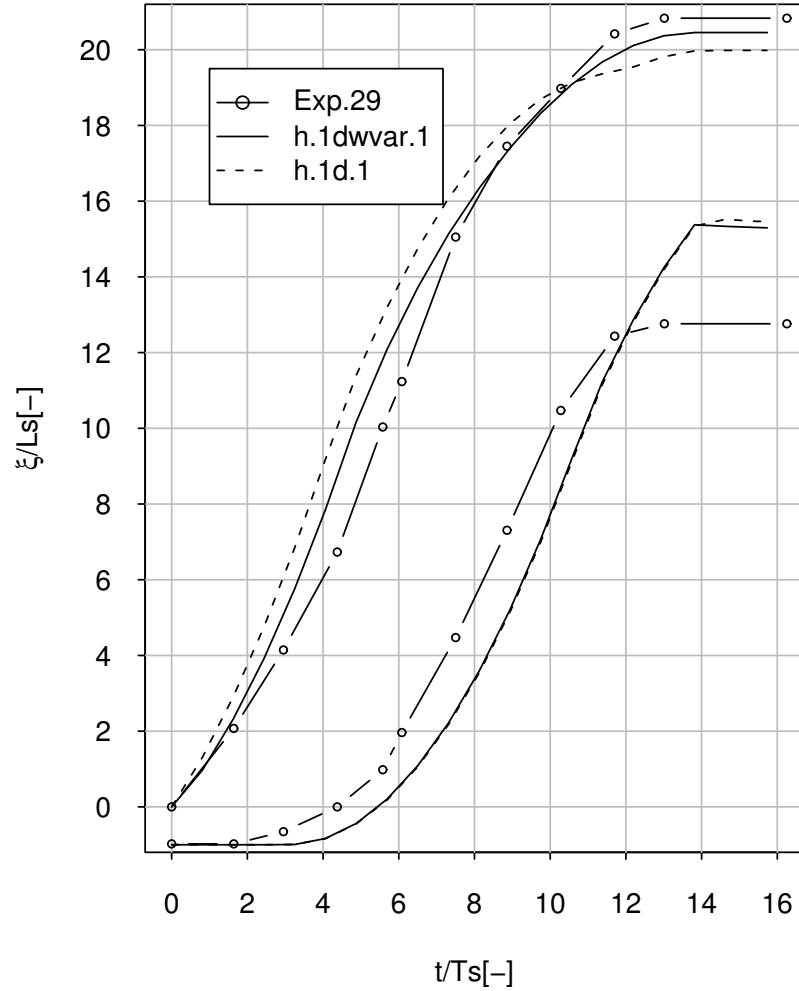


Figure 2.13: Double slope chute. Positions of the front and the rear of the mass plotted versus time for *exp.29*. Comparison between experimental data and numerical simulations produced by the one-dimensional models with constant width (*1d*) and variable width (*1dwvar*), with no lateral friction at the lateral banks. The values of the rheological parameters used in different simulations are shown in Table 2.3 and Table 2.4. The curvilinear coordinate ξ is non dimensionalized through $L_s = 0.149\text{ m}$, the initial length of the mass, time through $T_s = \sqrt{L_s/g} = 0.12\text{ s}$.

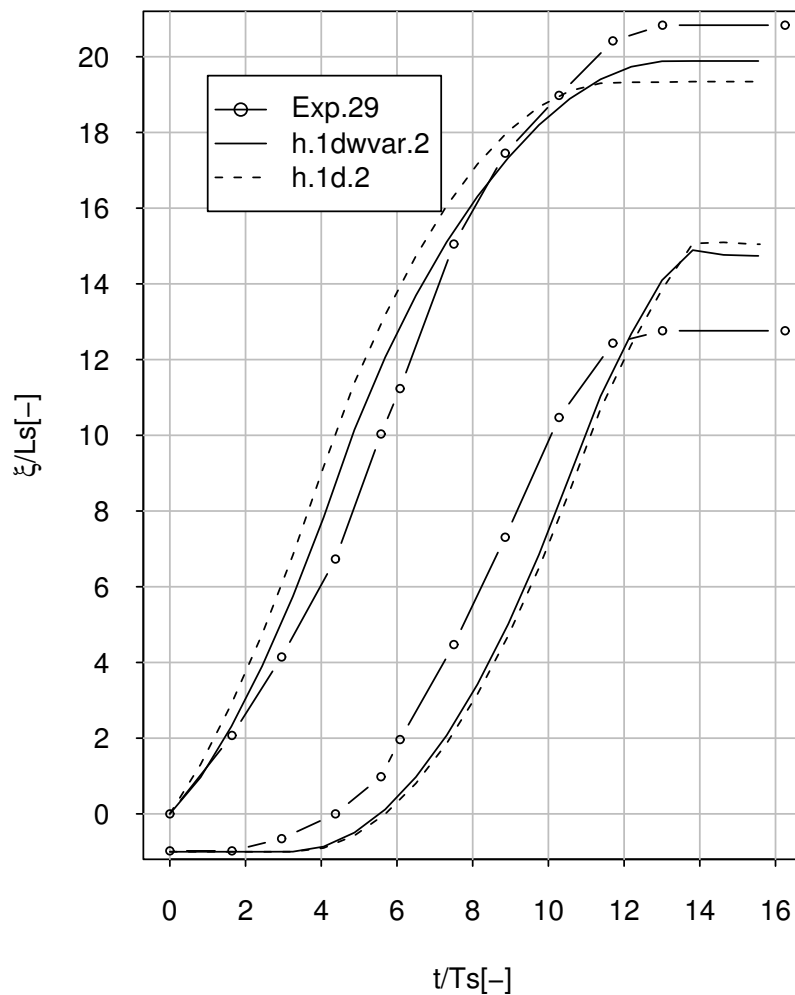


Figure 2.14: Double slope chute. Positions of the front and the rear of the mass plotted versus time for *exp.29*. Comparison between experimental data and numerical simulations produced by the one-dimensional models with constant width (*1d*) and variable width (*1dwvar*), adding lateral friction at the lateral banks. The values of the rheological parameters used in different simulations are shown in Table 2.3 and Table 2.4. The curvilinear coordinate ξ is non-dimensionalized through $L_s = 0.149\text{ m}$, the initial length of the mass, time through $T_s = \sqrt{L_s/g} = 0.12\text{ s}$.

2.4.3 Convex and concave curved chute

The experiments of Greve and Hutter (10) were executed in a convex and concave curved chute, 0.1 m wide and 4 m long. The inclination angle $\beta[^\circ]$, as function of the dimensionless arc length $\widehat{\xi} = \xi/L_s$, with $L_s = 0.150$ m, is given by:

$$\beta(\widehat{\xi}) = \beta_0 e^{-0.1\widehat{\xi}} + \beta_1 \frac{\gamma}{1 + \gamma^8} - \beta_2 e^{-0.3(\widehat{\xi}+10/3)^2}, \quad \text{with} \quad (2.20)$$

$$\gamma = \frac{4}{15} (\widehat{\xi} - 9), \quad \text{and}$$

$$\beta_0 = 60.0^\circ, \quad \beta_1 = 31.4^\circ, \quad \beta_2 = 37.0^\circ.$$

The bed geometry in the $(\widehat{x}, \widehat{z})$ -absolute dimensionless coordinate system is obtained by the integration:

$$\widehat{x}(\widehat{\xi}) = \int_0^{\widehat{\xi}} \cos \beta(\tau) d\tau + \widehat{x}_0, \quad \widehat{z}(\widehat{\xi}) = \int_0^{\widehat{\xi}} -\sin \beta(\tau) d\tau + \widehat{z}_0.$$

The trend of β as function of the dimensional absolute coordinate x is shown in Figure 2.15. The second term in equation (2.20) is responsible for the deviation from the exponential tendency. The result is a bump in the exponential geometry of the bed (see Figure 2.16).

The bottom of the chute consists of a flexible strip of plexiglass. To change the bed friction angle δ , Greve and Hutter covered it with no. 120 SIA sandpaper or drawing paper linings. One wall is in transparent plexiglass in order to make it possible to photograph the motion of the granular material. No information is given about the other wall. The mass is released on the incline by rotating the confining gate, initially oriented in the vertical direction. Mass is supposed to have an initial triangular shape. Longitudinal and normal scales, L_s and H_s , are assumed equal to the initial length and depth of the mass. The velocity scale is $U_s = \sqrt{g H_s}$ and the time scale $T_s = L_s/U_s$.

Only three of the experiments carried out by Greve and Hutter are reported here.

In *exp.16* a mass of 1.5 l of Vestolen, the same granular material seen in §2.4.2, is released on the chute, having the bottom lined with no. 120 sandpaper. Greve and Hutter provide the experimentally estimated values of $37.0^\circ \pm 2.0^\circ$ and $34.6^\circ \pm 2.0^\circ$ for the internal friction angle ϕ and the bottom friction angle δ respectively. They used $\phi = 37^\circ$, $\delta = 29^\circ$, $k_w = 11^\circ$ in the numerical simulation.

In Figure 2.17 the positions of the rear, the front and the maximum height are plotted versus time. Figure 2.18 shows the temporal evolution of the maximum height h . The lon-

2. A one-dimensional model with variable width

Experiment	Simulation	ϕ [°]	δ [°]	k_w [°]	k
exp.16	g16.1d.1	37	29	11	-
exp.29	g29.1d.1	37	26.5	11	-
exp.29	g29.1d.2	37	26.5	-	0.4
exp.36	g36.1d.1	44	30	12	-

Table 2.5: Values of the rheological parameters used in the numerical simulations of the experiments of Greve and Hutter (10) with the one-dimensional model with constant width ($1d$). ϕ is the internal friction angle, δ the bottom friction angle, k_w the coefficient of the corrective factor of δ proposed by Greve and Hutter (10) (see equation (2.19)), k the coefficient of the corrective factor of δ proposed by Savage and Hutter (28) (see equation (2.18)).

Experiment	Simulation	ϕ [°]	δ_b [°]	δ_l [°]	δ_r [°]
exp.16	g16.1dwvar.1	37	30	15	15
exp.29	g29.1dwvar.1	37	26.5	26.5	26.5
exp.36	g36.1dwvar.1	44	30	30	30

Table 2.6: Values of the rheological parameters used in the numerical simulations of the experiments of Greve and Hutter (10) with the one-dimensional model with variable width ($1dwvar$). ϕ is the internal friction angle, δ_b the bottom friction angle, δ_l and δ_r the lateral friction angles at left and right sides respectively.

itudinal curvilinear coordinate ξ is non-dimensionalised through $L_s = 0.375 m$, the maximum height h through $H_s = 0.08 m$ and the time t through $T_s = L_s/U_s = L_s/\sqrt{gH_s} = 0.42 s$. Using $\phi = 37^\circ$, $\delta_b = 30^\circ$ (closer to the experimental value) and $(\delta)_{l/r} = 15^\circ$, model $1dwvar$ shows a better behaviour than $1d$ model, both in the prediction of the position of the front and of the point of maximum height and in the prediction of the maximum height of the mass, during all the motion.

Exp.29 was carried out with 1.5 l of Vestolen on drawing paper. The measured basal friction angle is $24.7^\circ \pm 1.5^\circ$. The parameters used by Greve and Hutter in the numerical simulation are $\phi = 37^\circ$, $\delta = 26.5^\circ$ and $k_w = 11^\circ$. Model $1dwvar$ run with $\phi = 37^\circ$ and $\delta_{b/l/r} = 26.5^\circ$.

The results are shown in Figure 2.19, where h is non-dimensionalised through $H_s = 0.1 m$, ξ through $L_s = 0.3 m$, t through $T_s = L_s/U_s = L_s/\sqrt{gH_s} = 0.30 s$.

The presence of the convex bump in the middle of the chute causes the separation of

the granular avalanche in two parts: one part remains before the point of maximum slope along the bump, while the other one goes beyond it and stops in the segment at lower slope. The profiles produced by the one-dimensional models are later and deeper than the experimental ones. The *1d* model gives poorer results than the *1dwvar* model. Also the volume splitting over and under the bump is better simulated by the *1dwvar* model. Model *1d* overestimates the volume which stops on the bump.

Analogous considerations are valid for *exp.36*, shown in Figure 2.20, where, for the non-dimensionalization, the length scale is $L_s = 0.33\text{ m}$, H_s is 0.09 m and the time scale is $T_s = L_s/U_s = L_s/\sqrt{gH_s} = 0.35\text{ s}$. Experiment *exp.36* was performed with a mass of 1.5 l of *quartz 0*, having mean grain diameter of 3 mm , maximum length $l_{max} = 5.0\text{ mm}$, bulk density at densest packing $1562\text{ kg/m}^3 \pm 20\text{ kg/m}^3$ and density $2600\text{ kg/m}^3 \pm 150\text{ kg/m}^3$. The granular mass is released on the chute lined with drawing paper. The measured internal friction angle is $\phi = 44.0^\circ \pm 2.5^\circ$, the bottom friction angle $\delta = 31.1^\circ \pm 1.5^\circ$. The values of the numerical parameters used in model *1d* are the ones applied by Greve and Hutter: $\phi = 44^\circ$, $\delta = 30^\circ$ and $k_w = 12^\circ$. Model *1dwvar* gives the best numerical simulations with $\phi = 44^\circ$ and $\delta_{b/l/r} = 30^\circ$.

In this case, the model *1d* gives a better description of the maximum height, but the deposit volumes ratio is poorly reproduced, as in *exp.29*.

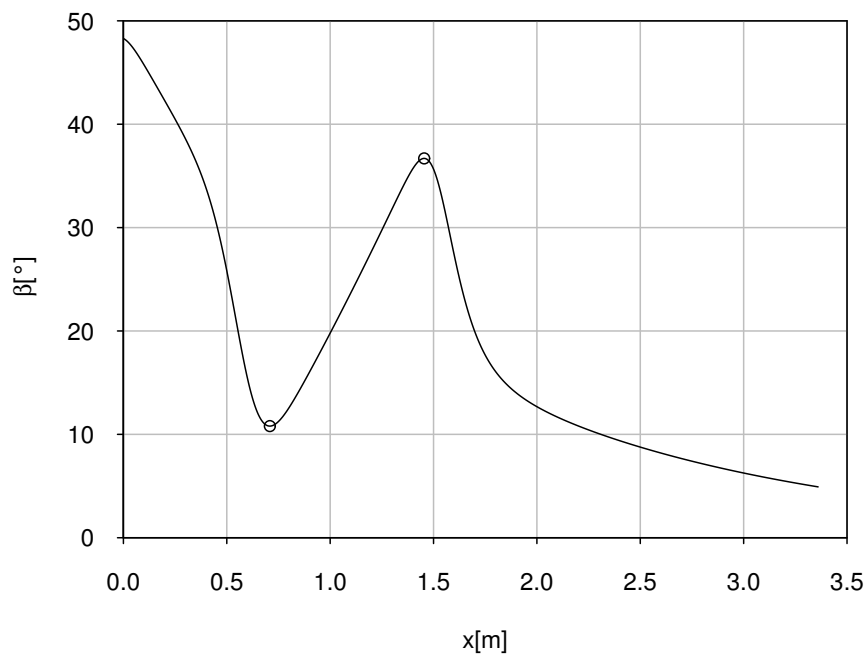


Figure 2.15: Convex and concave curved chute. The bed inclination angle $\beta[^\circ]$ versus the absolute dimensional coordinate $x[mm]$. The circles highlight the positions of maximum and minimum slope along the bump.

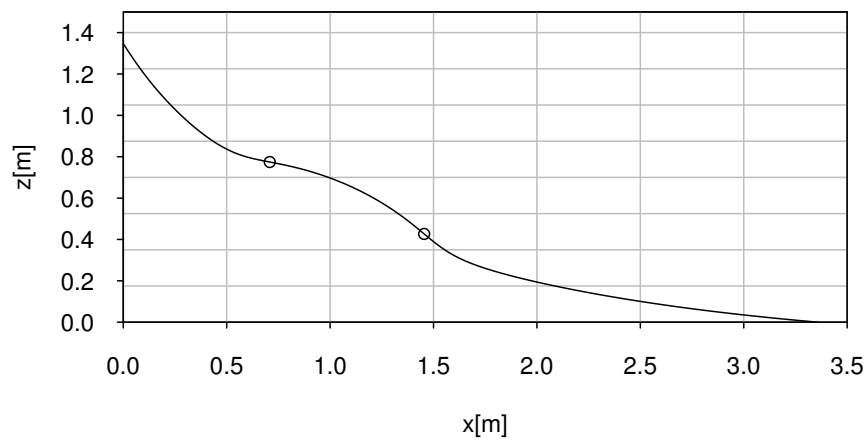


Figure 2.16: Convex and concave curved chute. The bed geometry in the (x, y) -absolute dimensional coordinate system. The circles highlight the positions of maximum and minimum slope along the bump.

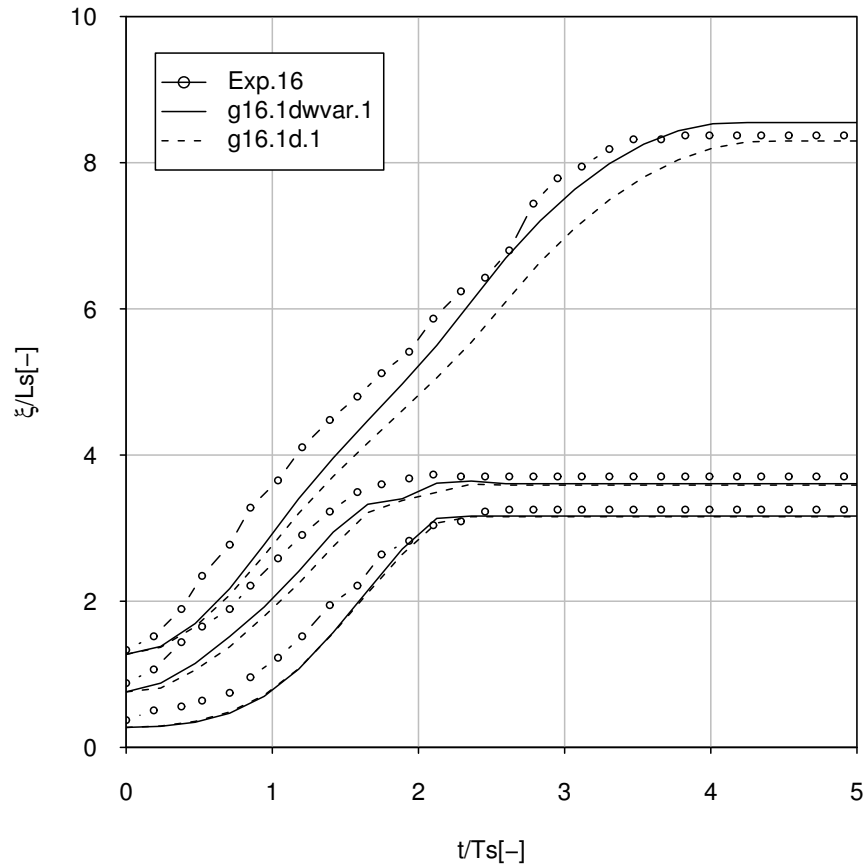


Figure 2.17: Convex and concave curved chute. *Exp.16*. Position of the front, the rear and the maximum height of the mass. Comparison of experimental data and numerical simulations of models *1d* and *1dwvar*, with the numerical parameters shown in Table 2.5 and Table 2.6. ξ is non-dimensionalized through $L_s = 0.375\text{ m}$, time t through $T_s = L_s/U_s = L_s/\sqrt{gH_s} = 0.42\text{ s}$, being $H_s = 0.08\text{ m}$.

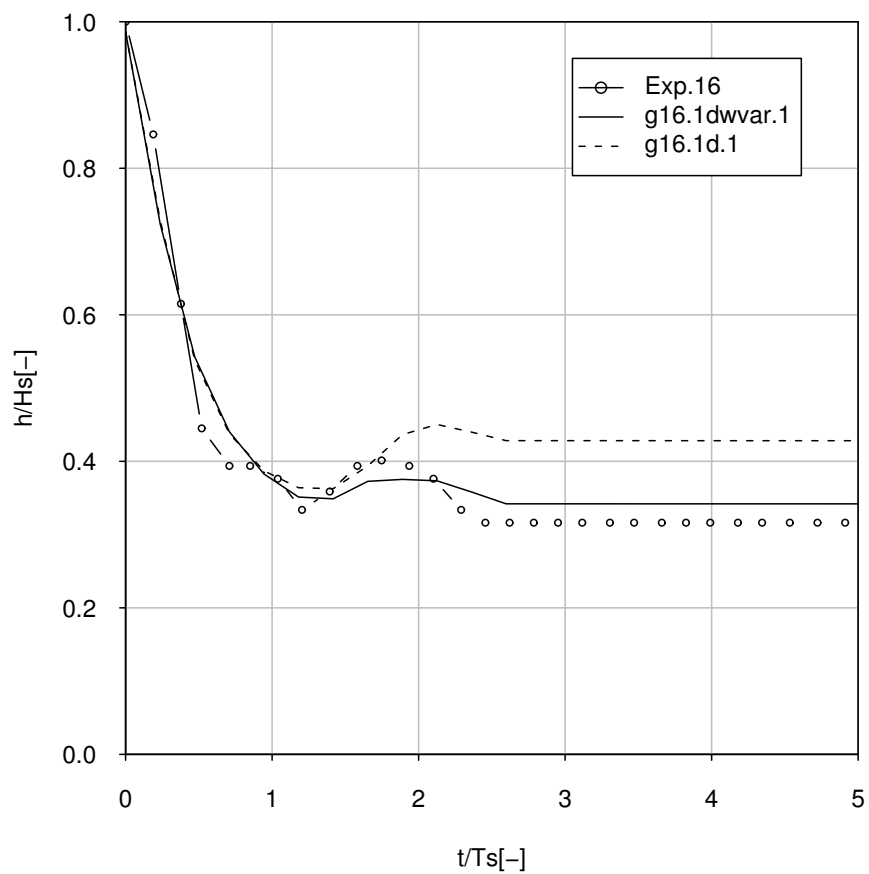


Figure 2.18: Convex and concave curved chute. *Exp.16*. Temporal evolution of the maximum depth of the granular mass. Comparison of experimental data and numerical simulations of models *1d* and *1dwvar*, with the numerical parameters shown in Table 2.5 and Table 2.6. h is non-dimensionalized through $H_s = 0.08\text{ m}$, time t through $T_s = L_s/U_s = L_s/\sqrt{gH_s} = 0.42\text{ s}$, being $L_s = 0.375\text{ m}$.

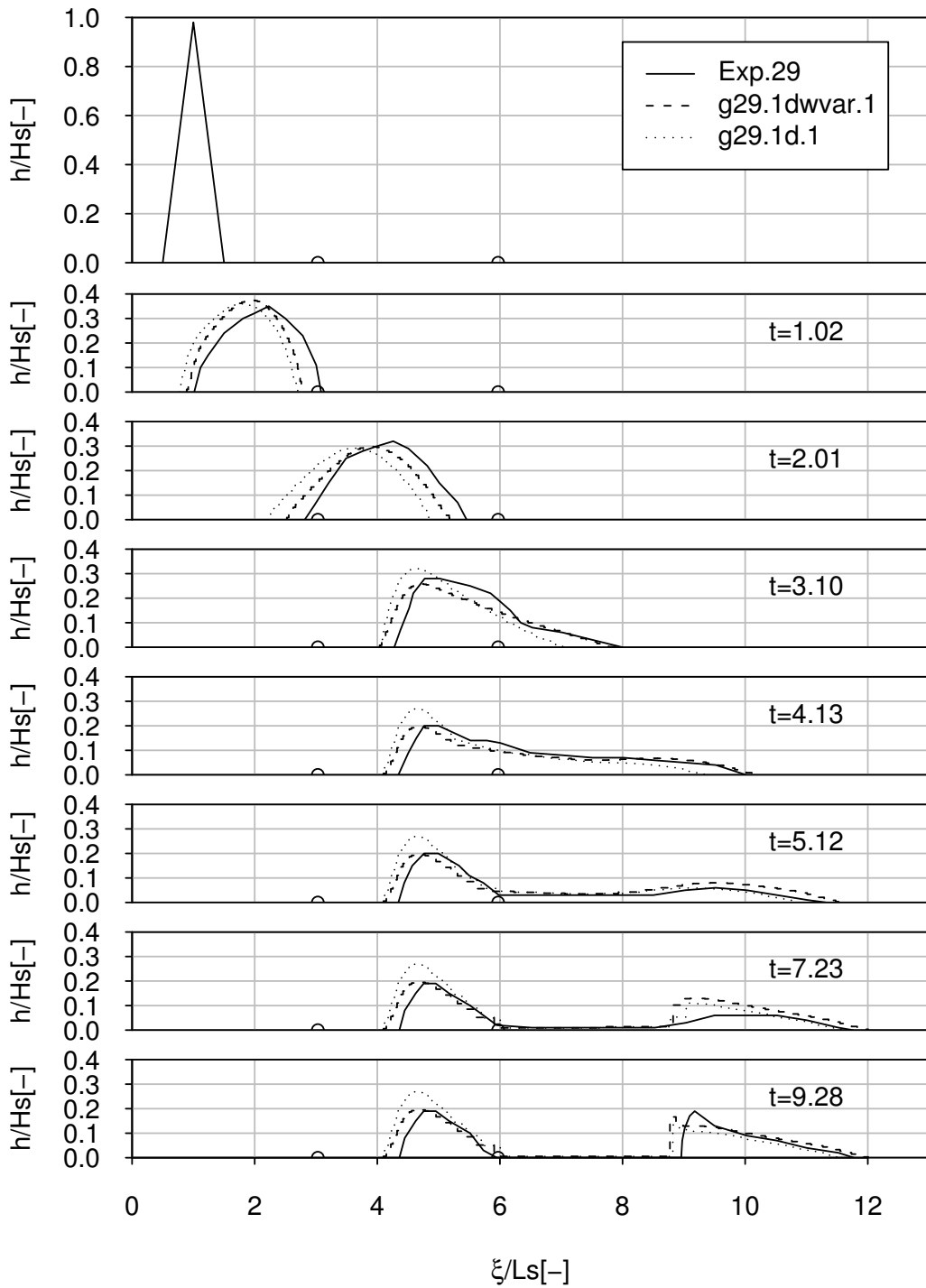


Figure 2.19: Convex and concave curved chute. *Exp.29*. Comparison of experimental and numerical profiles obtained with models *1d* and *1dwvar*, with the numerical parameters shown in Table 2.5 and Table 2.6. h is non-dimensionalized through $H_s = 0.1\text{ m}$, ξ through $L_s = 0.3\text{ m}$, t through $T_s = L_s/U_s = L_s/\sqrt{gH_s} = 0.30\text{ s}$. The circles signal the positions of points of maximum and minimum slope.

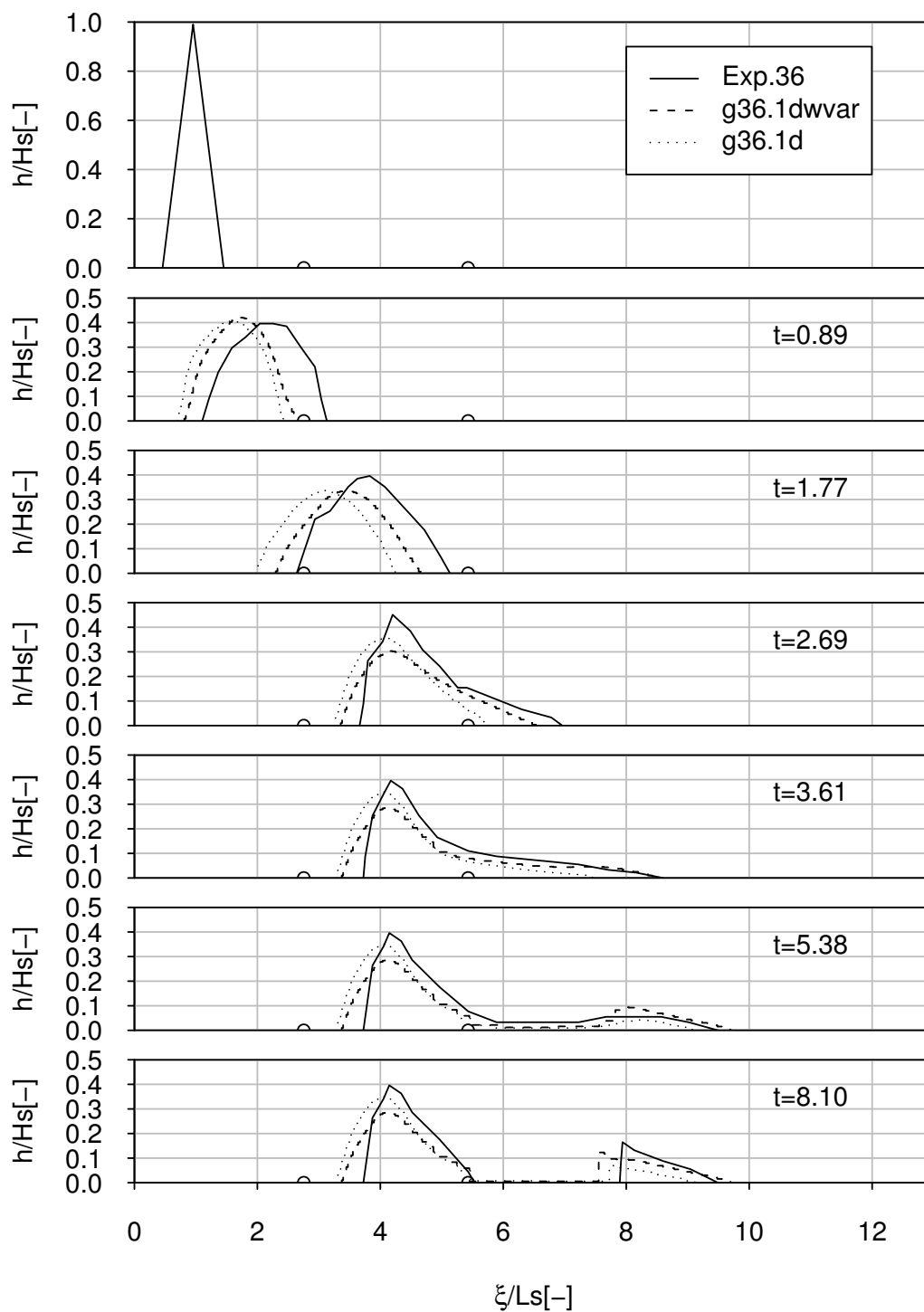


Figure 2.20: Convex and concave curved chute. *Exp.36*. Comparison of experimental and numerical profiles obtained with models *1d* and *1dwvar*, with the numerical parameters shown in Table 2.5 and Table 2.6. h is non-dimensionalized through $H_s = 0.09\text{ m}$, ξ through $L_s = 0.33\text{ m}$, the time t through $T_s = L_s/U_s = L_s/\sqrt{gH_s} = 0.35\text{ s}$. The circles signal the positions of the points of maximum and minimum slope.

2.4.4 Concluding remarks

In all the reported cases with constant width, by applying the values of the physical parameters which gave the best fittings to Hutter et al. (12) and Greve et al. (10), *1dwvar* model showed a better behaviour than *1d* model. Nevertheless, to verify definitively the effectiveness of the rheological hypotheses, it is necessary to test the *1dwvar* model on laboratory cases with known lateral friction angles and with converging and diverging side walls. An experimental campaign is being designed at the Hydraulic Laboratory of the University of Trento, in order to better investigate the effects of different lateral roughnesses and of a longitudinally varying width of the channel.

3 The two-dimensional model

Extending the theory of Savage and Hutter (27) to the two-dimensional case, Hutter et al. (13) developed a model based on a curvilinear coordinate system, which applies to topographies with small lateral curvature. The definition of a curvilinear coordinate system is not so obvious with arbitrarily complex topographies, especially if it is not possible to identify an unique thalweg line.

A two dimensional model has been written in an absolute orthogonal coordinate system at the Department of Civil and Environmental Engineering of Trento by De Toni (5). A detailed description of the model is in De Toni et al. (6). The behaviour of the model has been thoroughly investigated and some corrections have been applied.

3.1 The original model

Initially, the equations of motion have been written in a non-ortho-normal curvilinear system, relevant to the topographical surface, through the techniques of the tensorial analysis. The equation written in the direction normal to the bottom, simplified according to the hypothesis of “shallow water”, provides the hydrostatic pressure distribution, with an added centrifugal term. The stress tensor is then defined in a different ortho-normal coordinate system, relevant to the direction of the velocity vector. Afterward the equations of motion have been written in a (x, y, z) -ortho-normal coordinate system with z oriented along the vertical, rotating the stress tensor previously defined. Finally, assuming that the velocity is constant and the pressure distribution is linear along the vertical direction z instead of normally to the bottom, the motion equations are averaged over z .

3.1.1 The three-dimensional motion equations

The continuity equation and the momentum balance for an incompressible continuum in vectorial form are:

$$\begin{aligned}\nabla \cdot \mathbf{u} &= 0, \\ \rho \frac{d\mathbf{u}}{dt} &= \rho (\mathbf{u}_{,t} + \mathbf{u} \cdot \nabla \mathbf{u}) = \mathbf{f} + \nabla \cdot \mathbf{P},\end{aligned}\tag{3.1}$$

where \mathbf{u} is the velocity vector, ρ is constant density, \mathbf{f} is the external force per unit volume (the gravitational force $\rho \mathbf{g}$, with \mathbf{g} the gravity acceleration vector), \mathbf{P} is the stress tensor, with the convention of positive outward stress, t is the time. The notation $\partial_{,x}$ represents the partial derivative with respect to the generic variable x .

In the (x, y, z) -absolute coordinate system, with z orientated along the vertical, the geometries of the sliding and of the free surfaces are defined by the equations: $\Phi_b(\mathbf{x}) = b(x, y) - z = 0$ and $\Phi_f(\mathbf{x}, t) = z - f(x, y, t) = 0$, respectively, being \mathbf{x} the position vector. The kinematic boundary conditions take the form:

$$\mathbf{u}_b \cdot \nabla \Phi_b = 0 \quad \text{and} \quad \frac{\partial \Phi_f}{\partial t} + \mathbf{u}_f \cdot \nabla \Phi_f = 0,$$

where \mathbf{u}_f and \mathbf{u}_b are the velocity vectors at free surface and bed surface, respectively. The stress is assumed to be zero at the free surface while a Coulomb-type relation is used to describe the frictional interaction between the mass and the bottom surface. In this way the dynamic boundary conditions are given by:

$$\mathbf{P}_b \mathbf{n}_b - \mathbf{n}_b (\mathbf{n}_b \cdot \mathbf{P}_b \mathbf{n}_b) = + (\mathbf{u}_b / |\mathbf{u}_b|) \tan(\delta) (\mathbf{n}_b \cdot \mathbf{P}_b \mathbf{n}_b) \quad \text{and} \quad \mathbf{P}_f \mathbf{n}_f = \mathbf{0},$$

where δ is the bed friction angle and $\mathbf{n}_b = \nabla \Phi_b / |\nabla \Phi_b|$ and $\mathbf{n}_f = \nabla \Phi_f / |\nabla \Phi_f|$ are the normal outwards unit vectors at the bottom and at the free surface.

3.1.2 Internal pressure distribution

The equations of motion can be written in a non-ortho-normal curvilinear coordinate system with ζ normal to the slope and the coordinate lines ξ and η lying on the basal surface in planes normal to the y and x axis, respectively, as shown in Figure 3.1.

The equations of motion (3.1) can be written in the (ξ, η, ζ) -curvilinear coordinate system using the tensorial analysis techniques (Simmonds (31)). Applying the Einstein's summation convention, along the generic curvilinear coordinate x_i , one obtains:

$$\rho u^i_{,t} + \rho u^j \nabla_j u^i = f^i + \nabla_j p^{ij},$$

being:

$$\mathbf{u} = u^i \mathbf{g}_i,$$

$$\mathbf{f} = f^i \mathbf{g}_i,$$

$$\mathbf{P} = p^{ij} \mathbf{g}_i \mathbf{g}_j,$$

$$\nabla = \mathbf{g}^k \nabla_k.$$

\mathbf{g}_i are the “cellar” base vectors, defined as:

$$\mathbf{g}_i = \frac{\partial \mathbf{x}}{\partial x_i},$$

where $\mathbf{x} = \mathbf{x}(x_1, x_2, x_3)$ represents the position vector of a generic point, written as function of the curvilinear coordinates x_i . The “cellar” base vectors define, locally, the directions of the curvilinear coordinate lines.

\mathbf{g}^i are the reciprocal base vectors, called “roof” base vectors. They are defined so that:

$$\mathbf{g}^i \cdot \mathbf{g}_j = \delta_j^i = \begin{cases} 1 & \text{if } i = j \\ 0 & \text{if } i \neq j \end{cases},$$

where the symbol δ_j^i is the Kronecker delta.

A generic vector \mathbf{u} can be represented through its “roof” components u^i , “physic” components $u^{(i)}$ or “cellar” components u_i :

$$\mathbf{u} = u^i \mathbf{g}_i = u^{(i)} \mathbf{g}_i / |\mathbf{g}_i| = u_i \mathbf{g}^i.$$

A second order tensor \mathbf{P} can be written as follows:

$$\mathbf{P} = p^{ij} \mathbf{g}_j \mathbf{g}_i = p^{(ij)} \mathbf{g}_j \mathbf{g}_i / (|\mathbf{g}_j| |\mathbf{g}_i|) = p_{ij} \mathbf{g}^i \mathbf{g}^j.$$

∇_k is called the covariant derivative with respect to x_k . The covariant derivative of the roof component u^i of a vector \mathbf{u} can be defined using the Christoffel symbols Γ_{ij}^k :

$$\nabla_j u^i = u^i{}_{,j} + \Gamma_{jk}^i u^k.$$

For the roof components p^{ij} of a tensor \mathbf{P} :

$$\nabla_k p^{ij} = p^{ij}{}_{,k} + \Gamma_{lk}^i p^{lj} + \Gamma_{lk}^j p^{il}.$$

where:

$$\Gamma_{ij}^k = \mathbf{g}_{i,j} \cdot \mathbf{g}^k.$$

It can be demonstrated that $\Gamma_{ij}^k = \Gamma_{ji}^k$.

The momentum equation along ζ is non-dimensionalized by scaling with the characteristic parameters of the phenomenon: L_s for the geometrical dimensions of the mass along x , y , ξ and η directions; H_s for the flow depth; P_s for the pressure terms; T_s for the time; U_s and $U_{\zeta s}$ for the velocity components along and normal to the sliding surface respectively; ρ_s for the density. The maximum altitude difference covered by the avalanche is

3. The two-dimensional model

considered comparable with L_s . It is assumed that $\varepsilon = H_s/L_s$ is small (“shallow water” hypothesis) and that $T_s = L_s/U_s = H_s/U_{\zeta s}$. It follows that $U_{\zeta s} = \varepsilon U_s$. The pressure and the inertial terms are assumed to be of the same order of magnitude as gravitational forces, i.e. $P_s \approx \rho_s U_s^2 \approx \rho_s g L_s$.

It can be demonstrated (see De Toni et al. (6)) that, neglecting the terms of order ε , the vectors of the “cellar” base are:

$$\begin{aligned}\mathbf{g}_\xi &= \frac{1}{\sqrt{1+b_{,x}^2}\Big|_{\eta=0}} (1, 0, b_{,x}) , \\ \mathbf{g}_\eta &= \frac{1}{\sqrt{1+b_{,y}^2}\Big|_{\xi=0}} (0, 1, b_{,y}) , \\ \mathbf{g}_\zeta &= \frac{1}{\sqrt{1+b_{,x}^2+b_{,y}^2}} (-b_{,x}, -b_{,y}, 1)\end{aligned}$$

and that “roof” base vectors are given by:

$$\begin{aligned}\mathbf{g}^\xi &= \frac{\sqrt{1+b_{,x}^2}\Big|_{\eta=0}}{1+b_{,x}^2+b_{,y}^2} (1+b_{,y}^2, -b_{,x}b_{,y}, b_{,x}) , \\ \mathbf{g}^\eta &= \frac{\sqrt{1+b_{,y}^2}\Big|_{\xi=0}}{1+b_{,x}^2+b_{,y}^2} (-b_{,x}b_{,y}, 1+b_{,x}^2, b_{,y}) , \\ \mathbf{g}^\zeta &= \mathbf{g}_\zeta .\end{aligned}$$

$\Gamma_{\zeta\zeta}^k$ is identically 0 and the dimensional analysis reveals that $\Gamma_{i\xi}^k = \Gamma_{\xi i}^k$ and $\Gamma_{i\eta}^k = \Gamma_{\eta i}^k$ are of order $1/L_s$. Hence, discarding the terms of order ε , the motion equation along ζ results:

$$\rho \left[\Gamma_{\xi\xi}^\zeta (u^\xi)^2 + 2\Gamma_{\xi\eta}^\zeta u^\xi u^\eta + \Gamma_{\eta\eta}^\zeta (u^\eta)^2 \right] = -\frac{\rho g}{\sqrt{1+b_{,x}^2+b_{,y}^2}} + p^{\zeta\zeta}_{,\zeta} . \quad (3.2)$$

According to the “plug-flow” hypothesis, the velocity vector is considered constant along the depth and so equation (3.2), integrated over ζ , gives a linear pressure profile. It can

be written in terms of the physical components of velocity and stress tensor:

$$\begin{aligned}
 p^{(\zeta\zeta)} &= -\frac{\rho (\tilde{h} - \zeta)}{\sqrt{1 + b_{,x}^2 + b_{,y}^2}} \left(g + \frac{b_{,xx}}{1 + b_{,x}^2} (u^{(\xi)})^2 + \frac{b_{,xy}}{\sqrt{1 + b_{,x}^2} \sqrt{1 + b_{,y}^2}} u^{(\xi)} u^{(\eta)} + \right. \\
 &\quad \left. + \frac{b_{,yy}}{1 + b_{,y}^2} (u^{(\eta)})^2 \right) \\
 &= -\rho A \left(1 - \frac{\zeta}{\tilde{h}} \right),
 \end{aligned} \tag{3.3}$$

where \tilde{h} is the normal depth of the granular mass and A collects all the terms not explicitly shown.

3.1.3 Mohr–Coulomb closure

The simulation of the dynamic of granular materials is dramatically affected by the choice of the rheological closure law. In our one-dimensional model, the rheology of Savage and Hutter (27) has been successfully tested with experimental data. The extension of this theory to two dimensions is not straightforward.

The first step is to find the principal directions of the stress tensor. Pudasaini and Hutter (23) chose the plane defined by ζ and the thalweg direction as main principal surface. We opted for the plane passing through ζ , normal to the bed, and Ξ . During the motion, Ξ is oriented along the direction of the velocity vector (Figure 3.2). When the mass is at rest, Ξ is chosen along the projection, on the sliding surface, of the gradient of the free surface elevation in the xyz reference system. In this way the basal frictional shear stress, $p_{\zeta\Xi}$, is precisely directed opposite to the velocity during the motion and the definition of the stress tensor is independent of the topography and the position of the thalweg line. H is normal to Ξ and ζ .

Assuming H to be a principal direction means that $p^{(\Xi H)} = p^{(H\Xi)} = p^{(\zeta H)} = p^{(H\zeta)} = 0$. The secondary circulations, normal to the mean direction of the motion, are likely to be small, except for cases with abrupt deviations. Hence, $\partial u^{(H)}/\partial \Xi$ and $\partial u^{(H)}/\partial \zeta$ and related shear stresses, $p^{(\Xi H)}$ and $p^{(\zeta H)}$, are negligible.

On the plane $\Xi\zeta$, using the rheological theory of Savage and Hutter (27), the stress tensor components at the bottom are linearly depending on $(p^{(\zeta\zeta)})_b$ (the subscript b means evaluated at the bottom). If we consider $(p^{(HH)})_b = k_2 (p^{(\zeta\zeta)})_b$, then the entire stress tensor is proportional to $(p^{(\zeta\zeta)})_b$. Hence, in the coordinate system $\Xi H\zeta$, the components

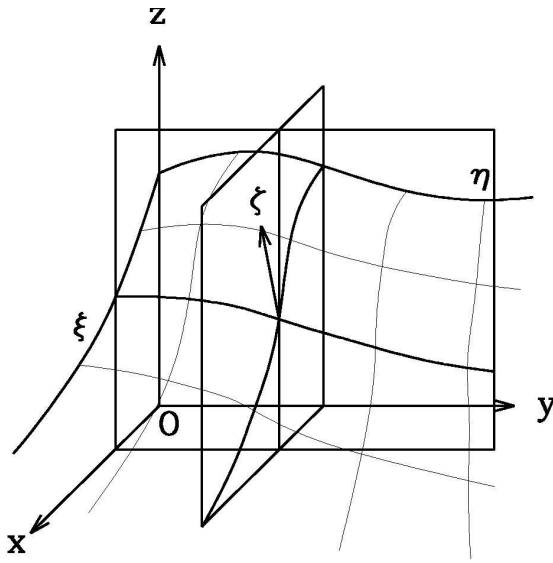


Figure 3.1: Absolute and curvilinear coordinate systems.

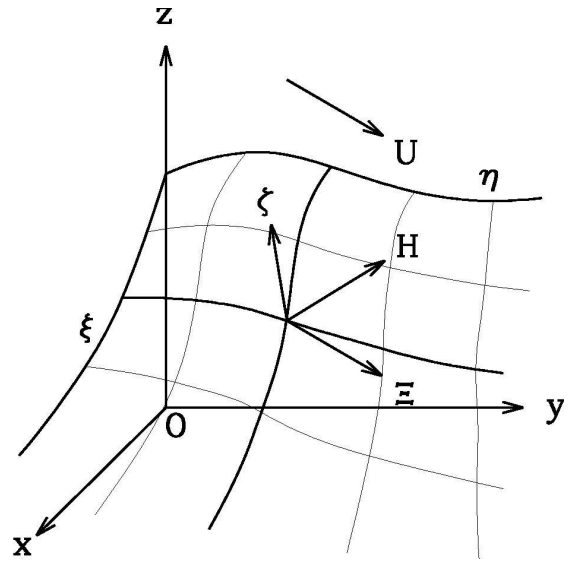


Figure 3.2: Local coordinate system $\Xi H \zeta$ relevant to the velocity vector, adopted to define the stress tensor.

of the stress tensor at the bottom are:

$$\begin{aligned}
 (\mathbf{P})_b &= \begin{pmatrix} p^{(\Xi \Xi)} & p^{(H \Xi)} & p^{(\zeta \Xi)} \\ p^{(\Xi H)} & p^{(HH)} & p^{(\zeta H)} \\ p^{(\Xi \zeta)} & p^{(H \zeta)} & p^{(\zeta \zeta)} \end{pmatrix} \Big|_b = \\
 &= \begin{pmatrix} k_{a/p} & 0 & \tan \delta \\ 0 & k_2 & 0 \\ \tan \delta & 0 & 1 \end{pmatrix} (p^{(\zeta \zeta)})_b = \tilde{\mathbf{K}} (p^{(\zeta \zeta)})_b. \tag{3.4}
 \end{aligned}$$

The linear dependence of the stress tensor on $p_{\zeta \zeta}$, reported in equation (3.4), is assumed to hold inside the entire moving mass.

$k_{a/p}$ is defined according to the scheme shown in Figure 3.3. In particular:

$$\left. \begin{matrix} k_p \\ k_a \end{matrix} \right\} = \frac{2}{\cos^2 \phi} \left[1 \pm \sqrt{1 - \frac{\cos^2 \phi}{\cos^2 \delta}} \right] - 1 \quad \text{if} \quad \begin{cases} \left(\frac{\partial u^{(\Xi)}}{\partial \Xi} \right)_b < 0 \\ \left(\frac{\partial u^{(\Xi)}}{\partial \Xi} \right)_b > 0 \end{cases},$$

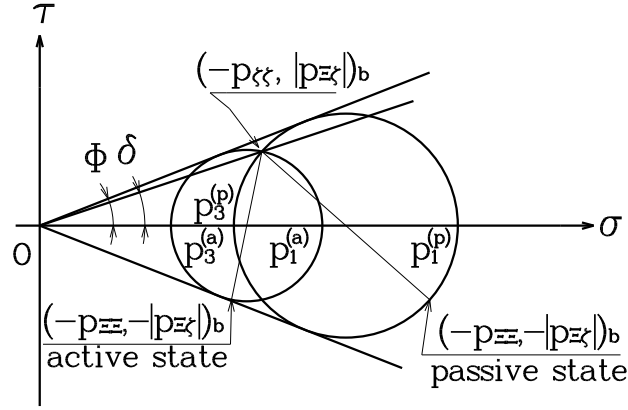


Figure 3.3: Definition scheme of the stress tensor components in the coordinate system $\Xi H \zeta$.

where ϕ and δ are the internal and bed friction angles, used to define the internal yield criterion and the bed-snow interaction.

The second step is to define the secondary principal stress in the direction H , normal to the main principal surface. Hutter et al. (13) relate $p^{(HH)}$ to the maximum or the minimum principal stress, p_1 and p_3 :

$$p^{(HH)} = p_2 = k_2 p^{(\zeta\zeta)} = \begin{cases} p_1 = k_1 p^{(\zeta\zeta)} & \text{if } \left(\frac{\partial u^{(H)}}{\partial H} \right)_b < 0 \\ p_3 = k_3 p^{(\zeta\zeta)} & \text{if } \left(\frac{\partial u^{(H)}}{\partial H} \right)_b > 0 \end{cases}. \quad (3.5)$$

If $(\partial u^{(\Xi)}/\partial \Xi)_b > 0$, i.e. in active stress state:

$$k_2 = \begin{cases} k_1^{(a)} \\ k_3^{(a)} \end{cases} = \frac{1 \pm \sin \phi}{\cos^2 \phi} \left(1 - \sqrt{1 - \frac{\cos^2 \phi}{\cos^2 \delta}} \right) \quad \text{if } \left(\frac{\partial u^{(H)}}{\partial H} \right)_b \begin{matrix} < \\ > \end{matrix} 0.$$

$k_1^{(a)} = p_1^{(a)}/p^{(\zeta\zeta)}$, $k_3^{(a)} = p_3^{(a)}/p^{(\zeta\zeta)}$, (see Figure 3.3 for $p_1^{(a)}$ and $p_3^{(a)}$).

If $(\partial u^{(\Xi)}/\partial \Xi)_b < 0$, i.e. in passive stress state:

$$k_2 = \begin{cases} k_1^{(p)} \\ k_3^{(p)} \end{cases} = \frac{1 \pm \sin \phi}{\cos^2 \phi} \left(1 + \sqrt{1 - \frac{\cos^2 \phi}{\cos^2 \delta}} \right) \quad \text{if } \left(\frac{\partial u^{(H)}}{\partial H} \right)_b \begin{matrix} < \\ > \end{matrix} 0,$$

where $k_1^{(p)} = p_1^{(p)}/p^{(\zeta\zeta)}$, $k_3^{(p)} = p_3^{(p)}/p^{(\zeta\zeta)}$ (see Figure 3.3 for $p_1^{(p)}$ and $p_3^{(p)}$).

3.1.4 The integrated equations of motion

The vertically averaged velocity components in the x and y directions of the absolute coordinate system are defined as:

$$U_x = \frac{1}{h} \int_b^f u_x dz, \quad U_y = \frac{1}{h} \int_b^f u_y dz,$$

where h is the vertical depth of the mass.

The vertically integrated continuity equation, taking into account the kinematic boundary conditions, reduces to:

$$h_{,t} + (h U_x)_{,x} + (h U_y)_{,y} = 0.$$

In order to integrate the momentum conservation equations along z it is necessary to know the stress tensor over the entire profile. Equation (3.4), which, strictly speaking, holds only at the bottom, is assumed to be valid over the entire flow depth. Furthermore velocity is assumed uniform along z , instead of along ζ . Similarly the hydrostatic distribution (3.3) is considered to hold along the vertical direction. Under these hypotheses, taking into account the kinematic and dynamic boundary conditions at the bottom and free surface, the integration of the momentum balance equations along x and y gives:

$$\begin{aligned} \frac{dU_x}{dt} &= U_{x,t} + U_x U_{x,x} + U_y U_{x,y} = ((k_{xx,x} + k_{yx,y}) A + k_{xx} A_{,x} + k_{yx} A_{,y}) \frac{h}{2} + \\ &\quad + (k_{xx} h_{,x} + k_{yx} h_{,y}) A + \\ &\quad + (k_{xx} b_{,x} + k_{yx} b_{,y} - k_{zx}) A, \\ \frac{dU_y}{dt} &= U_{y,t} + U_x U_{y,x} + U_y U_{y,y} = ((k_{xy,x} + k_{yy,y}) A + k_{xy} A_{,x} + k_{yy} A_{,y}) \frac{h}{2} + \\ &\quad + (k_{xy} h_{,x} + k_{yy} h_{,y}) A \\ &\quad + (k_{xy} b_{,x} + k_{yy} b_{,y} - k_{zy}) A, \end{aligned}$$

where:

$$\mathbf{K} = \begin{pmatrix} k_{xx} & k_{xy} & k_{xz} \\ k_{yx} & k_{yy} & k_{yz} \\ k_{zx} & k_{zy} & k_{zz} \end{pmatrix}$$

is the stress coefficient tensor $\tilde{\mathbf{K}}$ (defined by equation (3.4)) rotated into the absolute coordinate system xyz .

3.1.5 The numerical model

The vertically averaged equations are solved by means of a lagrangian finite difference scheme. The granular mass is discretized through a triangular mesh (see Figure 3.4).

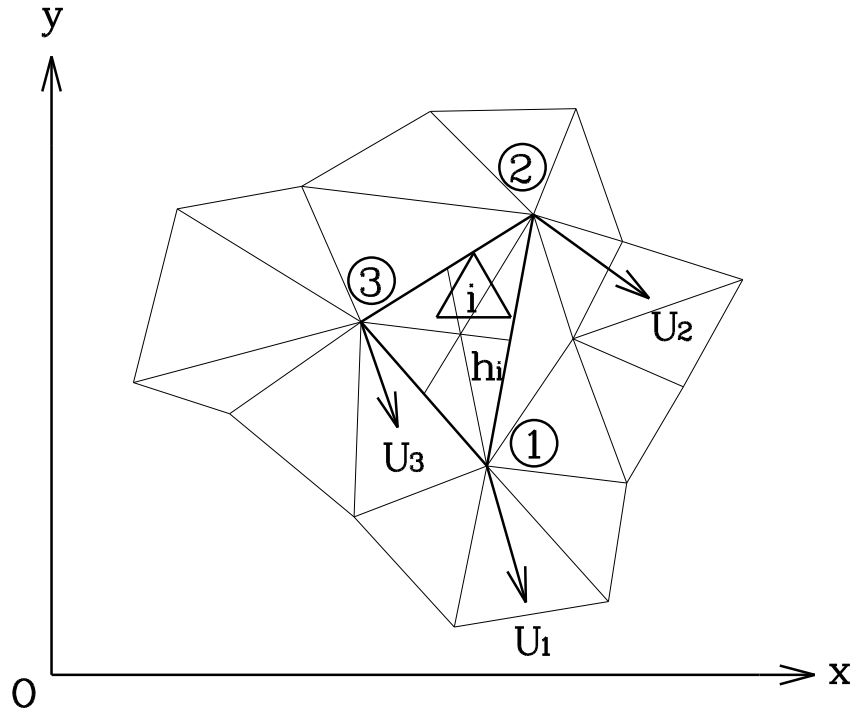


Figure 3.4: The triangular mesh which discretizes the fluid domain.

The values of the velocity vector U_i , defined at the vertexes of the mesh, are estimated by integrating the momentum balance equations along x and y through a two-step Collatz scheme (Stoer and Burlisch (32)). Node positions are then updated at every time step.

The vertical depth h_i is defined at each triangular cell of the mesh. The volume of every cell is kept constant to satisfy the continuity equation, so that, at each time step, the value of the vertical depth h_i is calculated dividing the volume by the area of the basal triangle.

The length of the time step Δt is varied during the simulation in order to fulfil a Courant–Levy–Friedrichs type stability condition. An artificial viscosity term is introduced in the momentum equations, to smooth numerical instabilities associated to shocks. The computational code is written in C++ and uses the library P2MESH (Bertolazzi and Manzini (3)) to manage the triangular mesh.

A detailed description of the mathematical and numerical model can be found in De Toni et al. (6).

3.2 The orientation of the absolute coordinate system

The comparison with experimental results obtained by Wieland et al. (34) on a chute with small lateral curvature shows a delay of the simulated profiles with respect to the experimental ones during the initial phases of the motion. Gray et al. (9) proposed a correction of the basal friction angle δ , in order to get best fittings with their two-dimensional model written in a curvilinear coordinate system. The same correction, applied to our model, gives poor reproductions of the final deposit. Tests performed with our model show that a better simulation of the initial phases of motion can be obtained orientating the xy plane along the surface that best approximates the bottom topography of the starting zone.

3.2.1 Chute with a small lateral curvature

Wieland et al. (34) performed their experiments on a chute constituted by an initiation zone, inclined at 40° on the horizontal, with shallow parabolic cross-slope section, smoothly connected to a flat horizontal run-out zone. The chute was constructed of steel sheet, wood and plaster, and was completely covered with paint, to have homogeneous frictional properties.

The granular material was released from a hemispherical cap.

Experiment *V05*, performed with rounded Vestolen plastic beads (diameters ranging from 2 mm to 3.5 mm , basal friction angle $\delta = 27^\circ$, internal friction angle $\phi = 33^\circ$), has been simulated numerically.

Our numerical model fails to reproduce correctly the initial phases of the motion, while fitting of last instants is excellent (see Figure 3.5, simulation *w.2d.1*). In Table 3.1 the values of the numerical parameters applied in the different simulations are reported.

Gray et al. (9) suggested to apply a corrective factor, which reduces the basal friction angle δ at the rear, in order to obtain a better prediction of its position at initial times:

$$\delta = \begin{cases} \delta_0 & \text{if } x \geq x_n - (x_n - x_r)/4 \\ \delta_0 - m_\delta (x_n - (x_n - x_r)/4 - x) & \text{if } x < x_n - (x_n - x_r)/4 \end{cases} \quad (3.6)$$

x_n and x_r identify the positions of the front and of the rear and x the position of the generic point along the mass. Applying the corrective term (3.6) to our model, with the values $m_\delta = 10^\circ/m$ suggested by Wieland et al. (34), the improvement in accuracy is limited to the initial phase, while the deposit is badly fitted (see Figure 3.5, simulation *w.2d.2*).

An offset in time equal to 0.2 s gives better results, except for the very initial instants.

Here, the position of the centre of mass is well predicted considering the time offset, but the longitudinal spreading is larger than in the experimental data (see Figure 3.6). This can be explained observing that, during the initial phase, the depth of the granular mass is comparable to its length, so that the hypothesis of “shallow water” decays. Furthermore, at steep slopes the deviation of the direction normal to the bottom from the vertical is large. Therefore the errors introduced by assuming the constancy of velocity and the linear distribution of stress tensor along z are likely not negligible.

Simulation	$m_\delta[^\circ/m]$	Time offset [s]	β_r
<i>w.2d.1</i>	0	0.0	0
<i>w.2d.2</i>	10	0.0	0
<i>w.2d.3</i>	0	0.2	0
<i>w.2d.4</i>	0	0.0	40

Table 3.1: The values of the parameters which characterize the different numerical simulations of experiment *V05*, described in Wieland (34). m_δ is the coefficient of the corrective term of the bottom friction angle δ , represented by equation (3.6). Time offset represents the delay introduced in the numerical simulation. β_r is the inclination on the horizontal of the rotated coordinate system.

3. The two-dimensional model

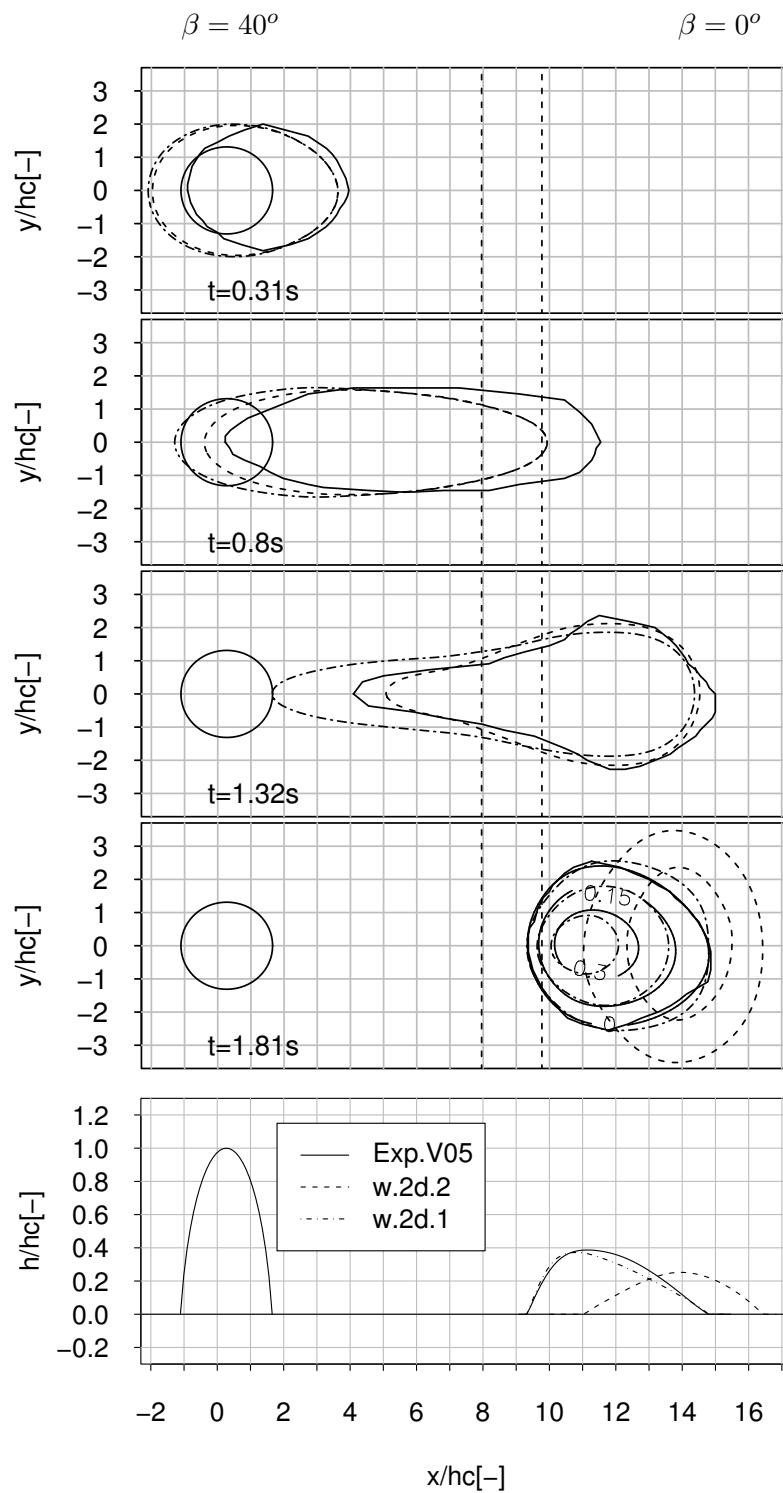


Figure 3.5: Comparison between experiment V05 performed by Wieland et al. (1999) and numerical simulations obtained by correcting the bottom friction angle δ through equation (3.6). The values of the applied numerical parameters are shown in Table 3.1. All the geometrical dimensions are non-dimensionalized by h_c , the initial depth of the mass. β is the inclination angle of the thalweg line on the horizontal.

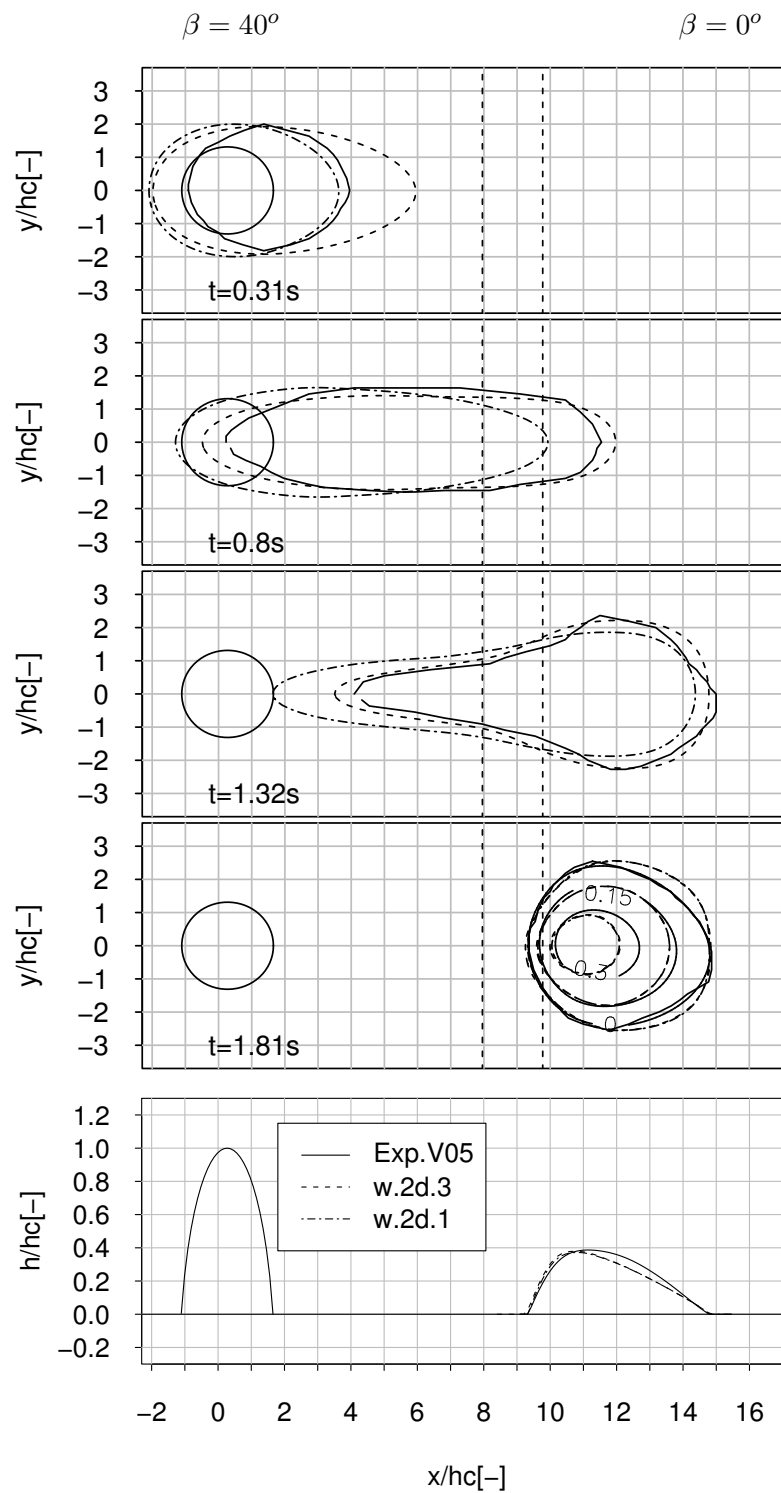


Figure 3.6: Comparison between experiment V05 performed by Wieland et al. (1999) and numerical simulations obtained by adding an offset of 0.2 s to the time. The values of the applied numerical parameters are shown in Table 3.1. All the geometrical dimensions are non-dimensionalized by h_c , the initial depth of the mass. β is the inclination angle of the thalweg line on the horizontal.

To evaluate these errors the original two-dimensional model has been developed, in order to give the opportunity of running the program in a rotated absolute coordinate system. Figure 3.7 shows the comparison between the simulation made with the horizontal coordinate system and the simulation made with the absolute coordinate system rotated by 40° about the y -axis, in order to better fit the sliding surface in the initiation zone.

The reproduction of the very initial instants is excellent. Then, in the simulation, the delay of the rear is not recovered while the fitting of the front noticeably improves. When the avalanche reaches the horizontal part of the chute, the quality of the numerical results gets suddenly worse.

Using a coordinate system inclined at 40° on the horizontal, the deviation of the direction identified by z from the normal to the bottom ζ , reduces considerably in the initiation zone: it vanishes along the thalweg of the chute and slightly increases as the cross distance from the thalweg increases. The problem is transferred to the run-out zone, where the directions ζ and z are inclined of 40° one with respect to the other.

It follows that, in the application to real cases, it is important to choose the orientation of the absolute coordinate system so that the reference surface xy best fits the topography.

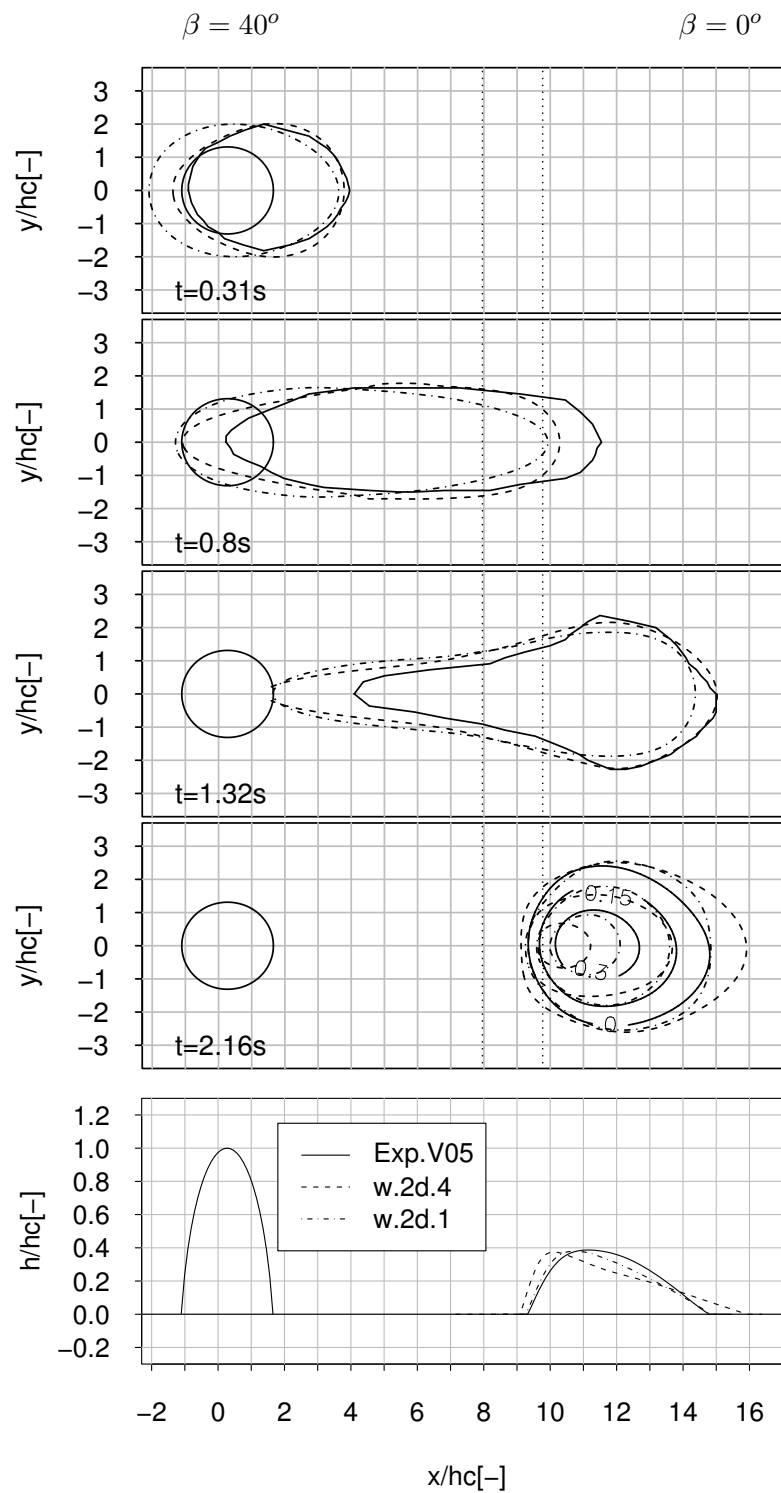


Figure 3.7: Comparison between experiment V05 performed by Wieland et al. (1999) and numerical simulations obtained applying the horizontal coordinate system and the coordinate system inclined at 40° . The values of the applied numerical parameters are shown in Table 3.1. All the geometrical dimensions are non-dimensionalized by h_c , the initial depth of the mass. β is the inclination angle of the thalweg line on the horizontal.

3.3 The definition of the secondary principal stress

Some experiments have been performed at the Hydraulic Laboratory of the University of Trento, in a double slope unconfined chute. The comparison with the simulations of the model shows that Hutter's approach for the definition of the secondary principal stress is not always effective.

3.3.1 Double slope unconfined chute

The model has been tested against experimental data collected at the Hydraulic Laboratory of the University of Trento.

The experimental apparatus consisted of a sliding surface, made up of two connected planes in forex with slopes of 27° and 0° (Figure 3.8).



Figure 3.8: Experimental apparatus at the Hydraulic Laboratory of the Department of Civil and Environmental Engineering of the University of Trento.

The granular material was synthetic zeolite, with almost uniform grain size distribution. Diameters ranged from 0.1 mm to 2 mm , with a mean value of 1 mm . The values of the internal friction angle ϕ and of the bed friction angle δ , measured by means of a shear box by D'Accordi (4), were $28^\circ \pm 0.75^\circ$ and $22^\circ \pm 0.75^\circ$, respectively. The values used in the simulations were $\phi = 28^\circ$ and $\delta = 22^\circ$.

In experiment *Exp. 2.0*, the mass of zeolite was released from a truncated conical shape holder, that was risen up normally to the bottom by a pneumatic piston. The conical holder was 20 cm high, with a basal radius of 21.8 cm and the lateral surface inclined at 50° on the basal plane. The initial position of the centre of the base was $x = -111.4$ cm and $y = -3$ cm.

The final deposit was automatically scanned by means of a laser distancemeter, mounted on a two-axial moving system (see Figure 3.9). Sensor moving and data acquisition are controlled by means of a LABVIEW program.

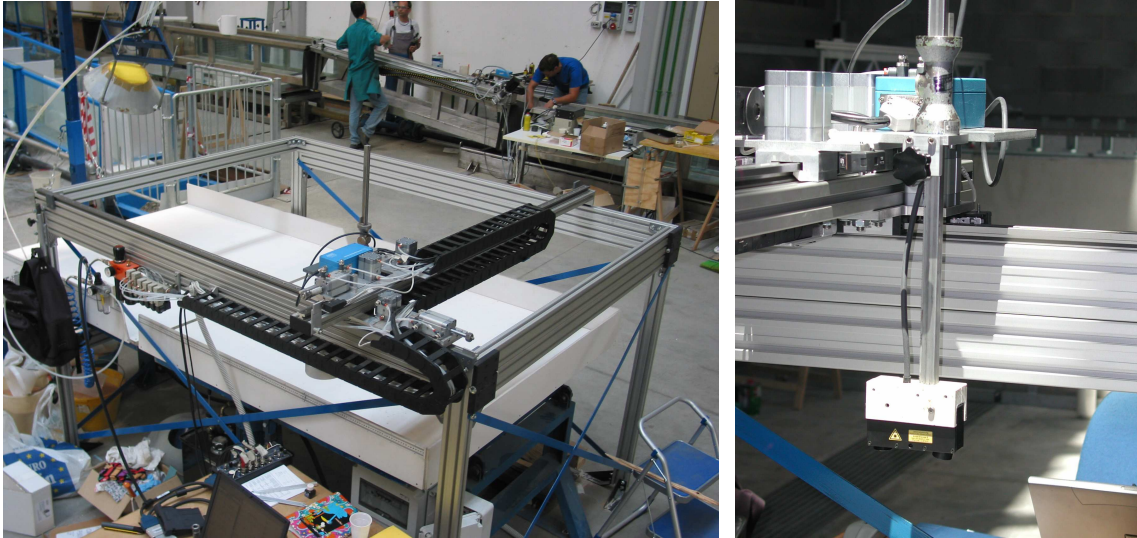


Figure 3.9: The two-axial pneumatic moving system, carrying a laser distance sensor, used to automatically map the final deposit of experiments performed on the double-slope unconfined chute at the Hydraulic Laboratory of the University of Trento.

In Figure 3.10 it is shown the comparison between the experimental data and the results of the numerical simulations obtained using different approaches in the definition of the secondary principal stress. Assuming $p^{(HH)}$ equal to the maximum or minimum principal stress according to the sign of $\partial U_H / \partial H$, as in equation (3.5), the geometry of the mass at rest in the numerical simulation results deeper and laterally less spread (simulation *DT.2d.1*). Imposing $p^{(HH)}$ always equal to the maximum principal stress p_1 , independently of the sign of the velocity gradient, the final deposit is better reproduced (simulation *DT.2d.2*).

A further campaign of experiments would be necessary in order to better understand this aspect of the rheology.

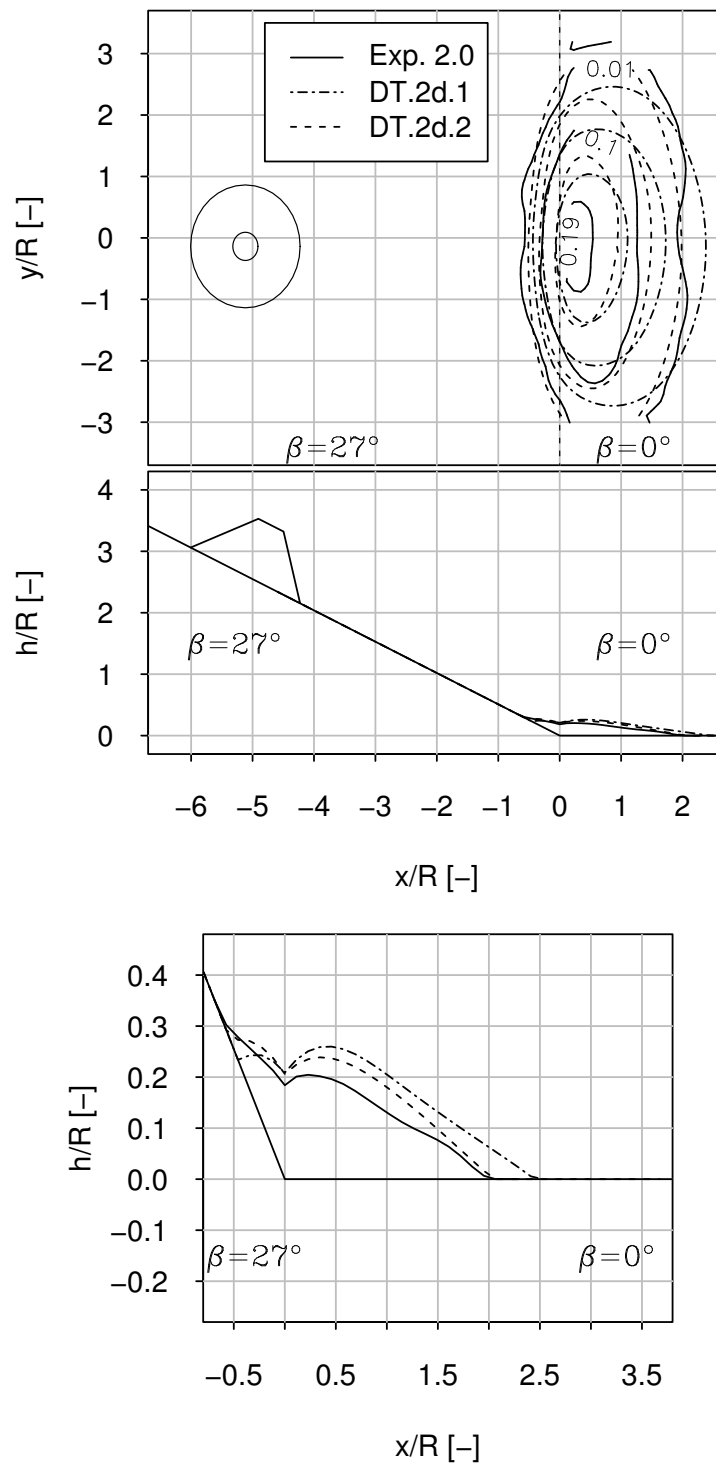


Figure 3.10: Comparison between experimental data, collected at the Hydraulic Laboratory of the University of Trento, and numerical simulations (plan, longitudinal section and amplified (factor 5) longitudinal section at $y/R = -0.023$). Simulation *DT.2d.1* is obtained applying Hutter's approach to the calculation of p_{HH} (equation (3.5)). In simulation *DT.2d.2* it is assumed $p_{HH} = p_1$. All geometrical dimensions are non-dimensionalized by R , the lower base radius of the truncated conical holder (Figure 3.8), equal to 21.8 cm.

3.4 The distortion of the mesh

One of the most critical deficiencies of the model, that precludes the application to complex topographies, is represented by the severe distortion of the mesh when strong transversal gradients of the velocity take place. For example, the model is unable to reproduce mass separations due to the interposing of obstacles along the path of the avalanche, as can be seen in Figure 3.11.

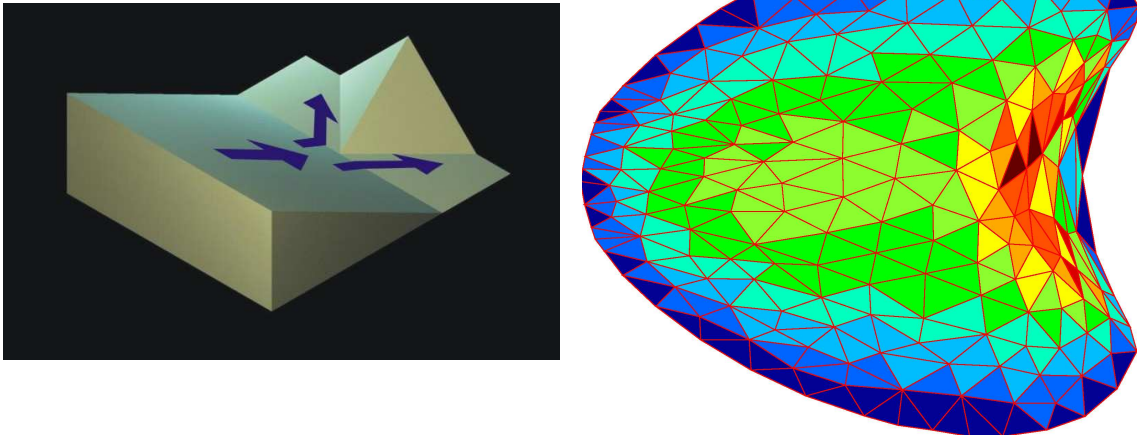


Figure 3.11: The distortion of the mesh when the mass collides with a dihedral obstacle. From Musner (22).

One possible solution could be to redefine the computational grid, before the distortion of the mesh causes the crash of the model. Remeshing algorithms are computationally expensive and yield a loss in accuracy, because of the errors introduced by remapping the field variables over the entire fluid domain. An alternative way to solve the problem could be the application of meshless methods, characterized by the absence of topological constraints between the nodes which represent the fluid domain. This property makes meshless methods suitable for the simulation of motion fields characterized by mass separations, strong deformations and discontinuities.

3.5 Final considerations

Our two-dimensional model reproduces sufficiently well experimental data, especially in presence of a weak lateral confinement and during the final phases of motion. Only two physical parameters, ϕ and δ , which are experimentally defined, have to be set.

In order to better predict the motion of the granular material during its entire evolution, it could be necessary to keep some terms of the balance equations, neglected in the hypothesis of “shallow water”. The application of a different plane reference surface, which, on the average, fits better the topography, allows to have z closer to ζ and reduces the errors due to the assumption of “plug flow” and linear pressure distribution along z , instead of along ζ .

However it is noticeable that, in natural events, the “shallow water” hypothesis is more likely to be violated in the run-out zone rather than in the initiation zone, because of the larger flow depth. For this same reason the deviation of z from ζ causes worse fittings where the mass stops. Furthermore, in application to real cases, attention is normally focused to the final stages of motion, to evaluate the impact forces on structures and to map the areas reached by the avalanche. Therefore it is reasonable to choose the orientation of the absolute coordinate system so that it better fits the run-out zone.

The model has to be further improved in order to apply it to real cases. The substantial exchanges of mass between the avalanche and the bottom during natural events can affect the dynamics of the motion by varying the momentum of the mass. Furthermore, the rear of the avalanche experiences, at its passage, a modified geometry of the bed and a different friction angle at the bottom. All these effects are not reproduced by the model. The error introduced neglecting these phenomena could be estimated through laboratory experiments on erodible bed.

In order to prevent the problems due to the distortion of the mesh, we focused our attention to meshless methods. The application of one of these methods, the Moving Least Square Particle Hydrodynamics, to the one-dimensional model, will be described in the next chapter.

4 The application of meshless numerical methods

4.1 What are meshless methods?

Meshless methods were first introduced by Lucy (18) and Gingold and Monaghan (14) in astrophysical and cosmological problems. Then they were modified, developed and applied to a wide range of problems, like high velocity impacts, compressible and incompressible fluid-dynamics, elastic–plastic flows, crack growth problems and to many other cases characterized by strong deformations, large discontinuities and mass separations.

The use of a mesh in the discretization of the spatial domain is the principal reason of the troubles shown by Finite Difference Methods (FDM) and Finite Element Methods (FEM) for such kind of problems. The generation of the mesh is not straightforward: the creation of the initial element connectivity is not entirely automated and if computational time is low in FEM, human intervention is necessary and time expensive. Furthermore, the distortion of the mesh requires a periodical re-meshing, through complex adaptive procedures, which have to “map” the field variables, with an additional computational cost and a decay of accuracy of the result.

Meshless methods represent the problem domain by a set of nodes scattered in the space. Nodes are not connected and no information on the geometrical relationships between the nodes is required. Furthermore, nodal density can be varied in the spatial domain and during the analysis, in order to increase the accuracy where large deformations and discontinuities take place. The field variables of the problem are interpolated or approximated through *shape functions*, which are relevant to the nodes and not to the elements as in FEM. For example the value of the generic variable q in the point \mathbf{x} is estimated by:

$$q^s(\mathbf{x}) = \sum_{i=1}^n q_i \phi_i(\mathbf{x}, s), \quad (4.1)$$

where q_i is the value of the variable at node i , $\phi_i = \phi_i(\mathbf{x}, s)$ is the shape function of node

i evaluated in \mathbf{x} and depending on the parameter s , n is the number of nodes included in a “small local domain” of \mathbf{x} . Only the nodes contained in this “small local domain” of \mathbf{x} , called *support domain*, contribute to the estimate of the field variable in \mathbf{x} . The derivatives of the field variable can be easily obtained from equation (4.1):

$$\nabla q^s(\mathbf{x}) = \sum_{i=1}^n q_i \nabla \phi_i(\mathbf{x}, s).$$

The support domain can have different shapes and dimensions, according to the density and arrangement of nodes. In particular the size of the support domain d_s is calculated as:

$$d_s = \alpha_s d_c, \tag{4.2}$$

where α_s is the dimensionless size of the support domain and d_c represents a characteristic length associated to the nodal spacing in the neighborhood of \mathbf{x} . d_c can be determined through the next simple steps. For one-dimensional cases, given the initial estimation of the support domain dimension D_s , and calculated n_{D_s} , the number of nodes covered by the domain of dimension D_s , d_c is given by:

$$d_c = \frac{D_s}{(n_{D_s} - 1)} \tag{4.3}$$

Finally, the dimension of the support domain d_s is calculated through equation (4.2), for a fixed dimensionless size of the support domain α_s . For two-dimensional and three-dimensional cases the average nodal spacing is given by:

$$d_c = \sqrt{\frac{A_s}{(n_{A_s} - 1)}} \quad \text{and} \quad d_c = \sqrt[3]{\frac{V_s}{(n_{V_s} - 1)}},$$

where A_s and V_s are estimations of first try of the area and the volume of the support domain.

Normally the contribution of each node to the construction of the approximation of the field variable in \mathbf{x} , will be weighted through a *weight function*.

In case of drastically heterogeneous distribution of nodes, using the support domain to identify the nodes involved in the construction of the shape functions can result in very poor approximations. In order to prevent this kind of problems, it was developed the concept of *influence domain*, defined as “the domain that a node exerts an influence upon” (17). The influence domain is associated to the node i and not to the point of interest

\mathbf{x} . According to the approach of the influence domain, all nodes which include in their influence domain the point of interest \mathbf{x} are used in the construction of the shape functions. The size of the influence domain d_i can be determined according to the nodal distribution, through a procedure similar to that seen for the support domain (see equation (4.2)).

The concepts of the support domain and of the influence domain are represented in Figure 4.1 and in Figure 4.2. The comparison of the two figures shows how differently they work in presence of unbalanced distributions of nodes. For example node 2, that belongs to an area with high nodal density, is included in the support domain of point \mathbf{x} , located in a low density area, whereas point \mathbf{x} is not comprehended in the influence domain of node 2.

Meshless methods apply to partial differential equations, written both in strong and weak form.

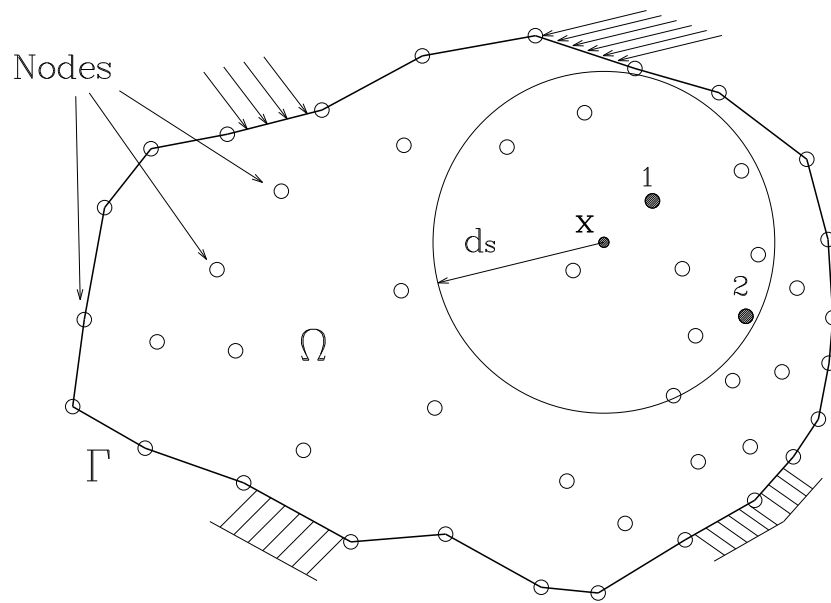


Figure 4.1: The definition of the support domain centered in the point of interest \mathbf{x} . Both the nodes 1 and 2 are included in the support domain of the point of interest.

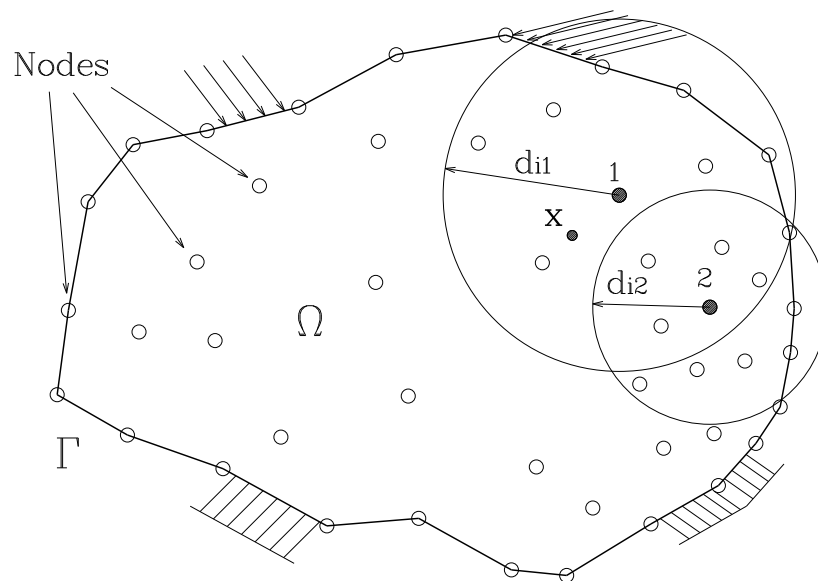


Figure 4.2: The definition of the influence domain for nodes 1 and 2. The point of interest is contained in the influence domain of node 1, but is excluded from the influence domain of node 2.

4.1.1 The properties of the shape functions

Setting the initial nodal distribution in meshless methods is more flexible than in FEM. Avoiding nodal alignments insures against the arising of singular matrices.

A compulsory condition that shape functions must respect is the *partition of unity*:

$$\sum_{i=1}^n \phi_i(\mathbf{x}, s) = 1,$$

which allows shape functions to reproduce any rigid motion of the domain. Another important property descends from this:

$$\sum_{i=1}^n \nabla \phi_i(\mathbf{x}, s) = \nabla \sum_{i=1}^n \phi_i(\mathbf{x}, s) = 0. \quad (4.4)$$

The *Kronecker delta function property* provides that:

$$\phi_i(\mathbf{x} = \mathbf{x}_j, s) = \begin{cases} 1 & i = j \\ 0 & i \neq j \end{cases} \quad \text{for } i, j = 1, 2, \dots, n.$$

It is not a necessary condition, but it simplifies the imposition of essential boundary conditions. When shape functions satisfy the Kronecker delta condition the evaluation of the field variables given by equation (4.1) is an interpolation, that is $q^s(\mathbf{x})$ passes through the nodal values. Differently, equation (4.1) is an approximation of the field variable $q(\mathbf{x})$.

The *consistency* requirement of the shape functions ensures the convergence of the applied meshless method, as nodal spacing goes to 0. The approximation is said to have *kth-order consistency* if it can exactly reproduce all the polynomial terms up to the *kth-order*. The order of *consistency* required for the convergence depends on the order of the partial differential equations and on the form they are expressed in (weak or strong form).

The approximant function has *compatibility* of order *k* if its derivatives are continuous up to *kth-order*. The *compatibility* affects the convergence and the accuracy of the solution.

The shape functions normally have compact support, that is the domain for field variables interpolation or approximation is small compared to the entire physical domain. Resulting system matrices have narrow bandwidth, with a reduction of the computational cost.

4.1.2 Smoothed Particle Hydrodynamics (SPH) shape functions

The integral representation of a generic function $q(\mathbf{x})$ is given by:

$$q(\mathbf{x}) = \int_{\Omega} q(\xi) \delta(\mathbf{x} - \xi) d\xi,$$

where $\delta(\mathbf{x})$ is the Dirac delta function:

$$\delta(\mathbf{x}) = \begin{cases} 1 & \mathbf{x} = \mathbf{0} \\ 0 & \mathbf{x} \neq \mathbf{0} \end{cases} .$$

The Dirac delta function $\delta(\mathbf{x})$ can be approximated through an appropriate function $W(\mathbf{x}, s)$, called *kernel* or *weight* or *smoothing function*. The integral representation of $q(\mathbf{x})$ is approximated by a finite integral form:

$$q^s(\mathbf{x}) = \int_{\Omega} q(\xi) W(\mathbf{x} - \xi, s) d\xi . \quad (4.5)$$

s is called *smoothing length* and controls the size of the compact support domain. The kernel function $W(\mathbf{x} - \xi, s)$ must satisfy two properties:

$$\int_{\Omega} W(\mathbf{x} - \xi, s) d\xi = 1 \quad (4.6)$$

and

$$\lim_{s \rightarrow 0} W(\mathbf{x} - \xi, s) = \delta(\mathbf{x} - \xi) .$$

From equation (4.6) it follows that:

$$\int_{\Omega} \nabla W(\mathbf{x} - \xi, s) d\xi = 0 \quad (4.7)$$

The integral of equation (4.5) is numerically discretized through the summation:

$$q^s(\mathbf{x}) = \sum_{i=1}^n q_i W(\mathbf{x} - \mathbf{x}_i, s) V_i ,$$

where V_i represents the volume associated to the generic node i and n is the number of nodes contained in the support domain of \mathbf{x} or which contain \mathbf{x} in their influence domain.

It follows the definition of the SPH shape function:

$$\phi_i(\mathbf{x}, s) = W(\mathbf{x} - \mathbf{x}_i, s) V_i .$$

The derivatives of the SPH approximation and, consequently, of the shape functions are:

$$\begin{aligned} \nabla q^s(\mathbf{x}) &= \sum_{i=1}^n q_i \nabla W(\mathbf{x} - \mathbf{x}_i, s) V_i , \\ \nabla \phi_i(\mathbf{x}, s) &= \nabla W(\mathbf{x} - \mathbf{x}_i, s) V_i . \end{aligned} \quad (4.8)$$

Equation (4.7) ensures that the derivative of the integral representation of 1 returns 0, but this is not true for its discretized version (4.8). It is for this reason that, in the generic point \mathbf{x} , the derivative of the function q is calculated as:

$$\begin{aligned}\nabla q^s(\mathbf{x}) &= \nabla \left(\sum_{i=1}^n q_i W(\mathbf{x} - \mathbf{x}_i, s) V_i \right) - q(\mathbf{x}) \nabla \left(\sum_{i=1}^n W(\mathbf{x} - \mathbf{x}_i, s) V_i \right) = \\ &= \sum_{i=1}^n (q_i - q(\mathbf{x})) \nabla W(\mathbf{x} - \mathbf{x}_i, s) V_i,\end{aligned}$$

Furthermore, it is easy to demonstrate that the integral SPH representation (4.5) has only 0th-order *consistency*. In order to have *consistency* of order 1 the first moment of the kernel function has to vanish, that is the kernel function must be symmetric about the origin. This condition is satisfied by interior points, but not by points near the boundary.

To improve the order of consistency of the SPH-approximation the kernel function has to be renormalized ((24) and (15)). Working with the discretized kernel approximation, we can correct the derivative representation by means of a second rank tensor $\mathbf{D}(\mathbf{x}, s)$, such that:

$$\begin{aligned}\nabla q^s(\mathbf{x}) &= \mathbf{D}(\mathbf{x}, s) \nabla \left(\sum_{i=1}^n q_i W(\mathbf{x} - \mathbf{x}_i, s) V_i \right) + \\ &\quad - q(\mathbf{x}) \mathbf{D}(\mathbf{x}, s) \nabla \left(\sum_{i=1}^n W(\mathbf{x} - \mathbf{x}_i, s) V_i \right) = \\ &= \sum_{i=1}^n (q_i - q(\mathbf{x})) \mathbf{D}(\mathbf{x}, s) \nabla W(\mathbf{x} - \mathbf{x}_i, s) V_i.\end{aligned}$$

\mathbf{D} is called re-normalization matrix and it can be demonstrated that, asking for ∇q^s to reproduce exactly any polynomial of order up to 1, $\mathbf{D}(\mathbf{x}, s) = \mathbf{E}(\mathbf{x}, s)^{-1}$, where:

$$E_{kl}(\mathbf{x}, s) = \sum_{i=1}^n (x_i^{(k)} - x^{(k)}) \frac{\partial W(\mathbf{x} - \mathbf{x}_i, s)}{\partial x^{(l)}}.$$

If the smoothing length s goes to 0, the *consistency* of the discretized SPH representation is ensured (see (33)).

4.1.3 Moving Least Square Particle Hydrodynamics (MLSPH) shape functions

The Moving Least Square Approximants (MLSA), introduced by Lancaster and Salkauskas (16), solve the problem of *consistency* in a different way. The approximation of the field variable q is obtained through a linear combination of a given set \mathbf{p} of m functions $p_j(\mathbf{x})$, with $j = 1, 2, \dots, m$:

$$q^s(\mathbf{x}) = \sum_{j=1}^m p_j(\mathbf{x}) a_j(\mathbf{x}, s) = \mathbf{p}(\mathbf{x})^T \cdot \mathbf{a}(\mathbf{x}, s) . \quad (4.9)$$

If \mathbf{p} is the base of polynomials of order up to k , the consistency is ensured up to order k .

The coefficients $a_j(\mathbf{x}, s)$ are evaluated by minimizing the function:

$$J(\mathbf{x}, s) = \sum_{i=1}^n \left(\mathbf{p}(\mathbf{x}_i)^T \cdot \mathbf{a}(\mathbf{x}, s) - q_i \right)^2 W(\mathbf{x} - \mathbf{x}_i, s) \quad (4.10)$$

n is the number of nodes contained in the support domain of \mathbf{x} (or containing \mathbf{x} in their influence domain). J in equation (4.10) represents the weighted summation of the residuals of the approximation of the field variable $q(\mathbf{x})$, through equation (4.9), at the known nodes \mathbf{x}_i , with \mathbf{a} frozen on \mathbf{x} . The role of the weight function is to give different importance to nodes at unequal distances from \mathbf{x} . Furthermore, thanks to the weight function, \mathbf{x} enters into the nodes' supports and leaves from them gradually, ensuring the compatibility of the approximation.

The vector of coefficients $\mathbf{a}(\mathbf{x}, s)$, calculated in order to minimize the sum J of weighted residuals, is given by:

$$\mathbf{a}(\mathbf{x}, s) = \mathbf{A}^{-1}(\mathbf{x}, s) \mathbf{B}(\mathbf{x}, s) \mathbf{q} , \quad (4.11)$$

where:

$$\begin{aligned} \mathbf{q}^T &= [q_1, q_2, \dots, q_n] , \\ \mathbf{A}(\mathbf{x}, s) &= \sum_{i=1}^n W(\mathbf{x} - \mathbf{x}_i, s) \mathbf{p}(\mathbf{x}_i) \mathbf{p}^T(\mathbf{x}_i) , \\ \mathbf{B}(\mathbf{x}, s) &= [\mathbf{B}_1, \mathbf{B}_2, \dots, \mathbf{B}_n] , \text{ with} \\ \mathbf{B}_i(\mathbf{x}, s) &= W(\mathbf{x} - \mathbf{x}_i, s) \mathbf{p}(\mathbf{x}_i) \end{aligned} \quad (4.12)$$

Substituting equation (4.11) into equation (4.9), one obtains:

$$q^s(\mathbf{x}) = \sum_{i=1}^n q_i \phi_i(\mathbf{x}, s), \text{ where}$$

$$\phi_i(\mathbf{x}, s) = \mathbf{p}(\mathbf{x})^T \mathbf{A}(\mathbf{x}, s)^{-1} \mathbf{B}_i(\mathbf{x}, s).$$

It can be demonstrated that the gradient of the MLS approximant is:

$$\nabla \phi_i(\mathbf{x}, s) = + \left[\nabla \mathbf{p}(\mathbf{x})^T \mathbf{A}^{-1} \mathbf{p}(\mathbf{x}_i) + \mathbf{p}(\mathbf{x})^T \mathbf{A}^{-1} \mathbf{A} \mathbf{A}^{-1} \mathbf{p}(\mathbf{x}_i) \right] W(\mathbf{x} - \mathbf{x}_i, s) + \mathbf{p}(\mathbf{x})^T \mathbf{A}^{-1} \mathbf{p}(\mathbf{x}_i) \nabla W(\mathbf{x} - \mathbf{x}_i, s),$$

where \mathbf{A} is $\mathbf{A}(\mathbf{x}, s)$.

A necessary condition for \mathbf{A} being invertible is that the number n of neighboring nodes is greater than the number m of functions of the base. But this is not sufficient. If nodes are aligned or are very close one to the other, \mathbf{A} can become singular. In order to avoid singularities, the dimension s of the support of nodes can be determined as a function of the local nodal density. Another solution could be to modify the maximum order of the polynomial of the base, according to the local density of nodes, but this means losing compatibility at the intersections between the influence domains of the nodes and reducing the consistency order.

4.2 The application of MLS approximants to the prediction of snow distribution

In the degree thesis by Sanfilippo (26), in order to test the efficiency of MLS approximants, they have been applied to the prediction of snow distribution in the Province of Trentino (Italy). Given the values of snow depth at several meteorologic stations located in Trentino, MLS approximants have been used to evaluate the snow depth in other points of interest. In particular, using the Digital Elevation Model of Trentino with resolution $200 \times 200 m$, maps of the distribution of snow have been realized and the volume of snow cover in all Trentino has been evaluated. What follows refers to the elaborations performed with the data collected on the 10th of January of 2001. The weather stations are shown in Figure 4.4 and their names, elevations above sea level and measured snow depths on January 10th 2001, are reported in Table 4.1. Different types of MLS approximants have been applied to estimate the snow distribution. Two indicators of the goodness of the approximation are represented by the mean and the standard deviation of the residuals of the estimations

from the known values at the snow stations. The computations are performed excluding the target point from the set of known nodes. In Table 4.2 the different types of MLS approximants are compared.

Because of the strong variability of the distribution of weather stations, the size s of the node supports should be chosen very large in order to gain matrix \mathbf{A} invertibility everywhere in the spatial domain. An alternative solution is to apply a MLS algorithm with a variable size s of the node support. In particular the value of s at each node is set in order to have, at each point of interest \mathbf{x} , a sufficient number of neighboring nodes for matrix \mathbf{A} (4.12) invertibility.

The used weight function was a cubic spline:

$$W(\mathbf{x} - \mathbf{x}_i, s) = \begin{cases} \frac{2}{3} - 4r_i^2 + 4r_i^3 & r_i \leq \frac{1}{2} \\ \frac{4}{3} - 4r_i + 4r_i^2 - \frac{4}{3}r_i^3 & \frac{1}{2} < r_i \leq 1 \\ 0 & 1 < r_i \end{cases},$$

with:

$$r_i = \frac{|\mathbf{x} - \mathbf{x}_i|}{s}.$$

The calculations were first made with a linear base:

$$\mathbf{p}^T(\mathbf{x}) = [1, x, y, z].$$

Figure 4.5 shows the approximated snow distribution obtained by choosing the size of the influence domain of each node in order to have at least 4 contiguous nodes for each point of interest. In Table 4.2 it can be noticed that incrementing the number of neighboring nodes, the approximation gets poorer. The reason is that the approximation loses its local character, because the influence of far nodes increases.

Figure 4.6 shows the results obtained with the quadratic base:

$$\mathbf{p}^T(\mathbf{x}) = [1, x, y, z, x^2, y^2, z^2, xy, xz, yz],$$

where s at each node is selected to have at least 11 neighboring nodes for each calculation point. The mean deviation is smaller than in linear cases ($0.17m$), but an anomalous growth of snow depth arises along the valley floor. This can be justified by the absence of snow depth measures at low altitudes. As shown in Figure 4.3, the quadratic term z^2

is the responsible for the non-monotone trend of the approximation. Adding 5 fictitious stations, with snow depth equal to 0 along the valley floors, the approximation improves. Using fictitious stations the mean deviation goes to $0.15 m$, as reported in Table 4.2. It is the best result, but anomalous trends are still recognizable at the eastern border of Trentino. The deficiency of this approach is that the choice of the position of the fictitious stations can be hardly automated.

Spurious trends can be removed also using a base mildly non-linear along z , without the term in z^2 , such as:

$$\mathbf{p}^T(\mathbf{x}) = [1, x, y, z, x^2, y^2, xy, xz, yz] .$$

The result is shown in Figure 4.8. The mean deviation is $0.19 m$, greater than the value obtained with the fictitious stations, but the algorithm does not requires external interventions.

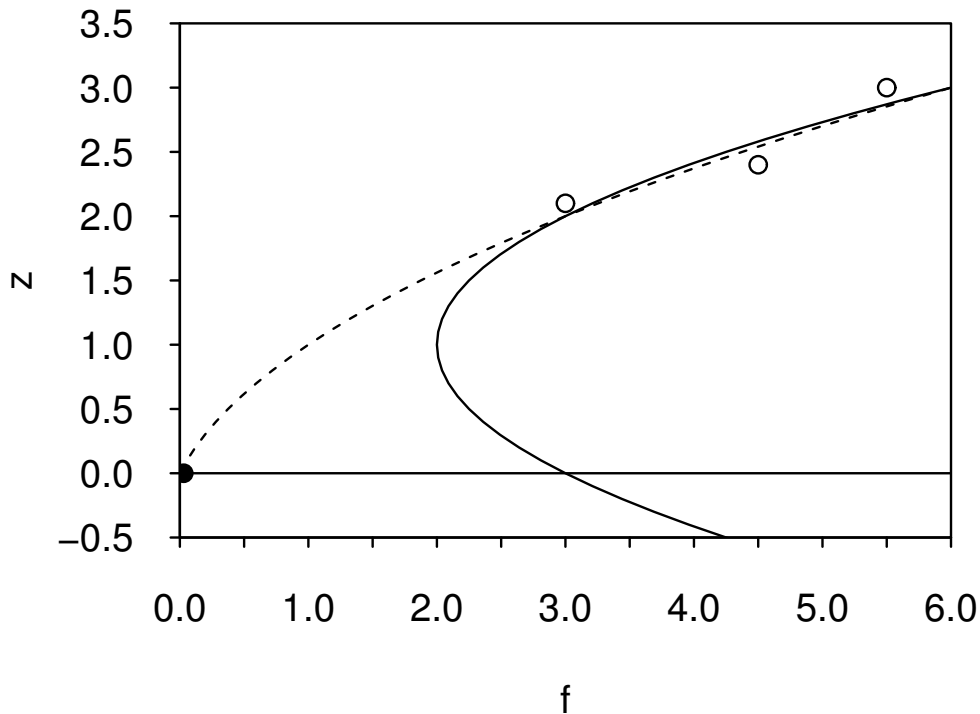


Figure 4.3: The incorrect parabolic extrapolation at low values of z (continuous line), when known nodes (empty circles) are absent in that region. Adding the fictitious node represented by the filled circle, the approximation retains a monotone trend in the whole region of interest (dashed line).

Another way to ensure matrix \mathbf{A} invertibility is to keep s constant, reducing the order of the base when the number of neighboring nodes is less than the number of base functions.

The approximants lose the *consistency* property, as can be observed in Figure 4.9. The discontinuities are localized where strong heterogeneities in snow stations distribution are concentrated. Incrementing s the discontinuities disappear, the mean deviation reduces, as shown in Table 4.2, but the local character of the approximation is lost and the approximant converges to the quadratic one.

The comparison of computed volumes in Table 4.2 shows that the most reliable estimates may have a mistake of over 100%. The volumes evaluated by the uncorrected quadratic MLS approximant and by the variable base MLS approximant, with $s = 17000 m$, are unlikely.

The MLS approximants can be applied to the estimation of any spatial function, known in a limited set of arbitrarily distributed nodes. For example, in the field of avalanche studies, the MLS approximant can be used in the determination of the spatial distribution of snow in the avalanche catchment, given the values of snow depth measured by means of half-meter graduated poles.

Id	Name	Elevation [m s.l.]	snow depth [m]
1PEI	Tarlenta	2010	1.40
2RAB	Rabbi	1280	0.09
3PIN	Pinzolo	1530	0.20
4SMC	S.Martino di C.	1460	0.21
5PSV	S.Valentino Pass	1330	0.00
6BON	Bondone	1445	0.20
7PVA	Valles Pass	2040	1.30
8PAN	Paneveggio	1535	0.14
9PTA	Panarotta	1775	0.56
10PM	Pampeago	1775	0.56
11AN	Andalo	1008	0.15
12FO	Sommo Pass	1360	0.10
13PR	Predazzo	1655	0.25
14PO	Pozza di Fassa	1380	0.11
15TR	Tremalzo	1520	0.24
16PT	Brocon Pass	1560	0.28
17CA	Caoria	925	0.13
18SB	Canal S.Bovo	1240	0.10
19PF	Vallarsa	1175	0.10
20BA	Malga Baessa	1260	0.20
21MB	Malga Bissina	1750	1.25
22CI	Ciampac	2160	1.22
23MC	Campiglio	1650	1.85

continue

Id	Name	Altitude [m a.m.s.l.]	snow depth [m]
24NO	Noana Valley	1025	0.10
25TO	Tonale Pass	1880	1.28
26SP	S.Pellegrino Pass	1980	0.91
27CM	Ciampedie	1975	0.88
28RM	Rumo	1090	0.06
30PN	Presena	2730	3.10
31RO	Rolle Pass	2000	1.23

Table 4.1: The list of snow and meteorologic stations in Trentino, used for the elaborations. For each station the identifier used in Figure 4.4, the name, the elevation above mean sea level, the measured snow depth on the 10th of January of 2001 are reported.

MLS approximant	Standard deviation [m]	Mean deviation [m]	Volume [10 ⁹ m ³]
Linear, 4 neighbors	0.28	0.18	2.661
Linear, 5 neighbors	0.28	0.20	2.567
Linear, 11 neighbors	0.30	0.22	2.341
Quadratic, 11 neighbors	0.28	0.17	4.302
Quadratic with fictitious stations, 11 neighbors	0.28	0.15	3.989
Quadratic along xy , mildly non-linear along z , 11 neighbors	0.28	0.19	2.935
Variable base order, $s = 17000 m$	0.39	0.21	6.412
Variable base order, $s = 45000 m$	0.32	0.18	3.916

Table 4.2: The standard and the mean deviation of the residuals and the computed volume for different types of MLS approximants.

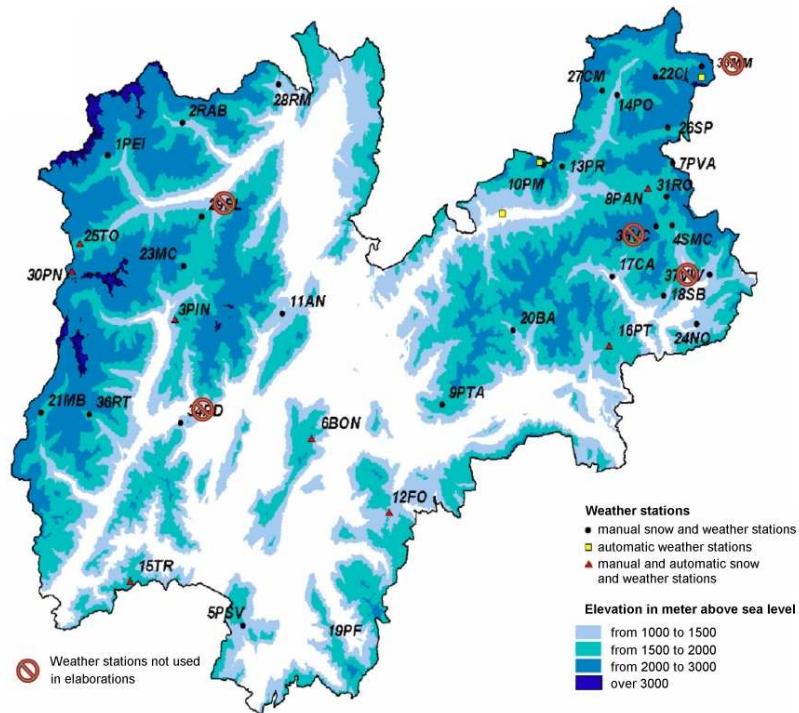


Figure 4.4: Digital Elevation Model of the Province of Trentino (Italy), with the snow and meteorologic stations used for the estimation of the snow distribution. Identifiers of stations are indicated in Table 4.1. The stations marked with the symbol indicated in the legend are excluded from computations, because they have no snow depth measure on January 10th 2004.

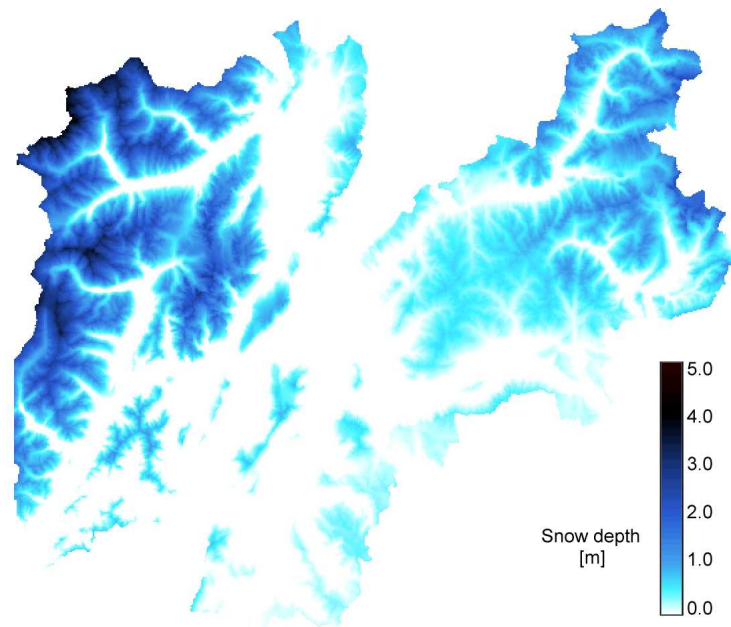


Figure 4.5: The snow distribution evaluated by MLS approximants, using a linear polynomial base and varying s up to have at least 4 neighboring nodes for each calculation point.

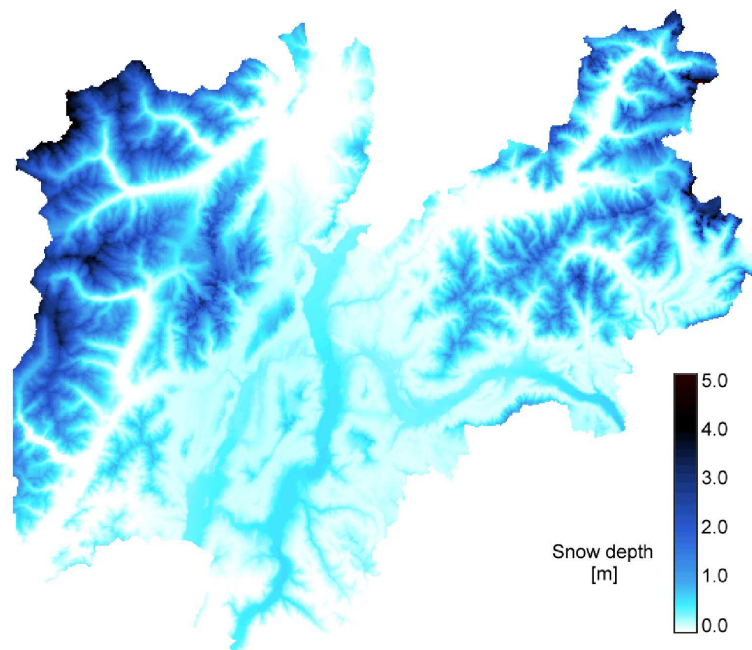


Figure 4.6: The snow distribution evaluated by MLS approximants, using a quadratic polynomial base and varying s up to have at least 11 neighboring nodes for each calculation point.

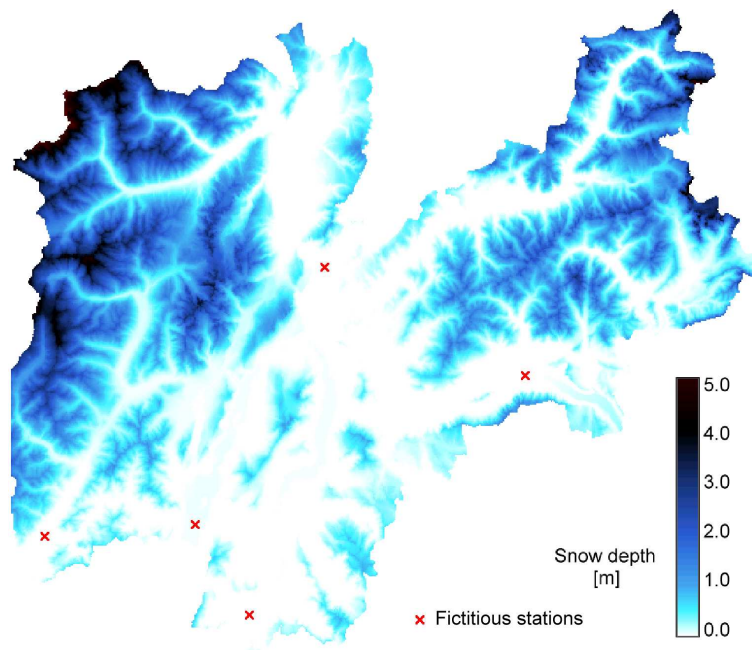


Figure 4.7: The snow distribution evaluated by MLS approximants, using a quadratic polynomial base and varying s up to have at least 11 neighboring nodes for each calculation point. 5 fictitious stations are indicated on the map through red crosses. They have been introduced in order to correct the increase of snow depth at low altitudes due to the quadratic trend in absence of known values of snow depth along the valley floors. The snow depth assigned to these fictitious nodes is 0.

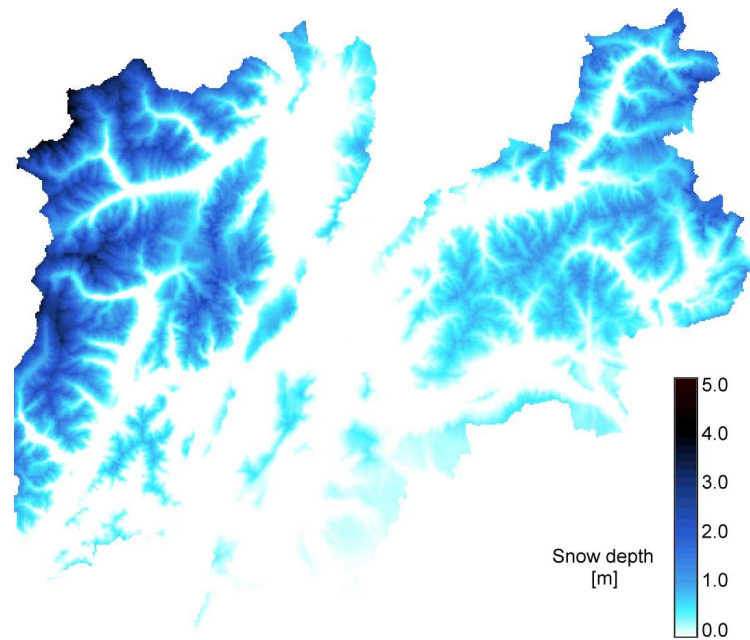


Figure 4.8: The snow distribution evaluated by MLS approximants, using a base mildly non-linear, varying s to have at least 11 neighboring nodes for each calculation point.

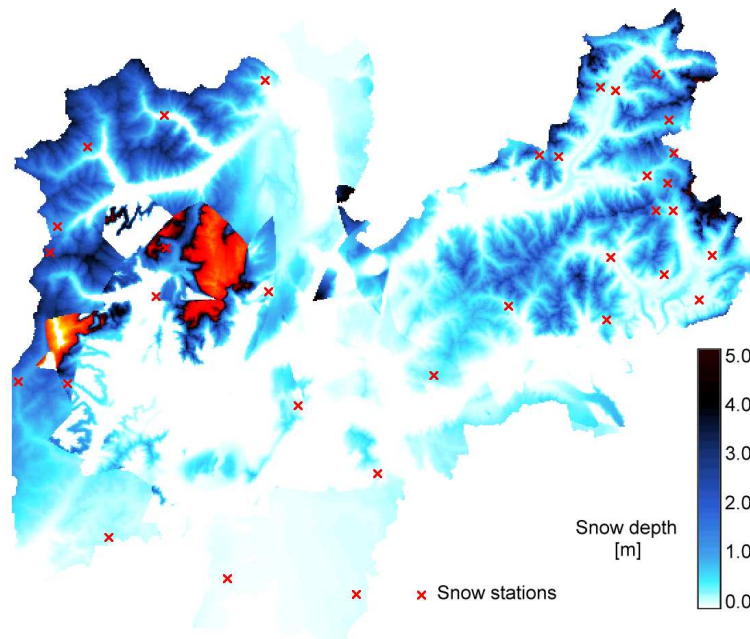


Figure 4.9: The snow distribution evaluated by MLS approximants, with s constant ($= 17000\text{ m}$), using a variable base order. The position of the snow stations is indicated through red crosses.

4.3 The MLSPH equations

The typical hydrodynamic equations of motion can be written in vectorial form as:

$$\rho \frac{d\mathbf{y}}{dt} = \mathbf{f} + \nabla \cdot \mathbf{F}(\mathbf{y}) , \quad (4.13)$$

where \mathbf{y} is the vector of conserved quantities, \mathbf{f} is the source/sink term and \mathbf{F} is the vector of fluxes. We can define a set of base functions $\{\phi_i\}_{i=1}^n$ for a n -dimensional subspace of a function space of which the components of \mathbf{y} are members. As in the Galerkin method, the equations of motion can be re-written in weak form by multiplying them by an arbitrary base function ϕ_i and integrating over the spatial domain Ω :

$$\int_{\Omega} \phi_i \rho \frac{d\mathbf{y}}{dt} d\mathbf{x} = \int_{\Omega} \phi_i (\mathbf{f} + \nabla \cdot \mathbf{F}) d\mathbf{x} . \quad (4.14)$$

In the MLPSH scheme proposed by Dilts ((7), (8)) ϕ_i are the MLS shape functions associated to the nodes, located in \mathbf{x}_i (with $i = 1, \dots, n$), through which the continuum is represented, that is:

$$\begin{aligned} \mathbf{y}^s(\mathbf{x}) &\approx \sum_{i=1}^n \phi_i(\mathbf{x}, s) \mathbf{y}_i , \quad \text{where} \\ \mathbf{y}_i &= \mathbf{y}(\mathbf{x}_i) . \end{aligned} \quad (4.15)$$

The flux term in the second member of equation (4.14) is usually integrated by parts. Using the Reynolds transport theorem:

$$\int_{\Omega} \phi_i \rho \frac{d\mathbf{y}}{dt} d\mathbf{x} = \int_{\Omega} \phi_i \mathbf{f} d\mathbf{x} + \int_{\Omega} \nabla \phi_i \cdot \mathbf{F} d\mathbf{x} + \int_{\partial\Omega} \phi_i \mathbf{F} \mathbf{n} dA , \quad (4.16)$$

where $\partial\Omega$ is the boundary of Ω , dA is an infinitesimal element of $\partial\Omega$ and \mathbf{n} is the outwards normal to dA .

The Galerkin method provides that \mathbf{y} will be expanded according to equation (4.15) and substituted into equation (4.16). The flux term \mathbf{F} is usually non linear and the resulting integral would become difficult to evaluate. Instead of \mathbf{y} , \mathbf{F} could be represented by means of the base functions:

$$\mathbf{F}^s(\mathbf{x}) = \sum_{i=1}^n \phi_i(\mathbf{x}, s) \mathbf{F}_i ,$$

with $\mathbf{F}_i = \mathbf{F}(\mathbf{y}_i)$.

The next step is to define a quadrature rule to evaluate the integrals. Given a generic function $g = g(\mathbf{x})$, defined on Ω , the mean value theorem states that:

$$\exists \xi \in \Omega \quad \text{such that} \quad \int_{\Omega} \phi_i g d\mathbf{x} = \left(\int_{\Omega} \phi_i d\mathbf{x} \right) g(\xi) .$$

A good approximation of the integral could be:

$$\int_{\Omega} \phi_i g d\mathbf{x} \cong V_i g_i ,$$

being:

$$\begin{aligned} V_i &= \int_{\Omega} \phi_i d\mathbf{x} , \\ g_i &= g(\mathbf{x}_i) , \end{aligned} \tag{4.17}$$

This is called the one point quadrature rule. V_i can be interpreted as the numerical volume associated to particle i . Applying the one point quadrature to the left member of equation (4.14) and to the sink/source term and expanding the flux term, one obtains the so-called collocation method:

$$\rho_i V_i \frac{d\mathbf{y}_i}{dt} = f_i V_i + \sum_{j=1}^n \mathbf{F}_j B_{ij} , \tag{4.18}$$

where:

$$B_{ij} = \int_{\Omega} \phi_i \nabla \phi_j d\mathbf{x} .$$

Equation (4.18) does not ensure local conservation, because it does not satisfy the flux balance properties, that is fluxes between particles are not equal and opposite. Infact the term of fluxes is not antisymmetric with respect to the particle index. Furthermore, it can be demonstrated (see (8)) that, applying the approximate quadrature, it does not guarantee the global conservation.

Applying the one point quadrature to equation (4.16), the result is:

$$\rho_i V_i \frac{d\mathbf{y}_i}{dt} = f_i V_i + \sum_{j=1}^n \mathbf{F}_j (C_{ij} - B_{ji}) , \tag{4.19}$$

where:

$$C_{ij} = \int_{\partial\Omega} \phi_i \phi_j \mathbf{n} dA .$$

This can be considered a complete Galerkin method. It is globally conservative, but not locally conservative, for the same reason seen for equation (4.18).

Applying the integration by parts, it is easy to demonstrate that:

$$B_{ij} = \int_{\Omega} \phi_i \nabla \phi_j d\mathbf{x} = \int_{\partial\Omega} \phi_i \phi_j \mathbf{n} dA - \int_{\Omega} \nabla \phi_i \phi_j d\mathbf{x} = C_{ij} - B_{ji}. \quad (4.20)$$

C_{ij} is different from 0 only when both nodes i and j intersect the boundary, that is, defining the set of boundary nodes:

$$\mathcal{B} = \{i : \text{Supp}(\phi_i) \cap \partial\Omega \neq \emptyset\},$$

with $\text{Supp}(\phi_i)$ the support of the base function ϕ_i , it results:

$$B_{ij} + B_{ji} = \begin{cases} C_{ij} & \text{if } i, j \in \mathcal{B} \\ 0 & \text{otherwise} \end{cases}.$$

From equation (4.4) and equation (4.20), it follows that:

$$\begin{aligned} 0 &= \sum_{j=1}^n B_{ij} = \sum_{j=1}^n \int_{\Omega} \phi_i \nabla \phi_j d\mathbf{x} = \int_{\Omega} \phi_i \sum_{j=1}^n \nabla \phi_j d\mathbf{x} \Rightarrow \\ \Rightarrow 0 &= \sum_{j=1}^n C_{ij} - B_{ij}. \end{aligned}$$

Dilts (8) suggests to add (4.18) and F_i times the summation $\sum_{j=1}^n B_{ij}$, with B_{ij} rewritten according to the equivalence (4.20):

$$\rho_i V_i \frac{dy_i}{dt} = f_i V_i + \sum_{j=1}^n \frac{1}{2} (\mathbf{F}_j + \mathbf{F}_i) (C_{ij} + B_{ij} - B_{ji}), \quad (4.21)$$

The resulting method is globally conservative and satisfies the flux balance principle, being the integrated flux antisymmetric with respect to particle index. The next step is to define a volume quadrature rule $Q(\cdot)$ and a surface quadrature rule $\partial Q(\cdot)$ for the terms B_{ij} and C_{ij} . A one point quadrature scheme can be used to estimate B_{ij} :

$$B_{ij} \approx V_i \nabla \phi_j(\mathbf{x}_i).$$

The surface quadrature rule $\partial Q(\cdot)$ must satisfy the equivalence (4.20), such that:

$$Q(B_{ij}) = \partial Q(C_{ij}) - Q(B_{ji}), \quad \text{when } i, j \in \mathcal{B}. \quad (4.22)$$

Dilts (8) argues that, even using the one–point quadrature rule and a compatible surface rule according to (4.22), the schemes (4.19) and (4.21) are not necessarily consistent. Infact, if the flux term \mathbf{F} is a polynomial of order not higher than the base functions, the approximation of its divergence in the second member of (4.19) and (4.21) can be not a function of the gradient of a polynomial. Finally it is not ensured that the surface quadrature rule $\partial Q(\cdot)$ satisfies the condition:

$$\sum_{i=1}^n \mathbf{n}_i = \int_{\partial\Omega} \mathbf{n} dA = \int_{\Omega} \nabla(1) d\mathbf{x} = 0.$$

All these deficiencies can compromise the accuracy of the numerical scheme.

4.4 A MLSPH one-dimensional model with constant width

In collaboration with Musner (22), the MLSPH algorithm has been applied to a one-dimensional model with constant width, developed at the Department of Civil and Environmental Engineering of the University of Trento, and called *mlsph1d*.

4.4.1 The original equation of motion

The mass and momentum conservation laws for an incompressible continuum, written in vectorial form, are:

$$\begin{aligned}\nabla \cdot \mathbf{u} &= 0, \\ \frac{d\mathbf{u}}{dt} &= \mathbf{g} + \frac{1}{\rho} \nabla \cdot \mathbf{P},\end{aligned}$$

where ρ is density, \mathbf{u} is the velocity vector, \mathbf{g} is the gravity acceleration and \mathbf{P} is the stress tensor. In the (ξ, ζ) -curvilinear coordinate system, lying on a vertical plane, with ξ orientated along the slope and ζ normally to it, the free surface is represented by:

$$\Phi_h(\mathbf{x}, t) = \zeta - h(\xi, t) = 0.$$

The kinematic and dynamic boundary conditions are give by:

$$\begin{aligned}\frac{\partial \Phi_h}{\partial t} + \mathbf{u} \cdot \nabla \Phi_h &= 0, \\ \mathbf{P}_h \cdot \mathbf{n}_h &= 0\end{aligned}$$

being $\mathbf{n}_h = \nabla \Phi_h / |\nabla \Phi_h|$ the unit vector normal to the free surface, and \mathbf{P}_h the stress tensor at $\zeta = h(\xi, t)$.

At the bottom ($\zeta = 0$), the kinematic boundary condition is:

$$\mathbf{u} \cdot \mathbf{n}_b = 0,$$

with $\mathbf{n}_b = (0, -1)$ the unit vector normal to the sliding surface. A Coulomb-type friction law is used to represent the interaction of the granular flow with the bottom:

$$\mathbf{P}_b \mathbf{n}_b - \mathbf{n}_b (\mathbf{n}_b \cdot \mathbf{P}_b \mathbf{n}_b) = + (\mathbf{u}_b / |\mathbf{u}_b|) \tan \delta (\mathbf{n}_b \cdot \mathbf{P}_b \mathbf{n}_b),$$

where \mathbf{P}_b is the stress tensor at the bottom and δ is the bottom friction angle. The equations of the model are non-dimensionalized by means of the following scale quantities:

- L_s : the length scale along ξ ;

- H_s : the depth flow scale;
- R_s : the curvature radius scale;
- $U_{\xi s}$: the velocity scale along ξ ;
- $U_{\zeta s}$: the velocity scale along ζ ;
- T_s : the time scale;
- P_s : the pressure scale;
- ρ_s : the density scale.

Having defined the ratios $\varepsilon = H_s/L_s$ and $\lambda = L_s/R_s$, the following hypothesis are introduced:

- $\varepsilon \ll 1$, i.e. the “shallow water” assumption;
- $\varepsilon \lambda \ll 1 \Rightarrow H_s \ll R_s$, that is small bottom curvature;
- $U_s^2/L_s \approx g \approx P_s/\rho_s H_s$, that is inertial, gravitational and pressure forces are comparable;
- constancy of the velocity vector along the normal to the bottom direction;

Furthermore, from obvious kinematic considerations, $T_s = L_s/U_{\xi s}$ and from the continuity equation it follows that $U_{\zeta s} = \varepsilon U_{\xi s}$.

According to these hypothesis the mass and momentum balances are simplified and then integrated over ζ . The continuity equation becomes:

$$\frac{1}{h} \frac{dh}{dt} = -\frac{\partial U_{\xi}}{\partial \xi}, \quad (4.23)$$

being:

$$U_{\xi} = \frac{1}{h} \int_0^h u_{\xi} d\zeta.$$

It can be expressed in a form which will turn out useful later:

$$h \frac{d(1/h)}{dt} = +\frac{\partial U_{\xi}}{\partial \xi}. \quad (4.24)$$

The momentum balance along ζ yields the hydrostatic pressure distribution:

$$p_{\zeta\zeta}(\zeta) = -\rho (g \cos \beta + \chi U_{\xi}^2) (h - \zeta),$$

where β is the slope angle and χ is the curvature of the bottom. The other components of the stress tensor are derived by applying the Hutter and Savage rheology (28) and are the same found in §2.2.4, relevant to the plane ΞH . At the bottom it results that:

$$\begin{aligned} (p_{\xi\xi})_b &= k_{a/p} (p_{\zeta\zeta})_b, \\ (p_{\zeta\xi})_b &= (p_{\xi\zeta})_b = +\text{sgn}(u_\xi) \tan \delta (p_{\zeta\zeta})_b, \end{aligned} \quad (4.25)$$

where $k_{a/p}$ is defined according to the sign of $\partial u_\xi / \partial \xi$, as in equation (2.10) (see Figure 2.6). The linear dependence of the components of the stress tensor on $p_{\zeta\zeta}$, expressed by equation (4.25) at the bottom, is assumed to hold over the entire depth of the flowing mass. Simplifying the momentum balance along ξ , according to the hypothesis previously introduced, and integrating over ζ , one obtains:

$$h \frac{dU_\xi}{dt} = g h \sin \beta + \frac{\partial}{\partial \xi} \left(\frac{P_{\xi\xi} h}{\rho} \right) + \frac{2 P_{\zeta\xi}}{\rho}, \quad (4.26)$$

being:

$$\begin{aligned} P_{\xi\xi} &= \frac{1}{h} \int_0^h p_{\xi\xi} d\zeta = k_{a/p} \rho \frac{h}{2} (g \cos \beta + \chi U_\xi^2) \\ P_{\zeta\xi} &= +\rho \frac{h}{2} \text{sgn}(U_\xi) \tan \delta (g \cos \beta + \chi U_\xi^2). \end{aligned}$$

In order to highlight pressure terms and sink and source terms, equation (4.26) can be re-written as:

$$h \frac{dU_\xi}{dt} = \mathcal{G} - \mathcal{R} - \nabla \mathcal{P}, \quad (4.27)$$

where $\mathcal{G} = g h \sin \beta$ represents the driving gravitational force, $\mathcal{R} = -2 P_{\zeta\xi} / \rho$ is the resistance term, and $\mathcal{P} = -P_{\xi\xi} h / \rho$ is the stress flux term.

4.4.2 The one-dimensional MLSPH equation of motion

In the one-dimensional case the numerical particle volume defined by equation (4.17), becomes a numerical particle length:

$$l_i = \int_{L_{supp}} \phi_i d\xi, \quad (4.28)$$

where:

$$L_{supp} = \bigcup_{i=1}^n s_i,$$

is the one-dimensional spatial domain, constituted by the union of the nodal support domains s_i . The continuity equation (4.24) and the momentum balance along ξ (4.27) correspond to equation (4.13) with ρ substituted by h and with:

$$\mathbf{u} = \begin{bmatrix} 1/h \\ U_\xi \end{bmatrix}, \quad \mathbf{f} = \begin{bmatrix} 0 \\ \mathcal{G} - \mathcal{R} \end{bmatrix}, \quad \mathbf{F} = \begin{bmatrix} U_\xi \\ -\mathcal{P} \end{bmatrix}.$$

Substituting into equation (4.21), one obtains:

$$\begin{aligned} h_i l_i \frac{d(1/h_i)}{dt} &= \frac{1}{2} \sum_{j=1}^n (U_{\xi j} + U_{\xi i}) (C_{ij} + B_{ij} - B_{ji}), \\ h_i l_i \frac{dU_\xi}{dt} &= (\mathcal{G}_i - \mathcal{R}_i) l_i - \frac{1}{2} \sum_{j=1}^n (\mathcal{P}_j + \mathcal{P}_i) (C_{ij} + B_{ij} - B_{ji}). \end{aligned} \quad (4.29)$$

Equation (4.29) does not ensure the Galilean invariance: even if the velocity field is constant, h disturbances could arise due to the numerical approximation. This deficiency can be removed if the mean velocity $(U_{\xi j} + U_{\xi i})/2$ is substituted by the difference $U_{\xi j} - U_{\xi i}$ in the equation of continuity. This is a common practice in SPH models. Another problem is that l_i is difficult to calculate through equation (4.28). A possible solution is to treat l_i as an unknown, by introducing a numerical particle area A_i , assumed constant, defined as:

$$A_i = l_i h_i.$$

The continuity equation becomes:

$$\frac{d(A_i/h_i)}{dt} = \frac{dl_i}{dt} = \frac{1}{2} \sum_{j=1}^n (U_{\xi j} - U_{\xi i}) (C_{ij} + B_{ij} - B_{ji}). \quad (4.30)$$

In order to attenuate numerical instabilities, the momentum equation is corrected with an artificial viscosity Π_{ij} , in the form proposed by Monaghan (see (20)) for SPH methods:

$$A_i \frac{dU_\xi}{dt} = (\mathcal{G}_i - \mathcal{R}_i) l_i - \frac{1}{2} \sum_{j=1}^n (\mathcal{P}_j + \mathcal{P}_i + \Pi_{ij}) (C_{ij} + B_{ij} - B_{ji}), \quad (4.31)$$

with:

$$\Pi_{ij} = \begin{cases} \bar{h}_{ij} (-\alpha_v \bar{c}_{ij} \mu_{ij} + \beta_v \mu_{ij}^2) & \text{if } \nabla U_\xi < 0, \quad \text{that is } U_{\xi ij} \cdot \xi_{ij} < 0 \\ 0 & \text{if } \nabla U_\xi \geq 0, \quad \text{that is } U_{\xi ij} \cdot \xi_{ij} \geq 0 \end{cases}, \quad (4.32)$$

where:

$$\mu_{ij} = \frac{\bar{s}_{ij} U_{\xi ij} \xi_{ij}}{\xi_{ij}^2 + \gamma_v \bar{s}_{ij}^2},$$

being for the generic quantity f :

$$\bar{f}_{ij} = \frac{f_i + f_j}{2}, \quad f_{ij} = f_i - f_j.$$

In equation (4.32) c_i represents the celerity of the hyperbolic differential system at the generic node i . It can be calculated writing the continuity equation (4.23) and the integrated momentum equation along ξ (4.26) in a moving coordinate system $(\hat{\xi}, \hat{t})$, with:

$$\begin{aligned} \hat{\xi} &= \xi - \int_0^t U_{\xi} dt, \\ \hat{t} &= t. \end{aligned}$$

If U_{ξ} is assumed to be constant with respect to ξ and t , it can be demonstrated (see (22)) that the hyperbolic system can be expressed in matrix form as:

$$\begin{aligned} \begin{bmatrix} h \\ U_{\xi} \end{bmatrix}_{,\hat{t}} + \begin{bmatrix} 0 & h \\ -\frac{P_{\xi\xi}}{\rho h} & 0 \end{bmatrix} \begin{bmatrix} h \\ U_{\xi} \end{bmatrix}_{,\hat{\xi}} &= \begin{bmatrix} 0 \\ g \sin \beta + \frac{1}{\rho} \frac{\partial P_{\xi\xi}}{\partial \xi} + \frac{2P_{\xi\eta}}{\rho h} \end{bmatrix} \Rightarrow \\ \Rightarrow \mathbf{y}_{,\hat{t}} + \mathbf{C} \mathbf{y}_{,\hat{\xi}} &= \mathbf{d}. \end{aligned}$$

The notations $_{,\hat{t}}$ and $_{,\hat{\xi}}$ represent the derivation with respect to \hat{t} and $\hat{\xi}$.

The characteristic celerities of the system are the eigenvalues of matrix \mathbf{C} :

$$\begin{vmatrix} -c & h \\ -\frac{P_{\xi\xi}}{\rho} & -c \end{vmatrix} = c^2 + \frac{P_{\xi\xi}}{\rho} = 0,$$

and so:

$$c_{1,2} = \pm \sqrt{-\frac{P_{\xi\xi}}{\rho}} = \pm \sqrt{k_{a/p} \frac{h}{2} (g \cos \beta + \chi U_{\xi}^2)}.$$

In presence of convex curved slopes the centrifugal term becomes negative and, if the flow velocity is high, the radicand can become negative. In such cases the physical model fails to describe the phenomenon, because the flow loses adhesion to the bottom and a jump takes place.

Going back to the artificial viscosity (4.32), the term depending on α_v is linear with respect to the velocity difference and produces a pressure that prevents particles from getting too close. The term depending on β_v is a quadratic function of the velocity difference and it becomes important when the velocity difference is large with respect to the characteristic celerity, i.e. in presence of strong shocks. Finally, the term depending on γ_v prevents singularities. As shown in Figure 4.10, the viscosity term is maximum for $\xi_{ij} = \gamma_v^{1/2} \hat{s}_{ij}$, being s_i the dimension of the support of the generic node i . If particles get too close the viscosity term vanishes, and so γ_v must be chosen small enough. The values proposed by Monaghan (20) for these three parameters are $\alpha_v = 1$, $\beta_v = 2$ and $\gamma_v = 0.01$.

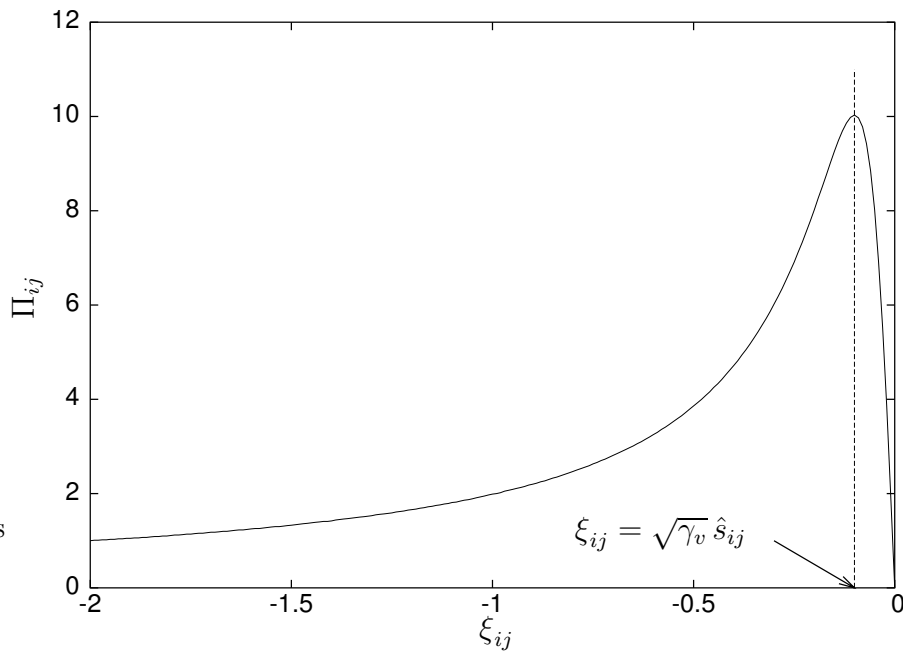


Figure 4.10: The dependence of the artificial viscosity Π_{ij} on ξ_{ij} (from (22))

As observed by Monaghan (20), this artificial viscosity is Galilean invariant, that is vanishes for rigid body rotations, and conserves total linear momenta.

4.4.3 Time integration

The MLSPPH continuity equation (4.30) and momentum equation (4.31) are integrated over time with a predictor–corrector algorithm. Being:

$$\frac{d\mathbf{y}}{dt} = \mathbf{f}(\mathbf{y}, t)$$

the MLSPH discretized system, at a first try the unknown vector \mathbf{y} is estimated at generic time t^{n+1} as a function of its value at the previous instant:

$$\mathbf{y}_{(0)}^{n+1} = \mathbf{y}^n + \mathbf{f}(\mathbf{y}^n, t^n) \Delta t.$$

Then \mathbf{y} at intermediate time $t^{n+1/2}$ is evaluated by interpolation:

$$\mathbf{y}_{(0)}^{n+1/2} = \frac{\mathbf{y}^n + \mathbf{y}_{(0)}^{n+1}}{2},$$

and is used to determine \mathbf{y}^{n+1} at next try through:

$$\mathbf{y}_{(1)}^{n+1} = \mathbf{y}^n + \mathbf{f}\left(\mathbf{y}_{(0)}^{n+1/2}, t^{n+1/2}\right) \Delta t.$$

An iterative procedure then starts up. At the generic step k :

$$\begin{aligned} \mathbf{y}_{(k)}^{n+1} &= \mathbf{y}^n + \mathbf{f}\left(\mathbf{y}_{(k-1)}^{n+1/2}, t^{n+1/2}\right) \Delta t, \\ \mathbf{y}_{(k)}^{n+1/2} &= \frac{\mathbf{y}^n + \mathbf{y}_{(k)}^{n+1}}{2}. \end{aligned}$$

The iterations are interrupted when the difference between two subsequent tries is less than a predefined tolerance.

The integrals B_{ij} are evaluated by means of the one-point quadrature, renouncing the consistency in the representation of the flux terms:

$$B_{ij} = l_i \nabla \phi_j(\xi_i) = l_i \nabla_i \phi_j.$$

C_{ij} is calculated according to the compatibility condition (4.22).

As suggested by Monaghan (20) and Morris (21), the time integration step is limited in order to prevent the rise of instabilities. Three different conditions have been imposed:

$$\Delta t < \tau_u \frac{s_i}{U_{\xi_i}},$$

which prevents each particle i from covering a space greater than a τ_u fraction of its support dimension s_i during the single time step Δt . τ_u has been taken equal to 0.2.

$$\Delta t < \tau_c \frac{s_i}{c_i},$$

which is a Friedrichs–Levy–Courant type condition. We used $\tau_c = 0.2$.

$$\Delta t < \tau_a \sqrt{\frac{s_i}{a_i}},$$

being a_i the MLSPH acceleration:

$$a_i = \frac{1}{A_i} \left((\mathcal{G}_i - \mathcal{R}_i) l_i - \frac{1}{2} \sum_{j=1}^n (\mathcal{P}_j + \mathcal{P}_i + \Pi_{ij}) (C_{ij} + B_{ij} - B_{ji}) \right).$$

The optimal value of τ_a was 0.1.

4.4.4 The initial condition

The initial dimension d_i^0 of the influence domain of each node i has been chosen in order to ensure the invertibility of the MLS matrix (4.12). For each calculation point, the minimum number of adjacent nodes for the MLS matrix invertibility is equal to the number of MLS base functions, but if the nodes are aligned in the plane $\xi\zeta$, it can be insufficient. For the stability of the simulation, it would be better to have a greater number of neighboring nodes, but incrementing the size of the nodal support the accuracy decreases and the computational time grows. For the sake of simplicity, the support domain approach has been preferred to the influence domain support for the initial definition of the nodal support dimension (see §4.1). The initial dimension of support domain s_i^0 is defined through equation (4.2):

$$s_i = \alpha_s d_{ci},$$

where d_{ci} represents the nodal spacing close to node i and is calculated through equation (4.3).

As in Dilts (7), the initial “length” associated to each node is calculated as:

$$l_i^0 = s_i^0 \frac{l_{tot}^0}{\sum_{j=1}^n s_j^0},$$

where l_{tot}^0 is the initial total length of the granular mass. The constant area A_i associated to each node i is defined at the initial instant as:

$$A_i = l_i^0 h_i^0.$$

4.4.5 The time evolution of support domains

A typical equation used in SPH methods to update the size of support domain is in the one-dimensional case:

$$\frac{1}{s} \frac{ds}{dt} = \frac{\partial U_\xi}{\partial \xi}.$$

The comparison with the continuity equation (4.23) brings to the relation:

$$\frac{1}{s} \frac{ds}{dt} = \frac{1}{h} \frac{dh}{dt}.$$

Descending from this, the relation suggested by Liu (17) to update s_i is:

$$s_i^{n+1} = s_i^n \left(1 - \frac{h_i^{n+1} - h_i^n}{h_i^n} \right).$$

4.4.6 Comparison with experiments

Convex and concave curved chute

MLSPH models turned out to be suitable for cases characterized by strong deformations and by separations of mass, because of the absence of a mesh. The movements of each node are not bound by topological relations with the neighboring nodes. For this reason the *mlsph1d* model has been tested against the experimental results of Greve and Hutter (10), relevant to a convex and concave curved chute, introduced in §2.4.3. The presence of a bump in the center of the channel causes the separation of the flowing mass. One part of the avalanche stops above the bump. The other part runs over the bump and stops where the slope reduces definitively.

In Figure 4.11 the MLSPH one-dimensional model *mlsph1d* and the original one-dimensional model with constant width $1d$ are compared. The used values of the physical parameters are the ones which gave the best results with the $1d$ model: $\phi = 37^\circ$, $\delta = 26.5^\circ$, $k = 0.4$. During the initial phases of motion, the mass in the *mlsph1d* simulation is more elongated and has smaller depth than in the experimental data. The simulation of the model $1d$ provides a better fitting. When the mass begins to experience the presence of the bump (non-dimensional time $t = 3.10$) the results of the two simulations are comparable and fit the experimental data quite well. During the final phases the behaviors of the two models differentiate again. The $1d$ model describes better the upstream deposit. The *mlsph1d* reproduces correctly the shape of the downstream deposit, but it overestimates its volume.

Simulation	m	α_s	α_v	β_v	γ_v
<i>g29.mlsph1d.1</i>	2	10.0	0.0	0.0	0.01
<i>g29.mlsph1d.2</i>	2	3.0	0.0	0.0	0.01
<i>g29.mlsph1d.3</i>	2	3.0	1.0	2.0	0.01
<i>g29.mlsph1d.4</i>	3	3.0	1.0	2.0	0.01

Table 4.3: The numerical parameters characterizing the simulations performed with the model *mlsph1d*. All the other parameters are the same for all the simulations: the number of nodes $n = 40$, the coefficients of time step corrections $\tau_u = 0.2$, $\tau_f = 0.1$, $\tau_c = 0.2$. The physical parameters are $\phi = 37^\circ$, $\delta = 26.5^\circ$ and $k = 0.4$. It is to point out that k , the corrective factor used to keep into account the lateral friction, is the one proposed by Savage and Hutter (28) (see equation (2.18)).

Both the simulations show a narrow strip of mass between the two deposits. In the simulation of the *mlsph1d* model it is more thick. The particles at the interior ends of the two deposits have a low value of h and consequently they have a large support domain. They are responsible for the presence of the strip. It is not gained a complete separation between the two deposits. Using the influence domain approach instead of the support domain approach, this problem is likely to reduce. Incrementing the nodal density near to these areas during the simulation should give good results, too.

Figure 4.12 shows the effects of adding the artificial viscosity (4.32) to the pressure term in the MLSPH momentum equation (4.31). In the simulation *g29.mlsph1d.2* no viscosity is inserted. In the simulation *g29.mlsph1d.3* the values of the artificial viscosity parameters are the ones suggested by Monaghan (20): $\alpha_v = 1$, $\beta_v = 2$ and $\gamma_v = 0.01$. α_s was set to 2, the minimum value which prevented the rise of numerical instabilities. The artificial viscosity gets effective when the mass is compressing and so no difference is noticeable until the instant $t = 3.10$. Nevertheless, only during the final phases of the motion the two simulations differ considerably. The downstream deposit of simulation *g29.mlsph1d.3* is more spread and thin than in simulation *g29.mlsph1d.2*. The accuracy of the fitting decreases. The use of the artificial viscosity should be limited to cases where strong instabilities arise.

Another solution in presence of instabilities could be to increment the initial number of neighboring nodes for each particle. In Figure 4.13 the results of simulation *g29.mlsph1d.1*, with $\alpha_s = 10$, and simulation *g29.mlsph1d.2*, with $\alpha_s = 3$ are compared. In the first case the size of the support domain and consequently the number of neighboring nodes is

strongly incremented. The MLS approximants make a mean over a greater number of nodes and the result is a flattening of the final downstream deposit. However the loss of accuracy is less pronounced than with the artificial viscosity.

Finally, in Figure 4.14 the effect of incrementing the number of base function is shown. In the simulation *g29.mlsph1d.4*, the parameter α_s was brought to 6, in order to use 3 base functions instead of 2, without adding artificial viscosity. The increase of the computational time, from 358 s in simulation *g29.mlsph1d.2* to 1022 s in simulation *g29.mlsph1d.4* is not rewarded with an improvement in numerical accuracy. The differences are very small and they can be distinguished only at the very final instants of motion.

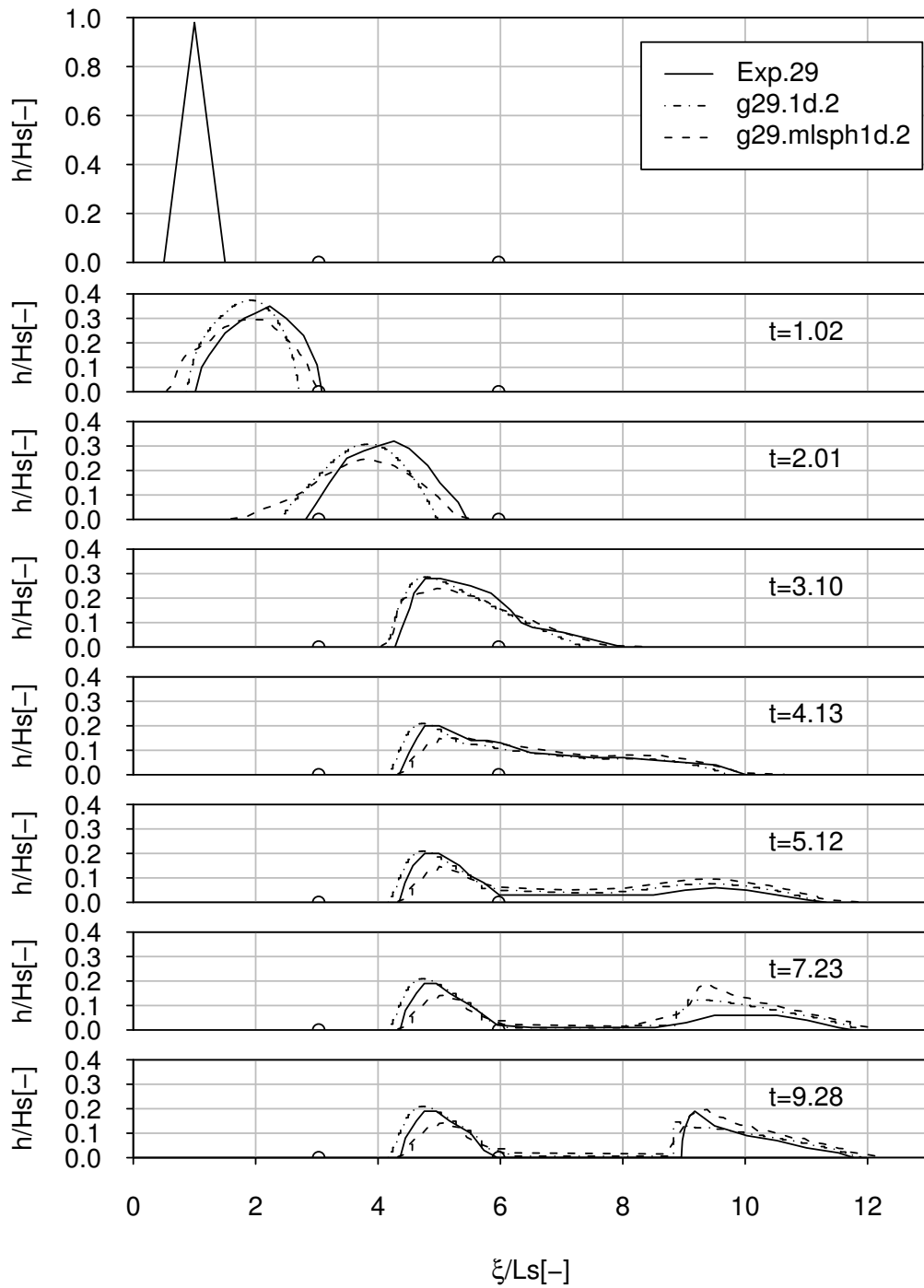


Figure 4.11: Convex and concave curved chute. *Exp.29*. Comparison of experimental and numerical profiles obtained with the one-dimensional MLSPH model and with the original finite difference one-dimensional model. The comparison is between the numerical simulations *g29.mlsp1d.2*, characterized by the parameters reported in Table 4.3 and *g29.1d.2*, reported in Table 2.5. h is non-dimensionalized through $H_s = 0.1\text{ m}$, ξ through $L_s = 0.3\text{ m}$, t through $T_s = L_s/U_s = L_s/\sqrt{gH_s} = 0.30\text{ s}$. Circles signal the positions of points of maximum and minimum slope.

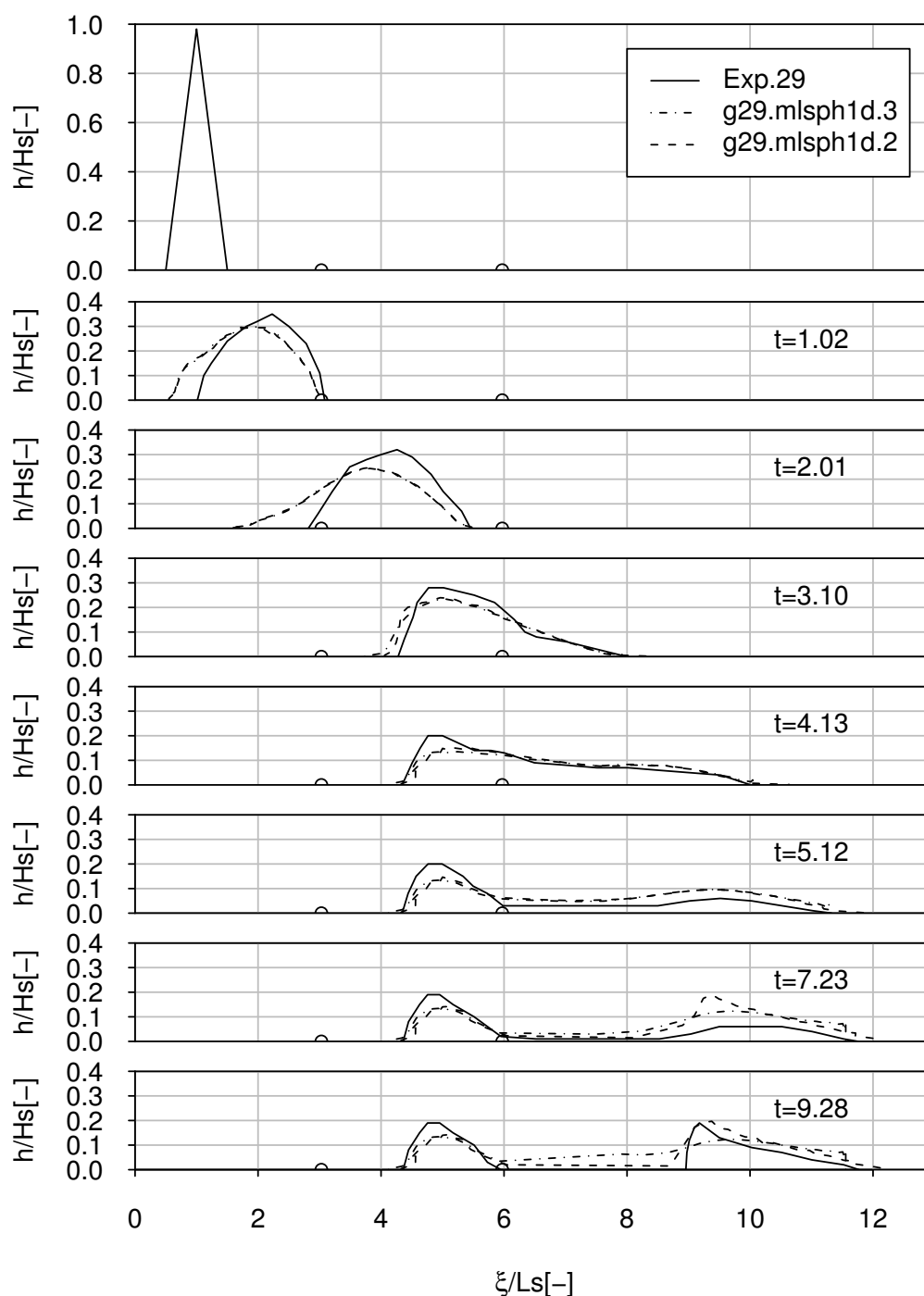


Figure 4.12: Convex and concave curved chute. *Exp.29*. Comparison of experimental and numerical profiles obtained with the one-dimensional MLSPH model. The comparison is between the numerical simulation *g29.mlsph1d.3* and *g29.mlsph1d.2*, characterized by the parameters indicated in Table 4.3. Both the simulations have the same value of α_s . The artificial viscosity is introduced in simulation *g29.mlsph1d.3*. h is non-dimensionalized through $H_s = 0.1$ m, ξ through $L_s = 0.3$ m, t through $T_s = L_s/U_s = L_s/\sqrt{gH_s} = 0.30$ s. Circles signal the positions of points of maximum and minimum slope.

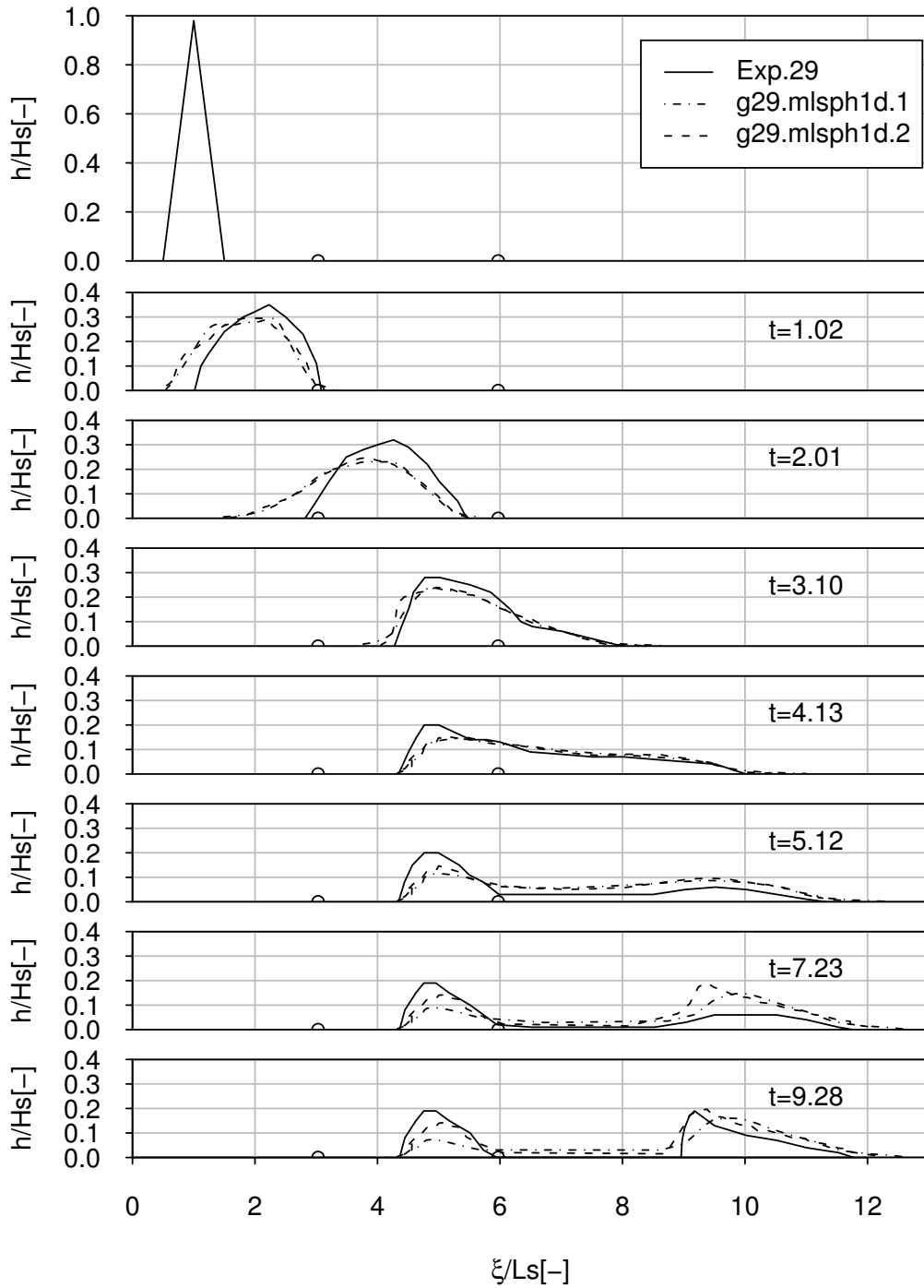


Figure 4.13: Convex and concave curved chute. *Exp.29*. Comparison of experimental and numerical profiles obtained with the one-dimensional MLSPH model. The comparison is between the numerical simulations *g29.mlsph1d.1* and *g29.mlsph1d.2*, characterized by the parameters reported in Table 4.3. Both the simulations are without viscosity. The simulation *g29.mlsph1d.1* has $\alpha_s = 10$, *g29.mlsph1d.2* has $\alpha_s = 3$. h is non-dimensionalized through $H_s = 0.1\text{ m}$, ξ through $L_s = 0.3\text{ m}$, t through $T_s = L_s/U_s = L_s/\sqrt{gH_s} = 0.30\text{ s}$. Circles signal the positions of points of maximum and minimum slope.

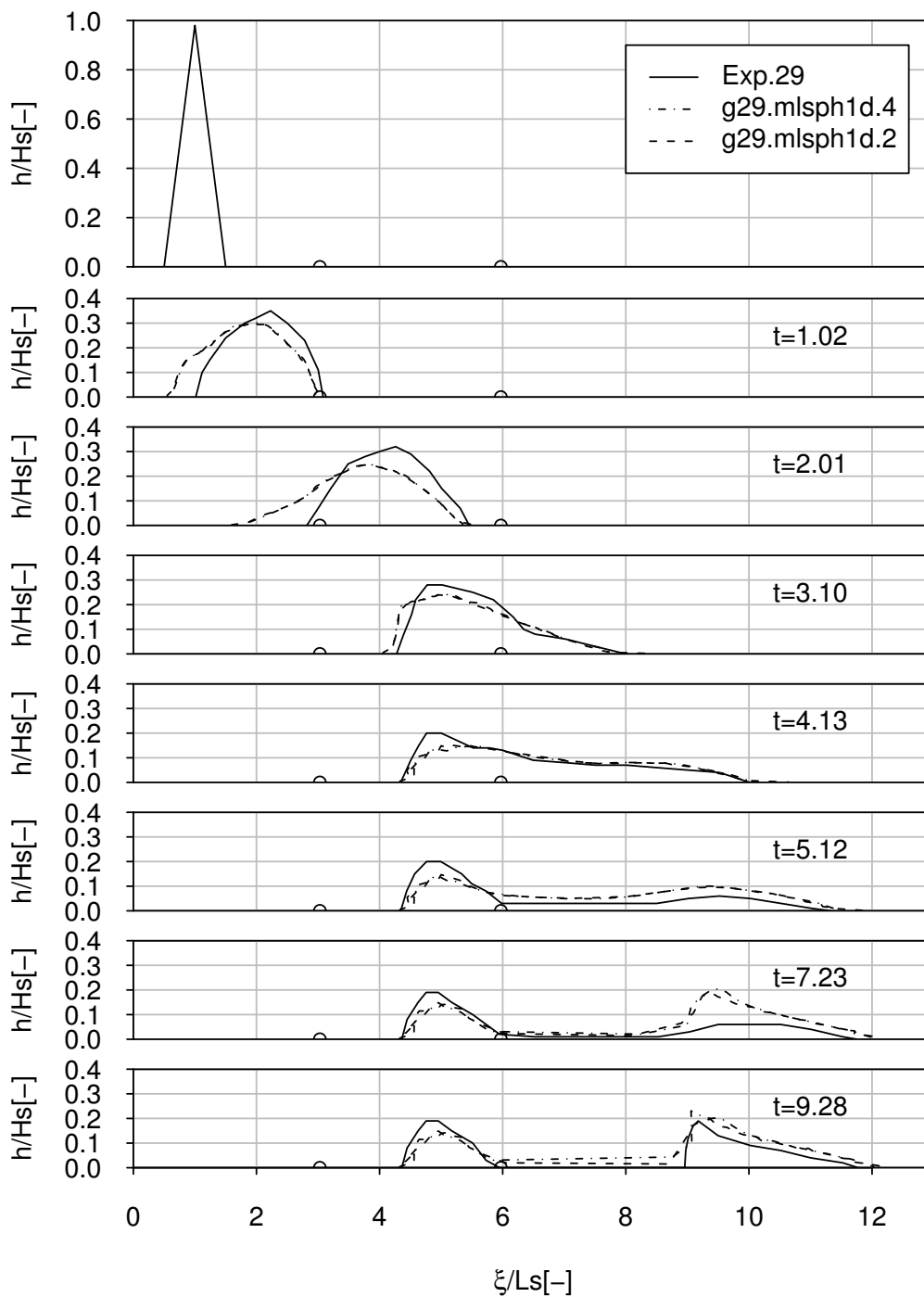


Figure 4.14: Convex and concave curved chute. *Exp.29*. Comparison of experimental and numerical profiles obtained with the one-dimensional MLSPH model. The comparison is between the numerical simulations *g29.mlsph1d.4* and *g29.mlsph1d.2*, characterized by the parameters reported in Table 4.3. In the simulation *g29.mlsph1d.4* the number of base function is incremented to 3, against the 2 base function of simulation *g29.mlsph1d.2*. The simulation *g29.mlsph1d.4* has $\alpha_s = 6$, while *g29.mlsph1d.2* has $\alpha_s = 3$. h is non-dimensionalized through $H_s = 0.1\text{ m}$, ξ through $L_s = 0.3\text{ m}$, t through $T_s = L_s/U_s = L_s/\sqrt{gH_s} = 0.30\text{ s}$. Circles signal the positions of points of maximum and minimum slope.

4.4.7 Final remarks

The *mlsph1d* turned up to be less accurate than the original one–dimensional model with constant width, especially if the artificial viscosity is added. A possible reason could be the loss of consistency due to the use of the one–point quadrature rule. The model is no more convergent. Furthermore, according to the approach of the support domain, with an uniform initial distribution of nodes, the boundary nodes have a support which is two times larger than the interior nodes. This fact is responsible for the absence of a real mass separation between the two masses in the simulation of the experiment of Hutter. A solution to this could be to increment the nodal density near to the boundary. The application of the influence domain approach could improve the quality of the simulation as well.

Another limit of MLSPH method is the considerable increment of computational time. For example the simulation *g29.mlsph1d.2* required a computational time of 358 s, with a value of 97% of used CPU, while the simulation *g29.1d.2* required only 3 s and a value of 81% of used CPU. The increase in computational cost is a deficiency of all meshless methods. The application of more recent methods like the normalized *SPH* should improve this aspect.

For all these reasons the application of meshless methods to the one–dimensional cases is not justifiable, except in order to test it with the aim of extending the application of meshless methods to the two–dimensional model. In this case the benefits should be tangible. The absence of nodal links should allow the flowing mass to easily adapt to the varying topography.

5 Field activity

The avalanche site of Lavina Granda in the mountain range of Vigolana (Figure 5.1), close to Trento, has been surveyed in order to examine the physical processes that generate snow avalanches and to collect data suitable for the calibration of the numerical models.

5.1 The Vigolana mountain range

The Vigolana range lies to the south-east of Trento. It bounds to the north on the ValSorda and the Vigolo Vattaro Plateau, to the east on the Centa Valley and the Carbonare Saddle, to the south on the Sommo Pass, the Folgaria Plateau and the Cavallo Stream, to the west on the Adige Valley. It is 65 km^2 wide and its ridge has the shape of a L , with a first segment oriented from north-west to south-east, and a second segment oriented from north-east to south-west. The ridge goes from the Ceriola Peak (1935 m a.s.l.) (the north-west edge) towards the Vigolana Peak (2148 m a.s.l.) and the Filadonna Peak (2150 m a.s.l.). Here the mountain chain bends to south-west towards the Cornetto Peak (2060 m a.s.l.).

All the Vigolana range is characterized by calcareous outcrops. The ridge bounds to the east and to the north the wide Scanuppia Plateau, characterized by Karstification and crossed by only two valleys, the Scaletta Valley in the south-west, and the Gola Valley in the south. Steep calcareous cliffs cover the northern and eastern sides of Vigolana, and are furrowed by deep dry valleys. In sequence, from the north-west edge to the north-east edge, there are the Cestara Gorge, the Valley of Stanghet Stream, the Zirezara Valley, the Scalone valley, the Calcarotta Valley, the Lavina Granda Valley, the Larga Valley and the Bianca Valley. The eastern side is crossed by the valleys of the left tributaries of the Centa Torrent.

As far as the vegetation is concerned, sub-Mediterranean species prevail up to an altitude of 400 m a.s.l. . Then, from 400 m a.s.l. to 900 m a.s.l. , there are mixed woods of chestnuts, horn-beams, hazels, lindens, ashes, elms, maples. Woods of beech cover the slopes of the Vigolana from 900 m a.s.l. to 1400 m a.s.l. . Beech is mixed with Norway

spruce, silver fir and larch, which are dominant at higher altitudes, up to the superior limit of vegetation at 1600 *m a.s.l.*. As the altitude gets higher, forest trees are replaced by bushes of mountain pine, alpine grasslands and screes.

The climate is characterized by rainy autumns, with peaks of precipitations, which can be snowy at high altitudes, in November. A minor period of intense precipitation can occur during the spring (snowy in the first part of the season) or during the summer. Winter is usually dry.

5.2 The avalanche site of Lavina Granda

Lavina Granda is a valley sited in the northern mountainside of Vigolana. It has two sub-catchments, located between the Madonnina refuge and the Gabrielli Cave. The maximum altitude is 2132 *m a.s.l.*. The two catchments join at the altitude of 1560 *m a.s.l.*. The channel intersects two dirt roads, at the altitudes of 1280 *m a.s.l.* and 1110 *m a.s.l.*. A transversal check dam, at the altitude of 780 *m a.s.l.*, interrupts the course of the stream. The channel is averagely north-facing, as shown in the aspect map (Figure 5.4). The slope map is shown in Figure 5.3. The altimetric profile of the channel and the trends of the slope angle and of the width with respect to the cumulative horizontal distance are represented in Figure 5.11. All these maps have been obtained through the elaboration of the Digital Elevation Model and of the colour digital ortho-photo of 1999, provided by the Autonomous Province of Trento. The bottom of the channel is covered by sand, gravel and boulders with maximum size of 1 *m*. In several points the channel has rocky outcrops, associated with abrupt slope increase and often narrowing of the channel.

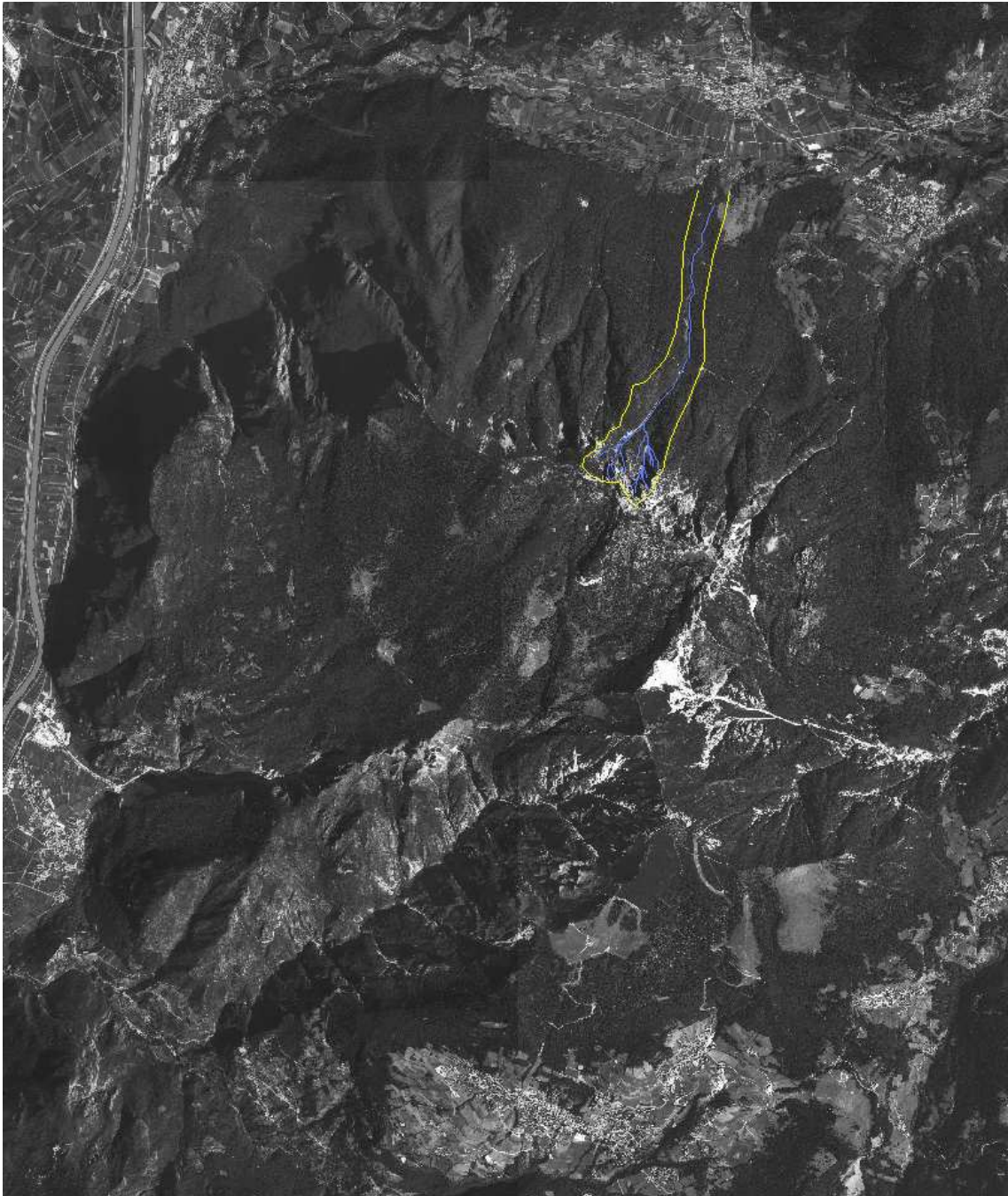


Figure 5.1: The Vigolana range and the Lavina Granda Valley on the black and white ortho-photo of 1994.

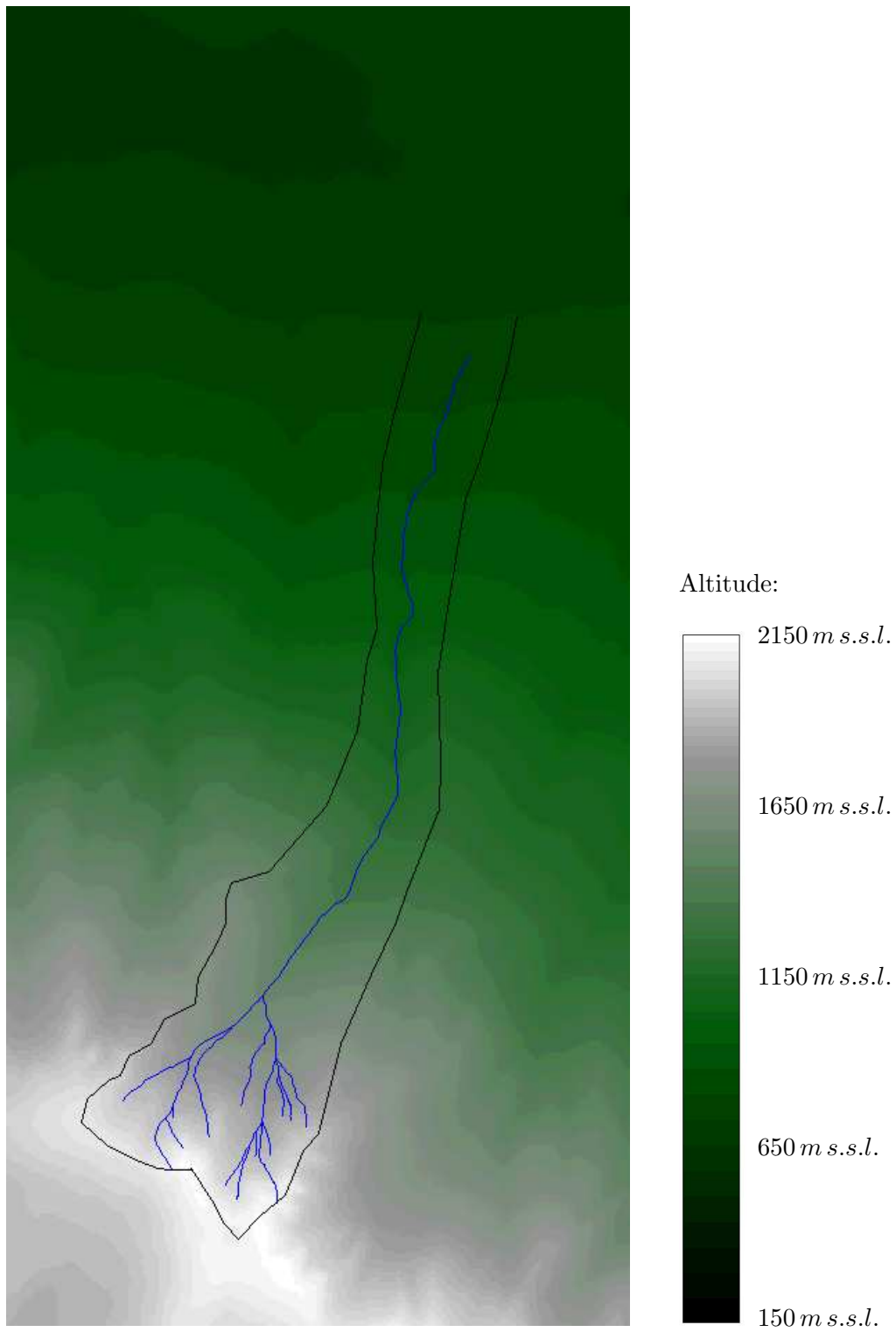


Figure 5.2: The Digital Elevation Model with resolution of 10 *m* of the Lavina Granda valley.

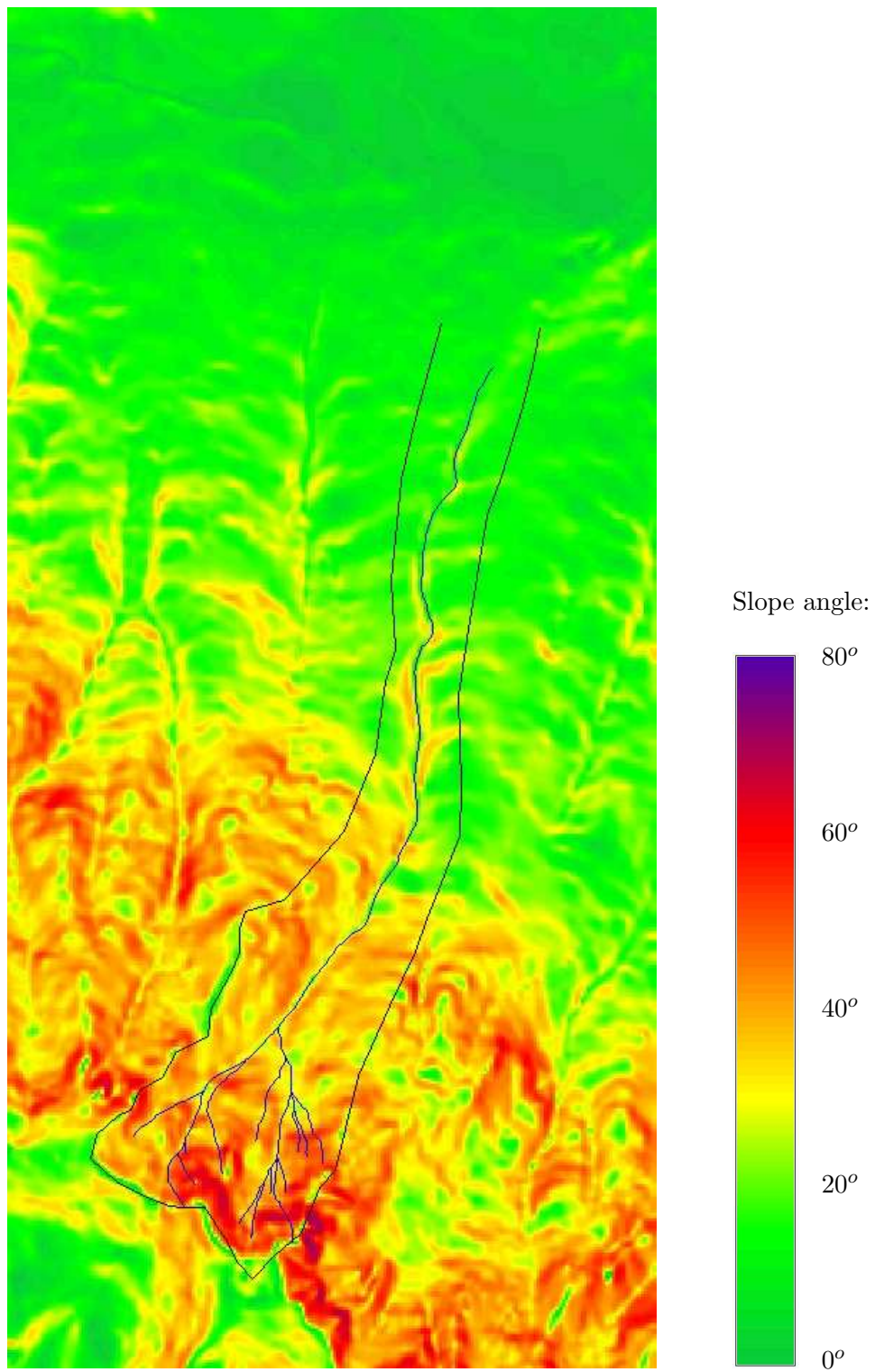


Figure 5.3: The slope map. The slope angle is measured in sexagesimal degrees on the horizontal.

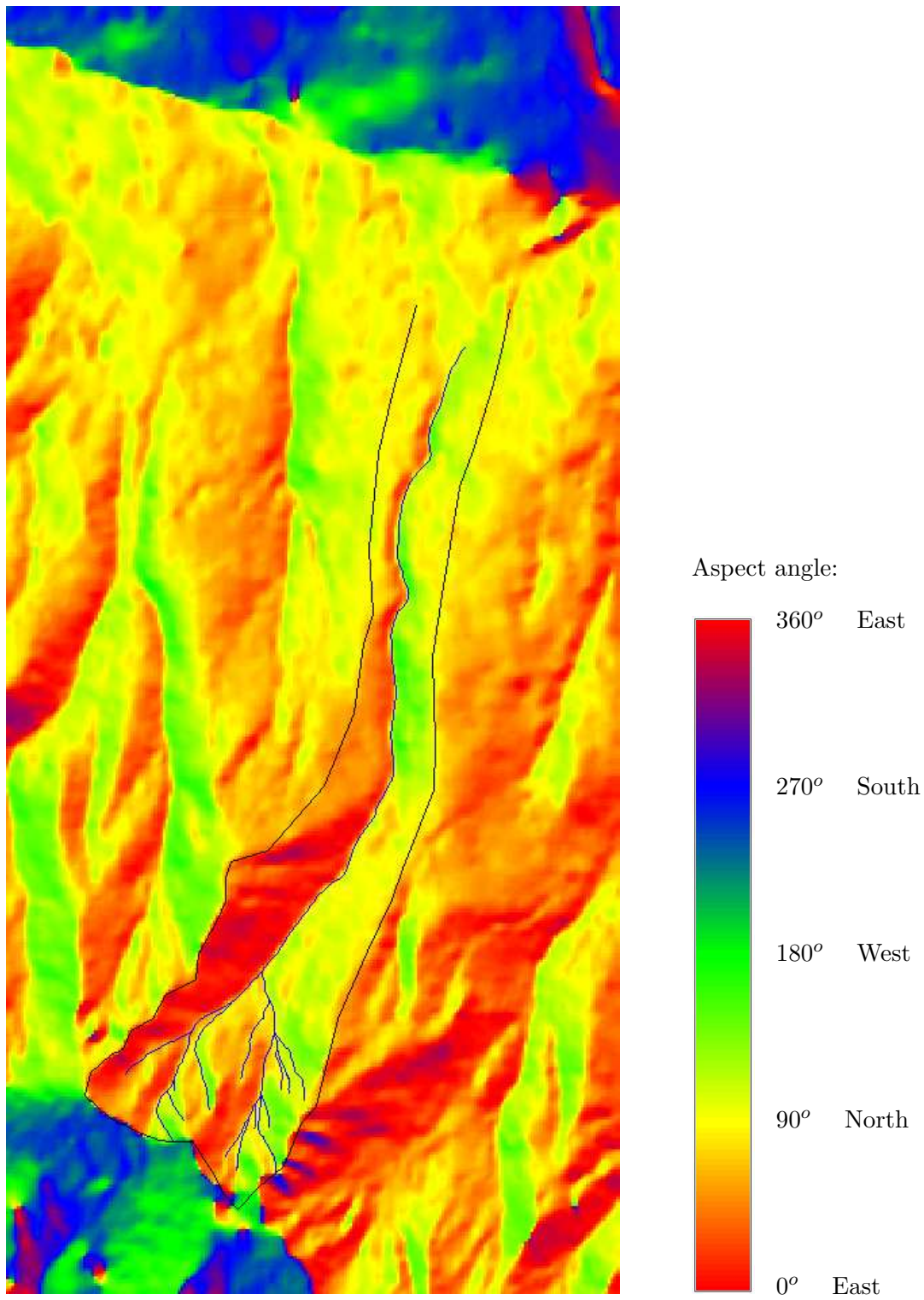


Figure 5.4: The aspect map. The aspect angle is measured in counterclockwise sexagesimal degrees from east.

5.3 Available data

The available cartographic products relevant to this area are: a topographic map (the Provincial Technical Map, scale 1:10000), the Digital Elevation Model with resolution of 10 m (Figure 5.2), a black and white digital ortho-photo of the year 1994 (resolution 1 m, scale 1 : 10000), a colour digital ortho-photo of the year 1999 (resolution 0.1 m, scale 1 : 10000).

The Snow, Avalanches and Meteorology Office of the Autonomous Province of Trento is responsible for the avalanche surveys drawing up and for the updating of the Avalanches Registers and of the Maps of Likely Avalanche Location.

A satellite image of the 30th of March 2004, having resolution 2.8 m, was supplied by the hydrology group of the Department of Civil and Environmental Engineering of Trento.

5.3.1 Avalanche registers and the Map of Likely Avalanche Location

The avalanche activity in Lavina Granda has been recorded since 1979. Since 1988 new more detailed registers are available.

According to the Avalanche Register of the Snow and Avalanches Office of the Province of Trento, the avalanches that take place in the Lavina Granda Valley (identified as 04309 and shown in the Map of Likely Avalanche Location, Figure 5.7), can occur more than one time every year. Usually they are granular dense avalanches of moist snow (see Figure 5.5), but more rarely dry powder avalanches can happen (see Figure 5.6). The avalanches of Lavina Granda usually occur in the period that goes from January to March, due to the fresh snow or rain overload or to the temperature rise, and they mostly start as cohesionless avalanche. The maximum recorded volume is relevant to the event that occurred on the 27th of January of 1985. A volume of 100000 m³ reached the altitude of 900 m a.s.l., running into the forest and pulling down a mass of 40000 kg of beech trees.

The snowpack involved by the detachment in the starting zone is up to 5 m deep, considering also the snow drift, and covers an area up to 20000 m² wide.

Quite frequently the avalanches reaches the dirt road at the altitude of 1280 m a.s.l. and more rarely the dirt road at the altitude of 1110 m a.s.l.. The most disastrous event within living memory occurred in 1929. The avalanche reached the area now occupied by the football field at the altitude of 690 m a.s.l..



Figure 5.5: The deposit of a granular avalanche in Lavina Granda site (January 16th 2004).



Figure 5.6: The effects of a powder avalanche in Lavina Granda site (March 21st 2004).

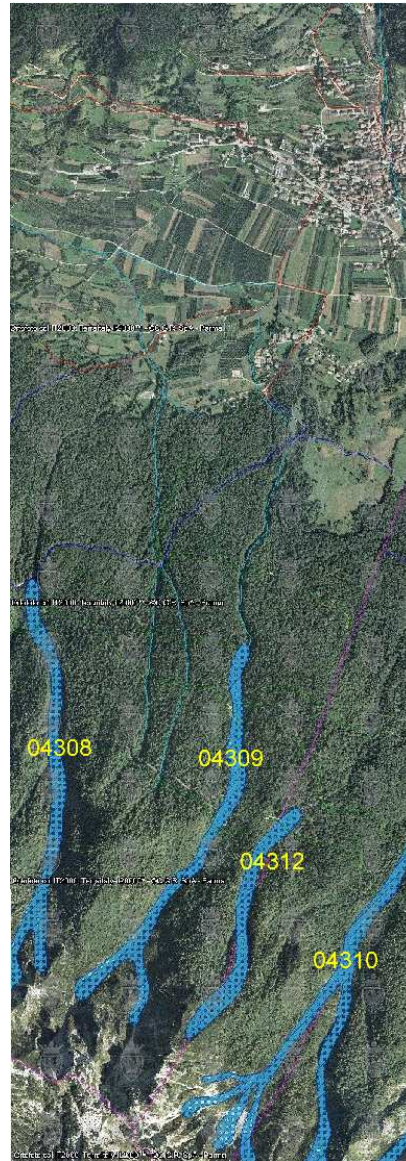


Figure 5.7: Map of Likely Avalanche Location. From Autonomous Province of Trento (<http://www.gis.provincia.tn.it/>).

5.3.2 The starting zone

The main features of the terrain: slope, aspect, vegetation

The starting zones in the two sub-catchments have been drawn by coupling the informations about slope (Figure 5.9), wood cover (Figure 5.10) and the observations made during the surveys.

The slope is the main factor that induces the detachment of an avalanche. The discrimination of different types of snow movement as a function of the slope angle (McClung and Schaerer, (19)) is reported in Table 5.1.

Slope Angle [°]	Avalanche type
10–25	Wet snow avalanches
25–35	Rare (large) slab avalanche; wet loose snow avalanches
35–45	Slab avalanches with generic dimension
45–55	Frequent small slab avalanches
30–60	Frequent dry loose snow avalanches
60–90	Rare avalanches; frequent sluffs

Table 5.1: The distinction between different types of avalanches occurring at different slope angles of the mountainside.

As can be seen in Figure 5.9, the right sub-catchment is crowned by high rock walls, starting from the altitude of 1900 m a.s.l. and culminating at the maximum altitude of 2132 m a.s.l. . The slope angle exceeds 60° and the fresh snow is discharged through frequent sluffs occurring during the snowfalls. The fallen snow accumulates at the base of the cliff, and, depending on the stability state of the snowpack below, it can either press and consolidate the snow cover or trig loose snow movements or slab avalanches. At the right side of the right starting zone lies a sub-catchment that usually does not contribute to the avalanche of Lavina Granda, because the masses falling down along the steep mountain side at the foot of the Madonnina Refuge (Figure 5.8), after a jump at the altitude of 1800 m a.s.l. , stop on a grassland characterized by a considerable slope reduction. Only in extreme conditions these volumes can reach the main channel.

The left starting zone is much more complex morphologically. Two couloirs are located in the right side. The snow, falling from the lateral rock walls and steep sides, accumulates

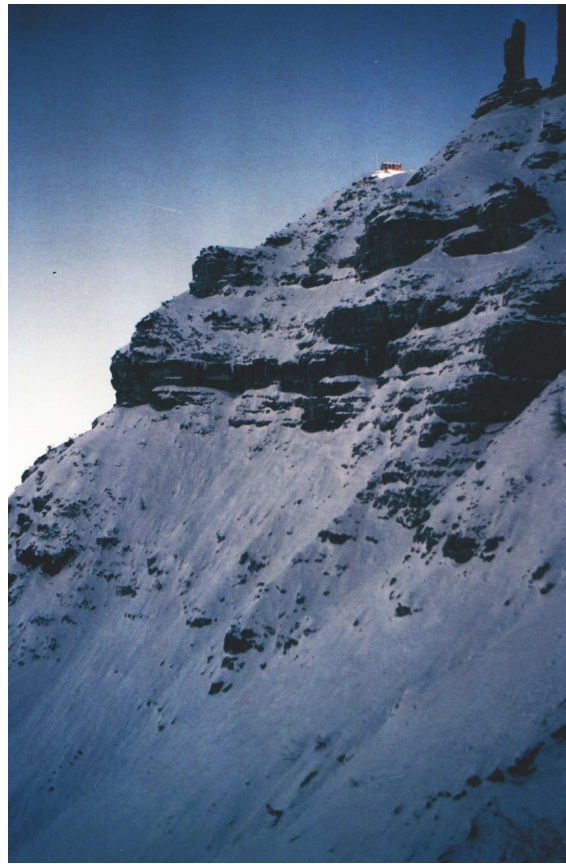


Figure 5.8: The steep slope below the Madonna Refuge (December 12th 2004).

along the channel, and can be destabilized afterwards due to a temperature rise or an overload. The upper part of the left side is characterized by a bowl-shaped slope, suitable for the snow drift accumulation, with inclinations ranging from 30° to 50° on the horizontal. This area seems to be prone to the release of quite large slab avalanches, but the presence of a wood of mountain pine suggests that such events have not taken place for a long time.

Another important factor for the release of snow avalanches is represented by the exposures of the mountain sides. Going from the left to the right sides of the channels in the starting zones, the exposure passes from north-east to north-west, as shown in Figure 5.4, with an average aspect counterclockwise angle of 92° from east in the left sub-catchment and of 83° in the right one. North facing mountainsides receive an amount of heat for solar radiation that can be 10 times smaller than south facing sides (1). Furthermore they release heat through long wave irradiation (19). After the snowfalls, all the isothermal metamorphic processes, like rounding and sintering of snow, are very slow, preventing the

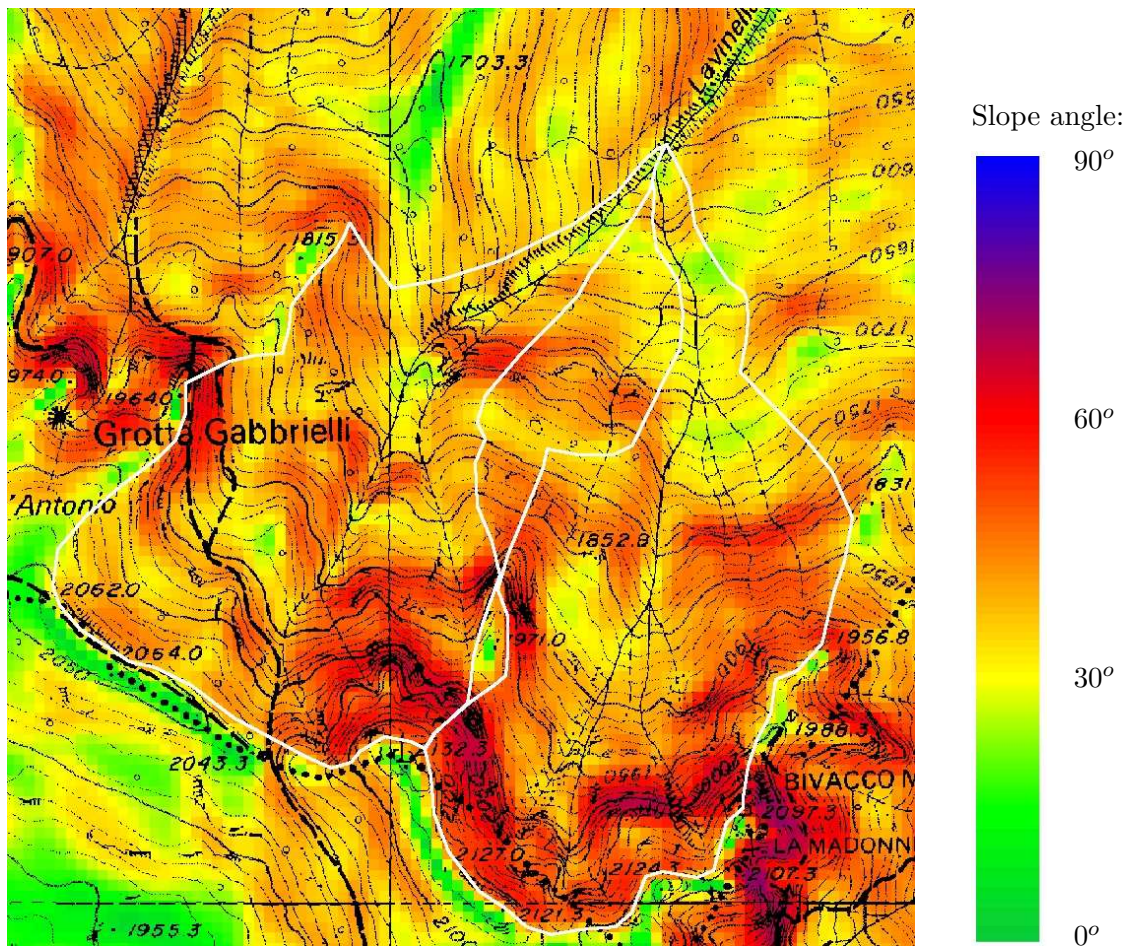


Figure 5.9: The slope map of the starting zone. The slope angle is measured in degrees on the horizontal. The assumed two sub-catchments are delimited by the white line.

settlement of the snowpack. Besides, because of the large temperature gradients, faceting processes take place, producing weak layers in the snow cover. For all these reasons the stabilisation of the snowpack on north-facing mountainsides is strongly slowed down.

The two starting areas are very wide. The right orographic sub-catchment has a maximum estimated surface of 146000 m^2 , while the left sub-catchment is 148600 m^2 wide. Because of the complexity of the topography the contemporary involvement of the entire sub-catchments is unlikely, but it cannot be, a priori, excluded.

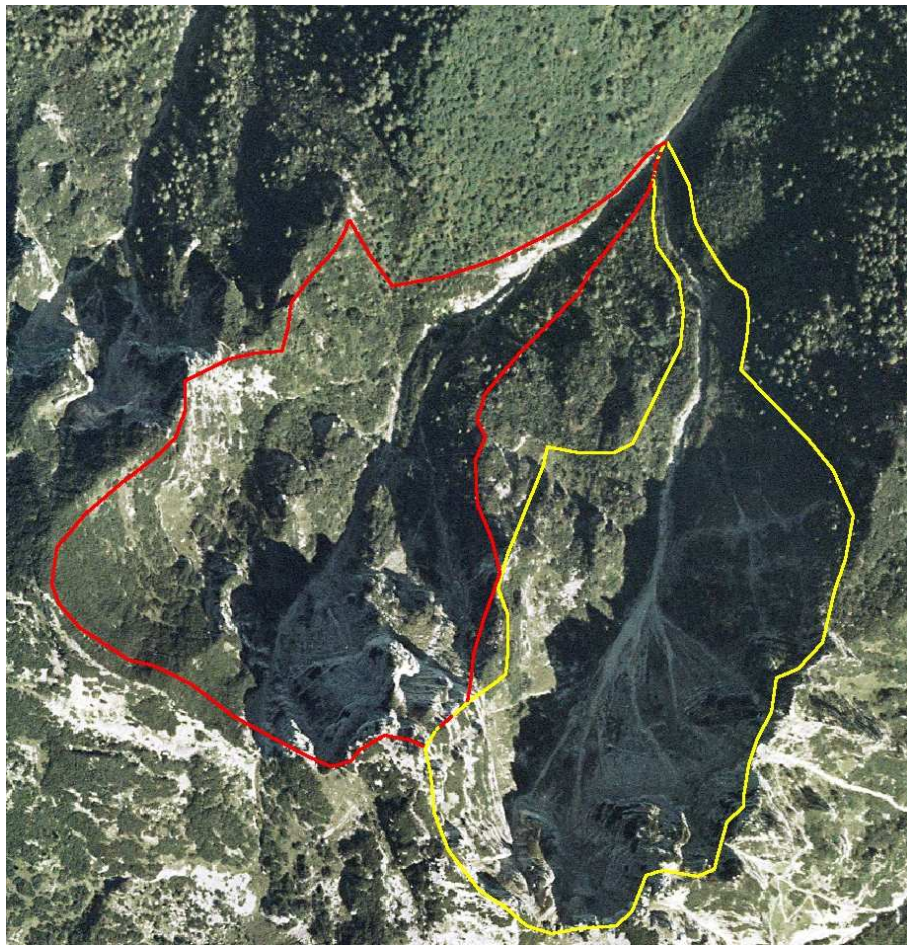


Figure 5.10: The ortho-photo of the starting zone, with the two assumed sub-catchments, delimited by the yellow and the red lines.

The assessment of initial volumes

The closest snow-weather stations, where snow depth data can be collected, are the ones at Sommo Pass, Mount Bondone and Mount Panarotta.

The snow-weather station of Sommo Pass is located at the east border of Vigolana mountain range. It has Gauss-Boaga coordinates 1671125 *m* east, 5087425 *m* north and an altitude of 1360 *m a.s.l.*. It is north-west facing.

The station of Mount Bondone is on the Bondone Plateau (1659160 *m* east, 5097650 *m* north), west of Vigolana, at the altitude of 1495 *m a.s.l.*, facing south.

The station of Panarotta is on the north-facing side of Mount Panarotta, at the altitude of 1775 *m a.s.l.*. The Gauss-Boaga coordinates are 1679499 *m* east, 5102262 *m* north.

All the stations are manual. The other available data are the instantaneous temperature of the air, the daily maximum and minimum temperature of the air, the daily temperature of the snow at the depths of 0.1 *m* and 0.3 *m*, the snowpack depth, the depth and the density of the fresh snow, the probe penetration, the observations of the cloudiness, of the weather conditions, of the aeolian activity, of the presence of snow cornices and of the occurrence of avalanches.

A statistical analysis of the maximum annual snow depth has been performed by Benfatto (2), for her degree thesis, using the data relevant to the period from 1980 to 2002. The maximum depths for the return periods of 100 and 300 years have been calculated, using different statistical distributions (lognormal, Gumbel, exponential and gamma with two parameters) and with different estimate methods (least squares, moments, maximum likelihood). The Pearson test has been applied in order to evaluate the goodness of the estimate.

Obviously, being the range of years very limited with respect to the chosen return period, results must be used with caution.

The best results for the station of Sommo Pass are the ones obtained with the lognormal distribution and the exponential distribution, with parameters estimated through the method of moments. The values of snow depth with a return period of 100 years in the two cases are 2.36 *m* and 2.47 *m* respectively. For the return period of 300 years, the estimated snow cover depth are 2.86 *m* and 2.97 *m* for the lognormal distribution and the Gumbel distribution.

The Mount Bondone station does not give acceptable results according to the Pearson test.

The best distributions for the station of Panarotta are the Gumbel distribution and the gamma distribution, with the parameters estimated through the method of moments. For the return period of 100 years, the corresponding values of snow depth are 2.79 *m* and 2.62 *m*. 3.16 *m* and 2.88 *m* are the values given by the Gumbel and the gamma distribution for a return period of 300 years.

It is possible to estimate the value of the snow depth h_0 at the mean slope and mean altitude of the two starting zones, by applying the corrective factors proposed by Salm et al. in the “Swiss Guidelines” (25):

$$h_0 = \left(h_0^* + \frac{0.05 (z - 2000)}{100} \right) f(\beta_0) + dw, \quad (5.1)$$

being h_0^* the snow depth at the altitude of 2000 *m a.s.l.*, z the altitude in *m a.s.l.*, dw the snow drift (usually ranging from 30 *cm* to 50 *cm*) and $f(\beta_0)$ a corrective factor related to

the mean slope of the catchment β_0 :

$$f(\beta_0) = \frac{0.291}{\sin \beta_0 - 0.202 \cos \beta_0}. \quad (5.2)$$

The left starting zone has a mean altitude of 1887 *m a.s.l.* and a mean slope angle of 44°. For the right sub-catchment the average altitude is 1883 *m a.s.l.* and the average slope is 46°. Applying the corrective factor (5.1) and (5.2) by Salm et al., we obtain, for a return period of 100 years, values of the maximum depth ranging from 1.3 *m* to 1.9 *m* on the right sub-catchment and from 1.4 *m* to 2.0 *m* on the left sub-catchment. The corresponding volumes go from 192000 m^3 to 281000 m^3 on the right sub-catchment and from 207000 m^3 to 299000 m^3 on the left sub-catchment.

For a return period of 300 years, the maximum depth goes from 1.5 *m* to 2.1 *m* in the right sub-catchment and from 1.6 *m* to 2.2 *m* in the left sub-catchment. The corresponding volumes range from 215000 m^3 to 309000 m^3 on the right sub-catchment and from 232000 m^3 to 330000 m^3 on the left one.

It is noticeable that the density of the snow in the starting area can be different from the density into the flowing avalanche. In particular, measures collected in various snow stations in Trentino show that fresh snow density can vary between 30 kg/m^3 and 250 kg/m^3 , depending on the water content and on the shape of the snow grains. McClung and Schaerer, in (19), suggest to evaluate the flowing density through the expression:

$$\rho = \rho_s C + \rho_a (1 - C),$$

where ρ_s is the density of the snow, ρ_a is the density of the air and C represents the volume concentration of the snow. For powder avalanches ρ_s is the density of the ice, that is 917 kg/m^3 , and C is about 0.01. The resulting flow density is 10 kg/m^3 . For dense snow avalanches ρ_s varies between 200 and 550 kg/m^3 and C in the range from 0.3 to 0.5. The corresponding density is normally included in the range between 60 and 275 kg/m^3 . It follows that the flowing volume can be definitely very different from the volume in the starting zone.

5.3.3 The track

The flowing track is represented by a channel, approximately half pipe shaped, with the bottom covered by sand, gravel and boulders with maximum diameter of more than 1 *m*. The altimetric profile and the trend of the width and of the slope angle versus the cumulative distance, obtained from the analysis of the ortho-photo, of the Digital Elevation

Model and of the Provincial Technical Map, are reported in Figure 5.11. The average slope, weighted through the length of each segment, is 38%, corresponding to a slope angle of 21° , a typical value for a sliding segment. The weighted standard deviation is 12% (7°). The slope variations along the channel are not negligible and can strongly affect the dynamic of the flowing mass. Abrupt slope decreases produce intermediate stops of the avalanche. The weighted mean width of the channel is of 16.1 m, with a weighted standard deviation of 5.4 m. The width normally ranges from 10 m to 15 m, but for a long segment of 700 m about the lower dirt road, it grows up to 20–25 m.

5.3.4 The runout zone

Just above the check dam at the altitude of 780 m *a.s.l.*, the track of the channel interrupts. The avalanche can go beyond the dam and in Figure 5.12. The planimetric and altimetric view of 6 possible rectilinear paths are shown. The orange path is the one covered by the historical avalanche of 1929, that reached the football field at the altitude of 690 m *a.s.l.*. The altimetric profile of the other two right paths is adverse to the continuing of the avalanche motion. The left paths pass through a tree forest that obstructs the passage of the avalanche. Nevertheless, for the presence of previous avalanche deposits, subsequent avalanches can deviate from the common paths. Furthermore, these considerations are valid for a dense snow avalanche, while a powder avalanche can be barely influenced by the morphology of the terrain and by the presence of the wood.

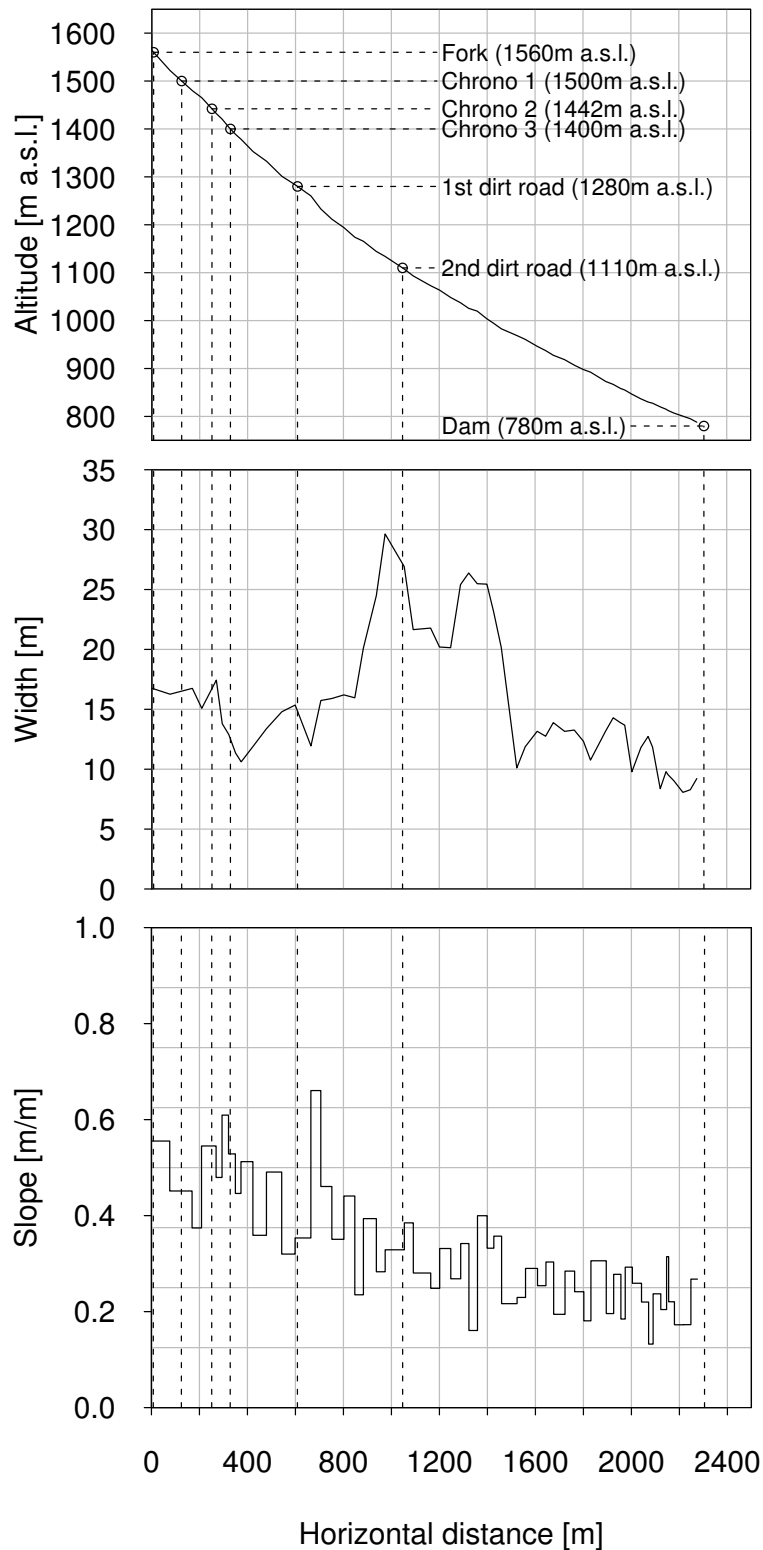


Figure 5.11: The altimetric profile of the channel, the trend of the width and of the slope angle vs. the horizontal cumulative distance. They have been obtained through the analysis of the ortho-photo, of the DEM and of the Provincial Technical Map.

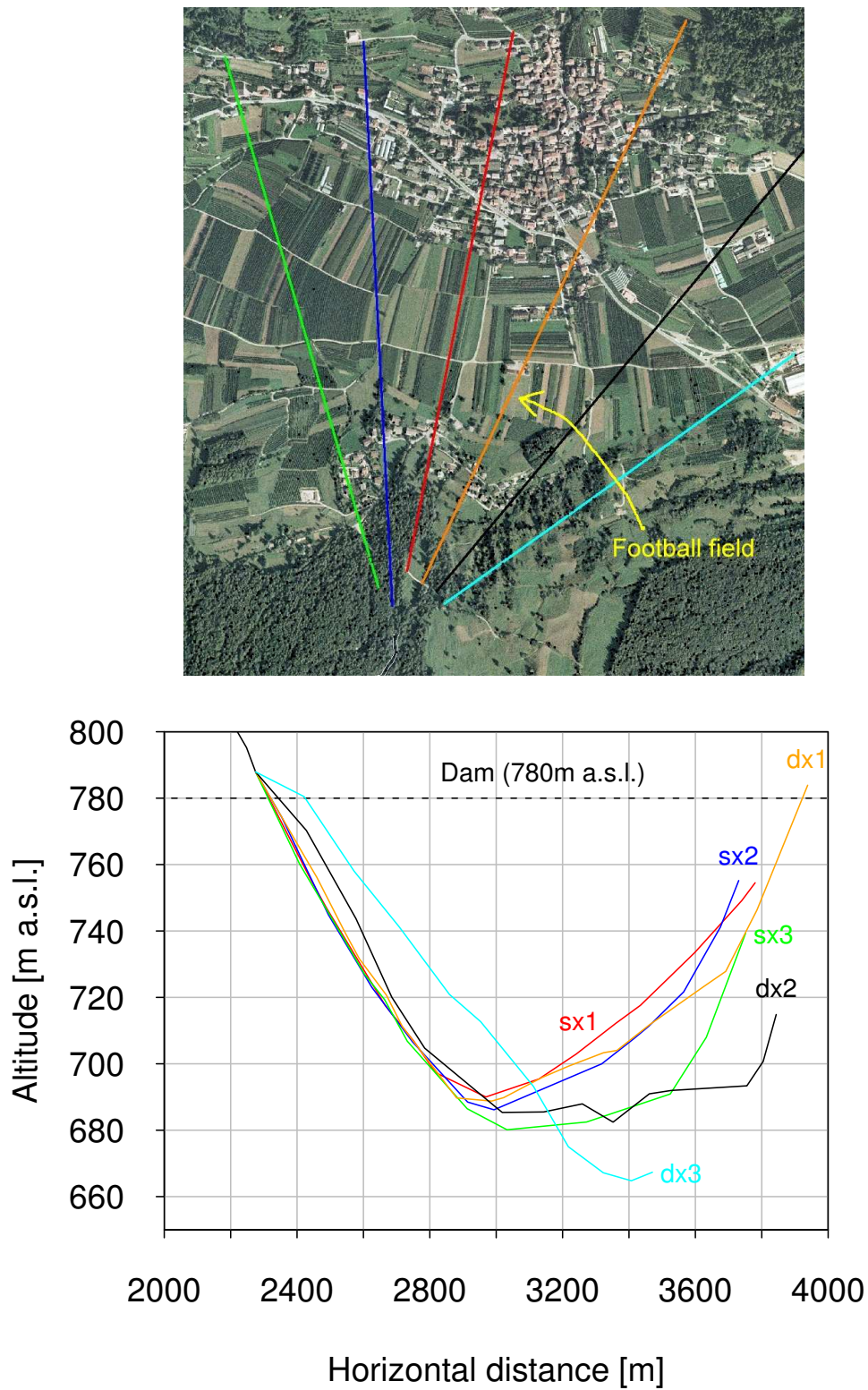


Figure 5.12: 6 different paths of the avalanche on the alluvial fan, used for the numerical simulations. Plan view and altimetric profiles

5.4 Monitoring of avalanche activity

The avalanche site of Lavina Granda has been equipped with instruments suitable for the evaluation of the flow depth and of the velocity along the channel and for the estimation of the snow depth and of the avalanche paths in the two sub-catchments. Two topographic surveys (a quick one and a detailed one) have been executed in snowy conditions and during the summer. During winter seasons 2003–2004 and 2004–2005 several events have been observed, allowing to characterize the behaviour of snow avalanches in Lavina Granda channel.

5.4.1 Field instrumentations

Two graduated 3.5 m-high poles have been placed in the two sub-catchments (Figure 5.13) in order to evaluate the snow depth in the starting zone. The poles have been located on low-slope places, safe from the risk of damages caused by snow movements. A SWAROVSKI AT80 spotting scope, equipped with a 800× HABICHT ST/CT photo-adaptor for a NIKON F4s 35 mm camera, has been used to observe and photograph the two poles from far away.

In order to monitor the avalanche activities in the starting zone, 42 coloured and numbered cubic wooden tracers, with the side 15 cm long, have been spread in the sub-catchments (Figure 5.14). Their initial position was measured by means of a PROMARK2



Figure 5.13: The two graduated poles, located in the two sub-catchments in order to estimate the snow depth in the starting zone (October 29th 2002).

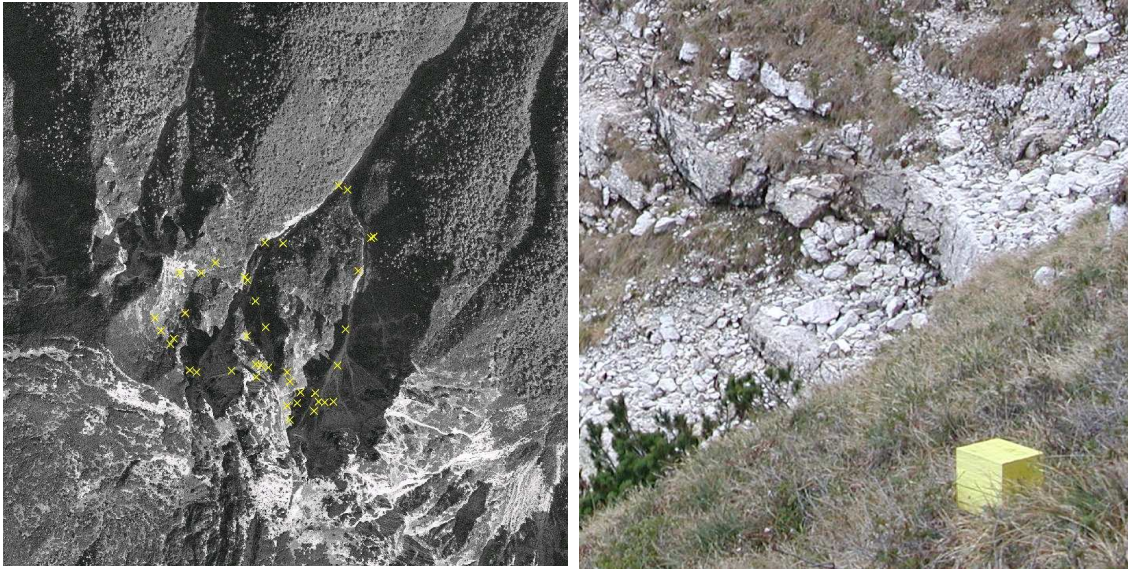


Figure 5.14: The coloured tracers, spread over the two sub-catchments in order to monitor the avalanches flowing paths (October 29th 2002).

GPS survey system. The survey of their final position, after snow melting, gives the chance to identify the channels mainly affected by the avalanche activity.

Three chronographs CASIO stopwatch HS-5 have been placed along the channel in order to measure the flowing velocities, at the altitudes of 1500 m a.s.l. , 1442 m a.s.l. and 1400 m a.s.l. , having reciprocal distances of 139 m and 85 m (see Figure 5.15). Each chronograph is contained in a box, located in safe position on the side of the channel. The chronograph is connected to a wooden cross placed in the center of the channel, through a nylon thread, 0.35 mm thick and having a yield load of 11 kg , and an iron wire, 1.5 mm thick. When the avalanche passes, it pulls down the wooden cross, drags the iron wire and tears the nylon wire, starting the chronograph up. The time interval between two subsequent chronographs is used to assess the velocity, given the distance.

A flowing depth measuring section has been equipped at the second chronograph (see Figure 5.16). An iron cable, 6 mm thick, has been hung out across the section and 8 numbered wooden saddles, having a side of 15 cm , have been hung at the cable at different heights from the bottom, through a nylon thread 0.35 mm thick. At the avalanche passage, lower saddles are removed, and the remaining ones allow to estimate the flowing depth.

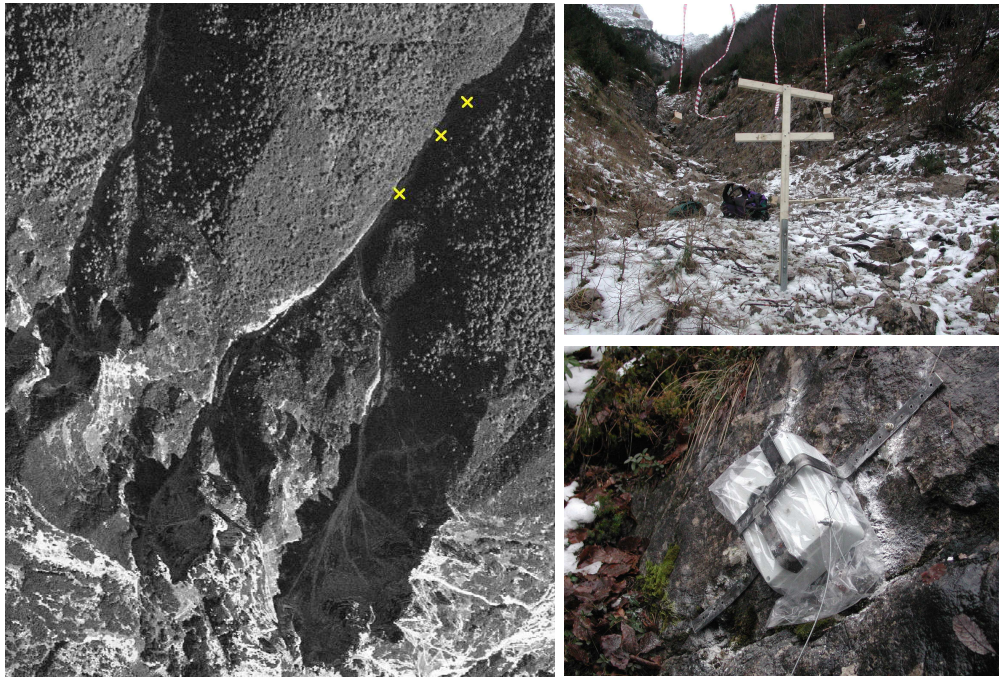


Figure 5.15: The chronographs placed along the channel in order to measure the avalanches flowing velocity (December 6th 2002).

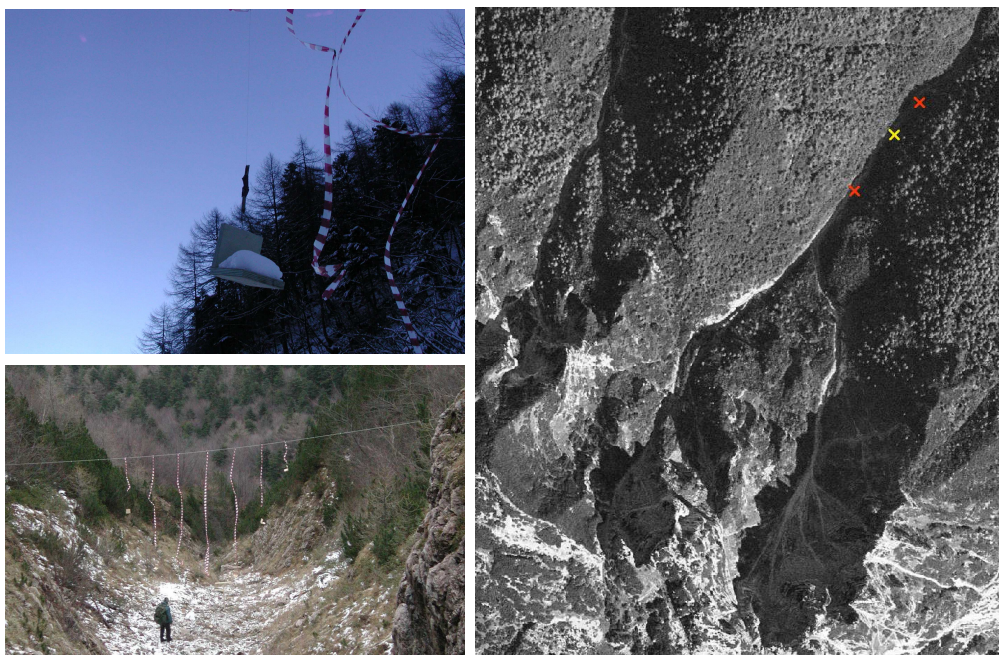


Figure 5.16: The flowing depth measuring section equipped at the second chronograph (December 6th and 18th 2002).

5.4.2 The topographic surveys

The detailed topographic surveys

Two detailed topographical surveys of the Lavana Granda channel, in winter and summer conditions, have been carried out in 2004. They have been performed by means of a theodolite LEICA TCR 705 (see Figure 5.17) and a target pole. Measures of inclined distances, azimuth angles and zenith distances have been taken, with declared standard deviations of $5''$ of sexagesimal degrees on angular measures and 10 mm on distance measures. The deposit of the avalanche occurred on December 2003 has been surveyed on February 6th 2004. 287 points, shown in Figure 5.18, have been surveyed on the surface of the avalanche deposit, with a station point on the dirt road at the altitude of 1110 m a.s.l. . On July 29th, the same segment of the channel has been surveyed, in order to reconstruct the topography of the channel. Two station points were necessary, because problems of points inter-visibility arised, due to the vegetation. 253 points have been measured.

By comparing the Digital Elevation Model of the bottom surface and of the snow cover surface, deduced from the elaboration of the data of the two surveys, it was possible to define the snow depth distribution of the deposit, represented in Figure 5.18. The final volume of the deposit has been assessed, providing a value of 5050 m^3 . It is noticeable that the avalanche deposited considerable volumes of snow also along the channel.

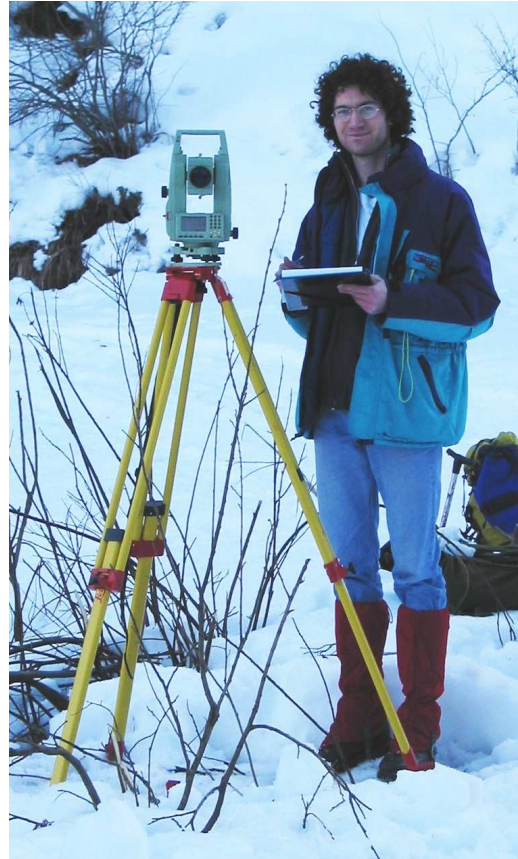


Figure 5.17: The theodolite for the measure of inclined distances, zenith angles and azimuth distances.

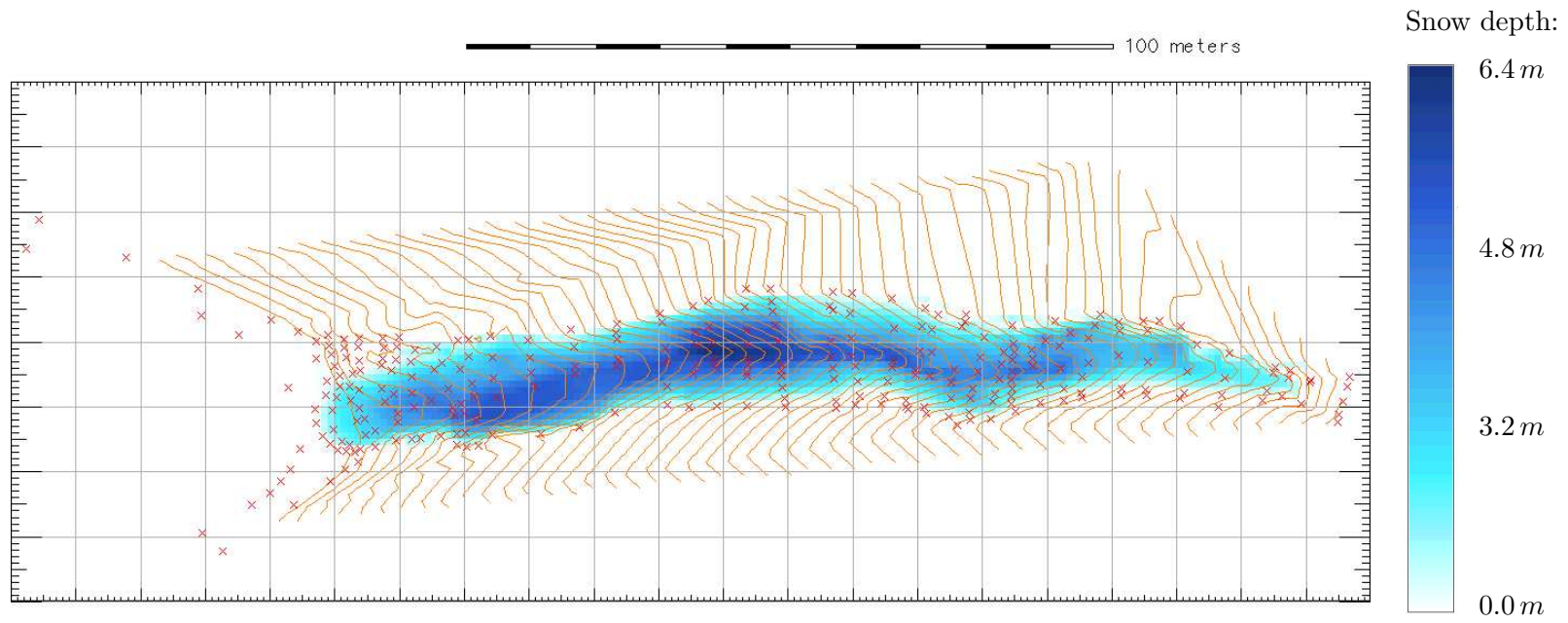


Figure 5.18: The snow depth distribution, obtained through the elaboration of the data of the two detailed topographic surveys, carried out along the segment of the Lavina Granda channel, above the lower dirt road at the altitude of 1110 m a.s.l. . The points of the winter topographic survey are represented through red crosses. The contour lines derive from the Digital Terrain Model obtained from the summer survey.

The quick topographic survey

The topographic survey of Lavina Granda snow avalanche channel, in Vigolana range, near Trento, has been carried out also by means of a quick procedure, using a laser distance-meter LEICA DISTO BASIC, a compass and clinometer SILVA CLINOMASTER. This quick and simple procedure has been chosen in order to obtain a sufficiently approximated representation of the channel, both in winter and in summer conditions. Adoption of more precise and more complicated methods proved to be unsuitable (GPS methods showed inappropriate, due to frequent lack of a sufficient number of satellites; theodolite based procedure demonstrated time expending and difficult to perform due to high slope and instrument heaviness) or too expensive (aerial photogrammetric techniques).

In Figure 5.21 is represented, on the left, the horizontal plane through the station point P_i . The angle on the horizontal plane is measured by means of a compass (Figure 5.23, on the left). On the right side of the same figure is represented the vertical plane through two station points P_i and P_{i+1} , belonging to the thalweg of the avalanche channel. The angle on the vertical plane between the azimuth and the direction defined by the line passing through P_i and P_{i+1} is measured by a clinometer (Figure 5.23, on the right). Practise allows to measure angles with a precision of 0.5 sexagesimal degrees. The measurement of the distance between the station points P_i and P_{i+1} is obtained using a laser distancemeter suitable for distances smaller than 100 m. The precision of distance measurement is around 10 cm, independently of weather conditions.



Figure 5.19: The comparison between the morphology of the channel at the end of the autumn (December 18th 2002) and after the passage of an avalanche (January 16th 2004), in the segment between the intermediate and the upper chronographs.



Figure 5.20: The comparison between the morphology of the channel in autumnal conditions (November 5th 2004) and in snowy conditions (January 2nd 2005), about the cliffs just below the lower chronograph.

The survey of cross sections is performed as showed in Figure 5.22, using the same implements described above. The segment of Lavina Granda channel between the fork at the altitude of 1560 and the lower dirt road at the altitude of 1110 *m a.s.l.* has been surveyed. A first survey was carried out on May 21th 2004, when the channel was filled by the deposits of previous avalanches. A second survey was performed when the terrain was free from the snow, on July 29th. In Figure 5.24 is reported a 3-D view of the bottom survey carried out on July 29th 2004. In Figure 5.25 are shown the bottom slope profiles along the avalanche channel, given by the cited spring and summer surveys.

The analysis of the mean slope and the standard deviation provides interesting results. The mean slope for the two surveys is nearly the same: 0.438 *m/m* for the spring survey versus 0.427 for the summer survey. Standard deviation passes from 0.082 *m/m* for the survey of May, to 0.107 *m/m* for the survey of July. The reason is that the avalanche, during its motion, fills the concave segments and reduces the curvature of the channel. The morphology of the channel is completely different in winter and summer conditions, as can be observed in Figure 5.19 and Figure 5.20. The modified roughness and geometry of the channel explain the smaller resistance offered to the flow of following avalanches, as observed during the winter surveys to the site.

In Figure 5.26 is reported the channel slope trend as function of the horizontal distance, obtained through the elaboration of data extracted from the Digital Elevation Model of the Autonomous Province of Trento. It differs significantly from the slope profile relevant to the summer survey, even if the mean slope (0.419 *m/m*) and the standard deviation

(0.123 m/m) are quite similar.

The quick survey demonstrated effective to draw the profile of the channel in different snow cover conditions. When long segment are surveyed, in order to limit error propagation, it's necessary to fix the survey to some topographical intermediate points, measured through more precise procedures. The survey can get more accurate and reliable volume assessments can be derived.

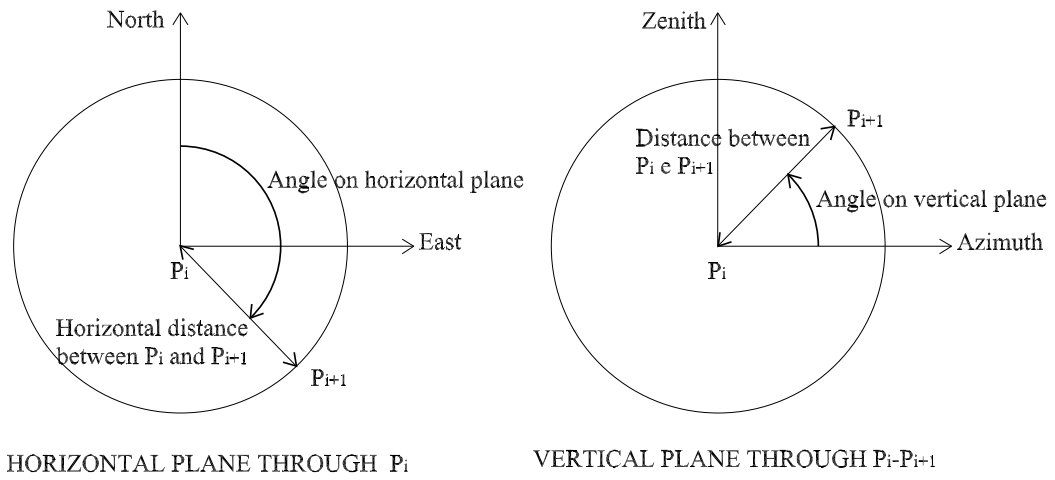


Figure 5.21: Survey of distance between two points on the thalweg is performed by means of a laser distancemeter; the measurement of the angle on the vertical plane is performed by means of a clinometer; the angle on the horizontal plane is measured by means of a compass.

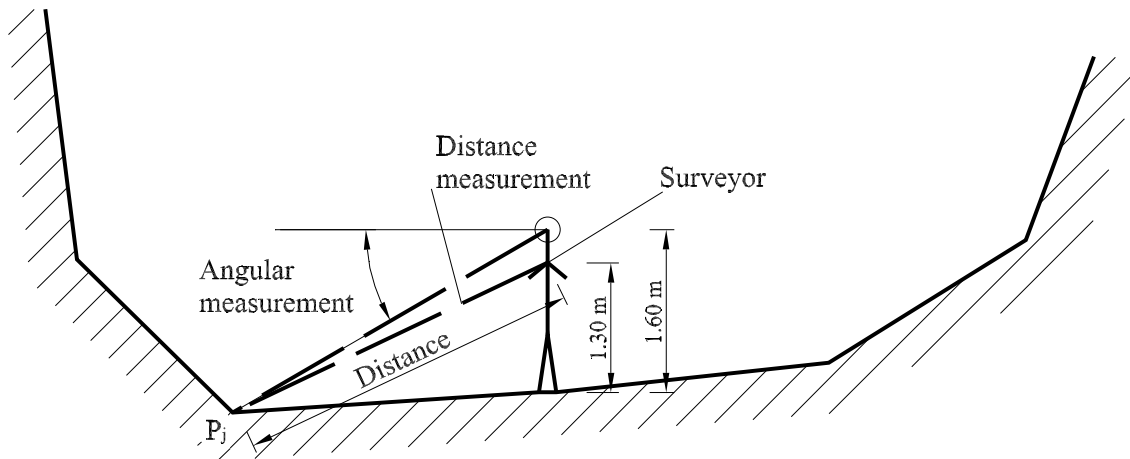


Figure 5.22: Survey of the cross-sections, performed by means of a laser distancemeter and of a clinometer.



Figure 5.23: Compass (on the left) and clinometer (on the right) for the measure of the angle on the horizontal plane (Figure 5.21, on the left) and the angle on the vertical plane (Figure 5.21, on the right).

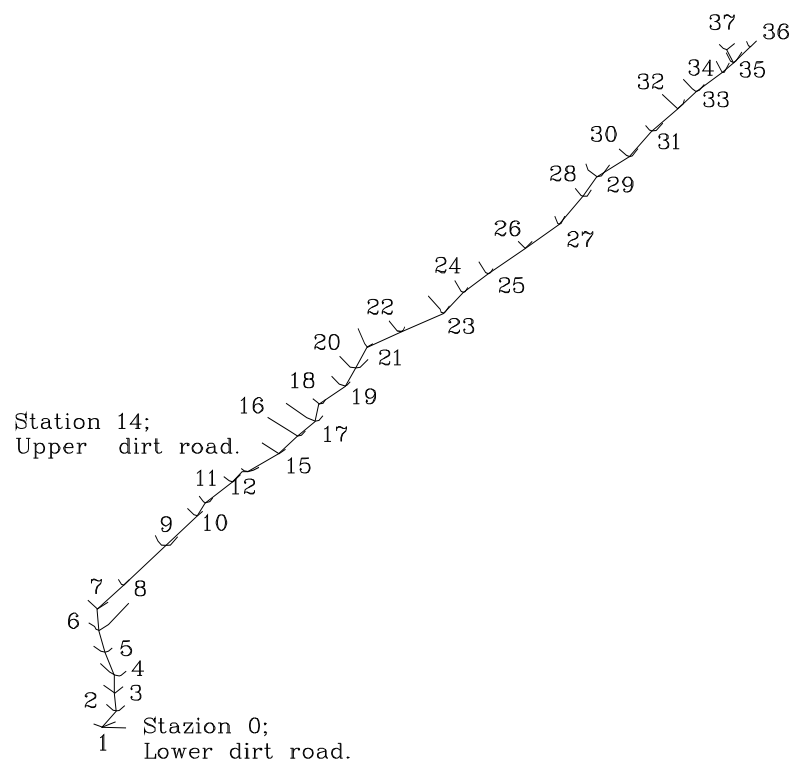


Figure 5.24: A 3-D view of Lavina Granda bottom survey, realised on July 29th 2004.

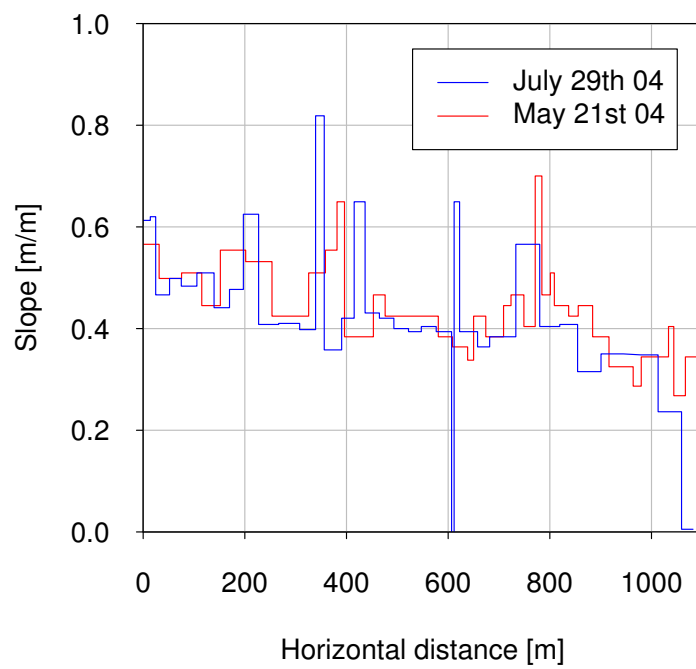


Figure 5.25: Slope profiles along the Lavina Granda avalanche channel, in the case of the summer survey (July 29th 2004) and in the case of the winter survey (May 21st 2004).

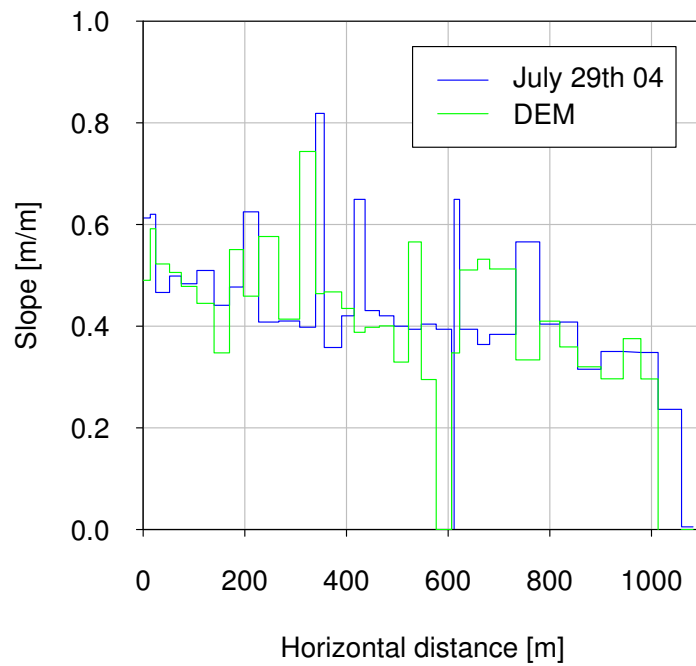


Figure 5.26: Comparison of the slope profiles along the Lavina Granda avalanche channel, obtained from the summer survey (July 29th 2004) and the Digital Elevation Model (DEM).

5.4.3 Surveyed events

Winter season 2002–2003

No avalanche reached the equipped sections of the channel during the winter season 2002–2003. The maximum snow depth measured along the channel was 50 *cm*.

Summer season 2003

During the summer 2003 a debris flow came down along the channel. On the 24th of June an intense precipitation (rain mixed with hail) affected the area. During 2 hours, 35 *mm* of equivalent water fell at Vigolo Vattaro, to the north of the channel. The granular material of the debris flow was poor of fine fraction and had mean diameter of 10 *cm*.

Several channels contributed to feed the debris flow. In Figure 5.27 is shown the morphological modification induced by the debris flow in the starting zone.

By measuring the final positions of the recovered wooden tracers, it was possible to identify the feeding areas and the paths of the debris flow, shown in Figure 5.30.

Through the chronographs, a velocity of 5–6 *m/s* was measured. The debris flow reached the dam at the end of the channel, at the altitude of 780 *ma.s.l.*. A final deposit volume of 500 *m*³ was estimated, but considerable depositions took place along the channel (see Figure 5.28 and Figure 5.29).



Figure 5.27: The morphologic evolution in the initiation zone of the debris flow. The two images show the same channel in autumn 2002 (October 29th 2002) and in summer 2003 (July 18th 2003).



Figure 5.28: An intermediate deposit of the debris flow, at the intersection between the channel and the dirt road at the altitude of 1280 *m a.s.l.* (August 10th 2003).



Figure 5.29: Erosion and lateral depositions due to the debris flow along the channel (July 18th 2003).

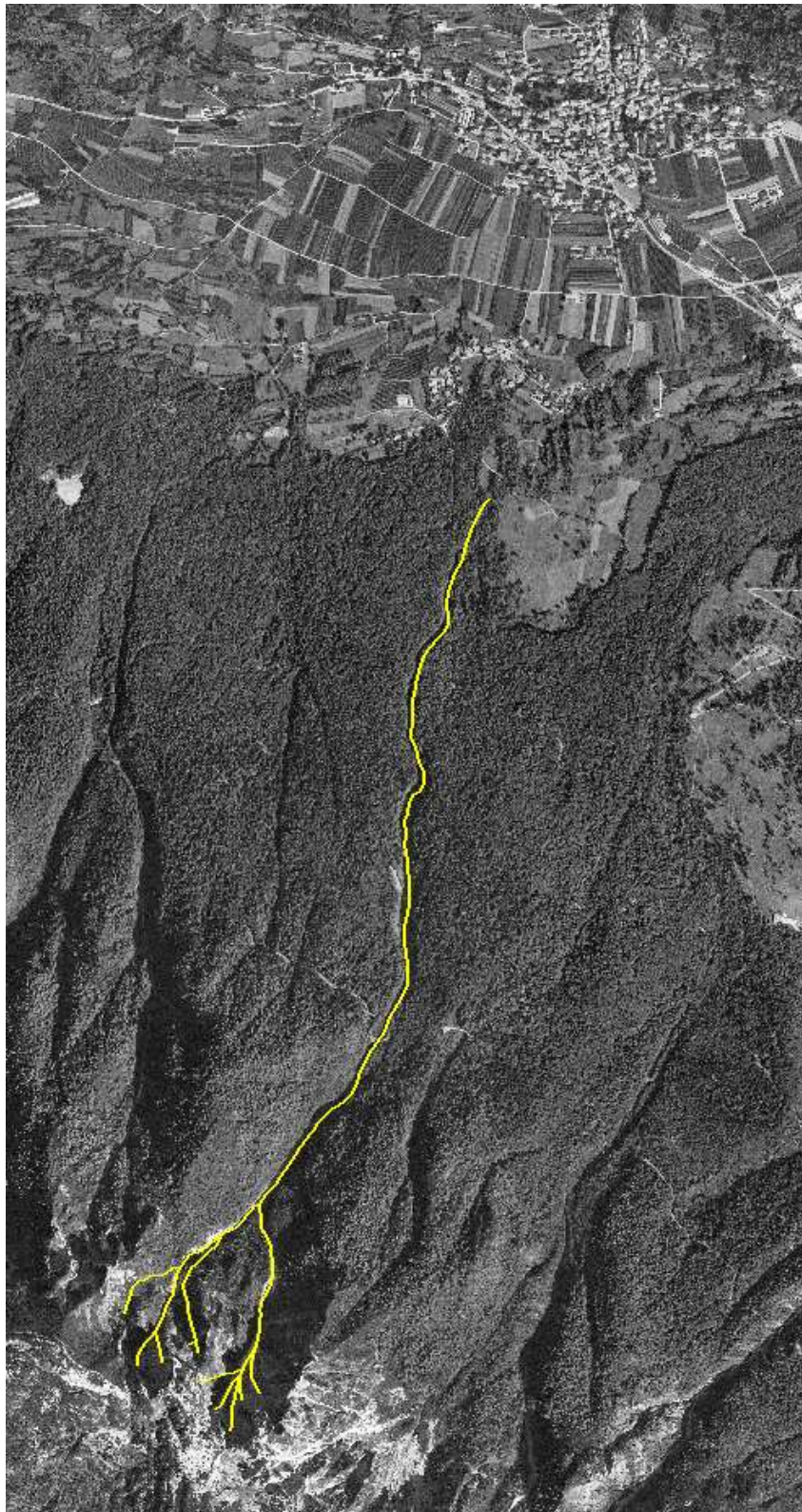


Figure 5.30: The feeding areas and the paths of the debris flow of the summer 2003.

Winter season 2003–2004

In order to avoid the tracers being moved by other phenomena (like intense floods or debris flows), and to prevent the tracers from being frozen to the ground, the best period to place the tracers is after a small snowfall. Because of the entity of the first snow precipitation, it was impossible to replace the tracers moved by the debris flow. This precluded the possibility to monitor the avalanche activity in the catchment.

During the winter season 2003–2004, 4 avalanches have been surveyed in the Lavina Granda site. The positions of the final deposits for the 4 events are reported with different colours in Figure 5.39.

The first event occurred on December 2003. From 70 to 80 *cm* of fresh snow fell in three days, from the 29th to the 31st of December of 2003 at the snow–weather stations of Sommo Pass and Bondone Mount. The avalanche was first surveyed on the 1st of January of 2004, from far away. It was a loose granular avalanche, induced by the overload of fresh snow. It reached the intersection of the channel with the dirt road at the altitude of 1110 *m a.s.l.*. The final deposit, shown in Figure 5.31, was 6–7 *m* deep, 15 *m* wide and 150 *m* long, with an estimated volume of 13000 *m*³. The maximum flowing depth was of 7–8 *m*, as can be seen from Figure 5.32. No measure of velocity has been taken because

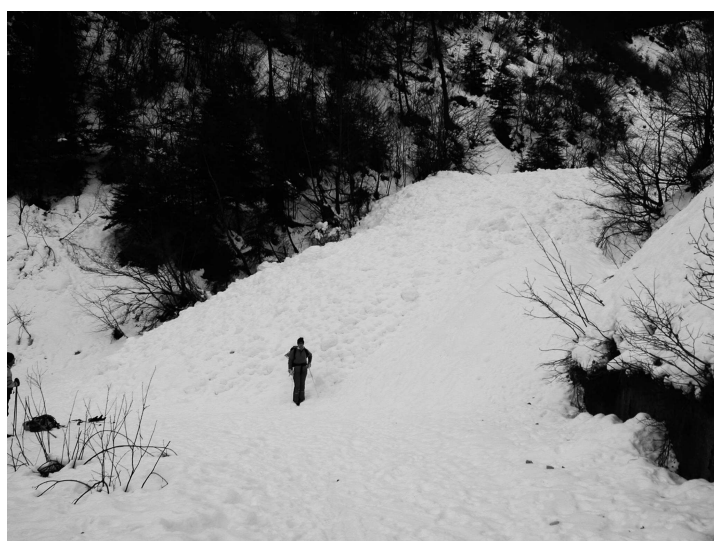


Figure 5.31: The final deposit of the avalanche that occurred on December of 2003, at the altitude of 1110 *m a.s.l.* (January 16th 2004).

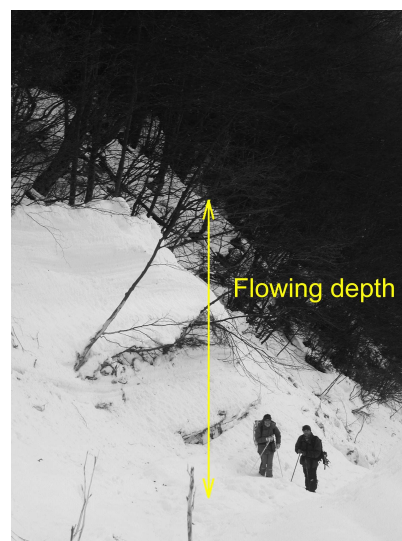


Figure 5.32: The maximum flowing depth for the granular avalanche occurred on December (photo taken on January 16th 2004).

of a malfunction of the chronographs.

On February 2004 a second granular avalanche took place. The only recorded precipitation occurred on January 19th 2004. 14 *cm* and 24 *cm* of fresh snow were surveyed at Bondone Mount and Sommo Pass snow–weather stations respectively. The avalanche was smaller than the preceding one and reached the upper intersection of the channel with the dirt road at the altitude of 1280 *m a.s.l.*. It mobilised the partially linked snow particles deposited along the channel during the previous event and big particle clusters (with diameter up to 1 *m*) characterized the final deposit. No image or quantitative datum is available, because of the high risk of access to the channel.

Between the 11th and the 12th of March 2004, 90–100 *cm* of fresh snow fell, and a powder avalanche occurred. The signs of the avalanche, among which the tree debris (see Figure 5.33), were recognizable up to the altitude of 870 *m a.s.l.*, just above the dam. The effects of the powder avalanche on the forest at the side of the channel, shown in Figure 5.34, have been found below the third chronograph, at the altitude of 1400 *m a.s.l.*. In our opinion, it was the dense core of the powder avalanche that tore the iron cable at the flowing depth measuring section (see Figure 5.35). Another powder avalanche came down along the Lavinella, a channel on the right orographic side of Lavina Granda (Figure 5.36): several plants of beech have been uprooted in the runout zone (Figure 5.37), at the altitude of 1250 *m a.s.l.*. The avalanche site of Lavinella is identified by the code 04312 on the Avalanche Register. It's characterized by rare events. The last and only



Figure 5.33: The tree debris transported by the powder avalanche. Entire plants have been uprooted (May 12th 2004).



Figure 5.34: The signs of the powder avalanche on the left side of the channel, opposite the third chronograph, at the altitude of 1400 *m a.s.l.*. All the trees are bended downstream (March 21st 2004).



Figure 5.35: The two edges of the iron cable, torn by the powder avalanche at the flowing depth measuring section, in the Lavina Granda channel (May 12th 2004).

recorded event took place on the 31st of January of 1986. The avalanche reached the same altitude and uprooted 80000 *kg* of beech trees.

From the 3th of May to the 6th of May an intense precipitation occurred, characterized by a water equivalent of 115 *mm* and 99 *mm* at the weather stations of Bondone and Sommo Pass. It was followed by a storm on May 8th. No snowfall data are available for this period. On the 12th of May, during an inspection to the channel, a new granular deposit, shown in Figure 5.38, was found. It was located at the altitude of 1290 *m a.s.l.* and was characterized by particles with diameters varying from 5 *cm* to 100 *cm*, the biggest particles being concentrated on the front of the deposit.

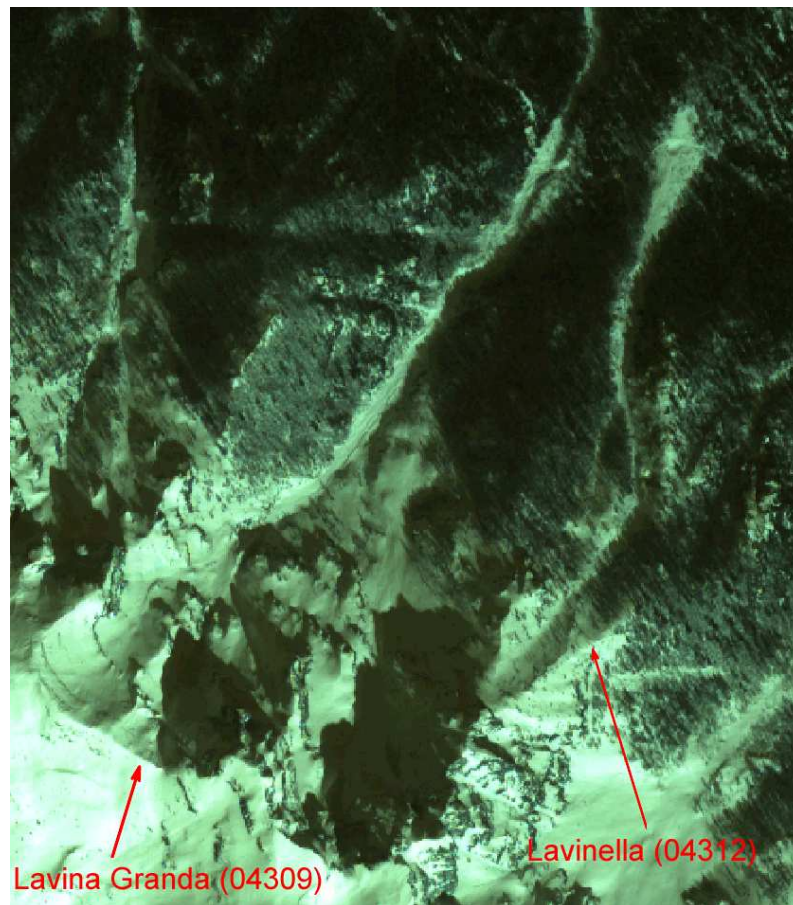


Figure 5.36: A satellite image, dated March 30th 2004, where are recognizable the area interested by the powder avalanches in Lavina Granda and Lavinella sites.



Figure 5.37: The runout zone of the avalanche that occurred in the Lavinella channel. In the background the uprooted beech plants are recognizable (March 21st 2004).



Figure 5.38: The final granular deposit of the avalanche that flew down at the beginning of May of 2004 (May 12th 2004).

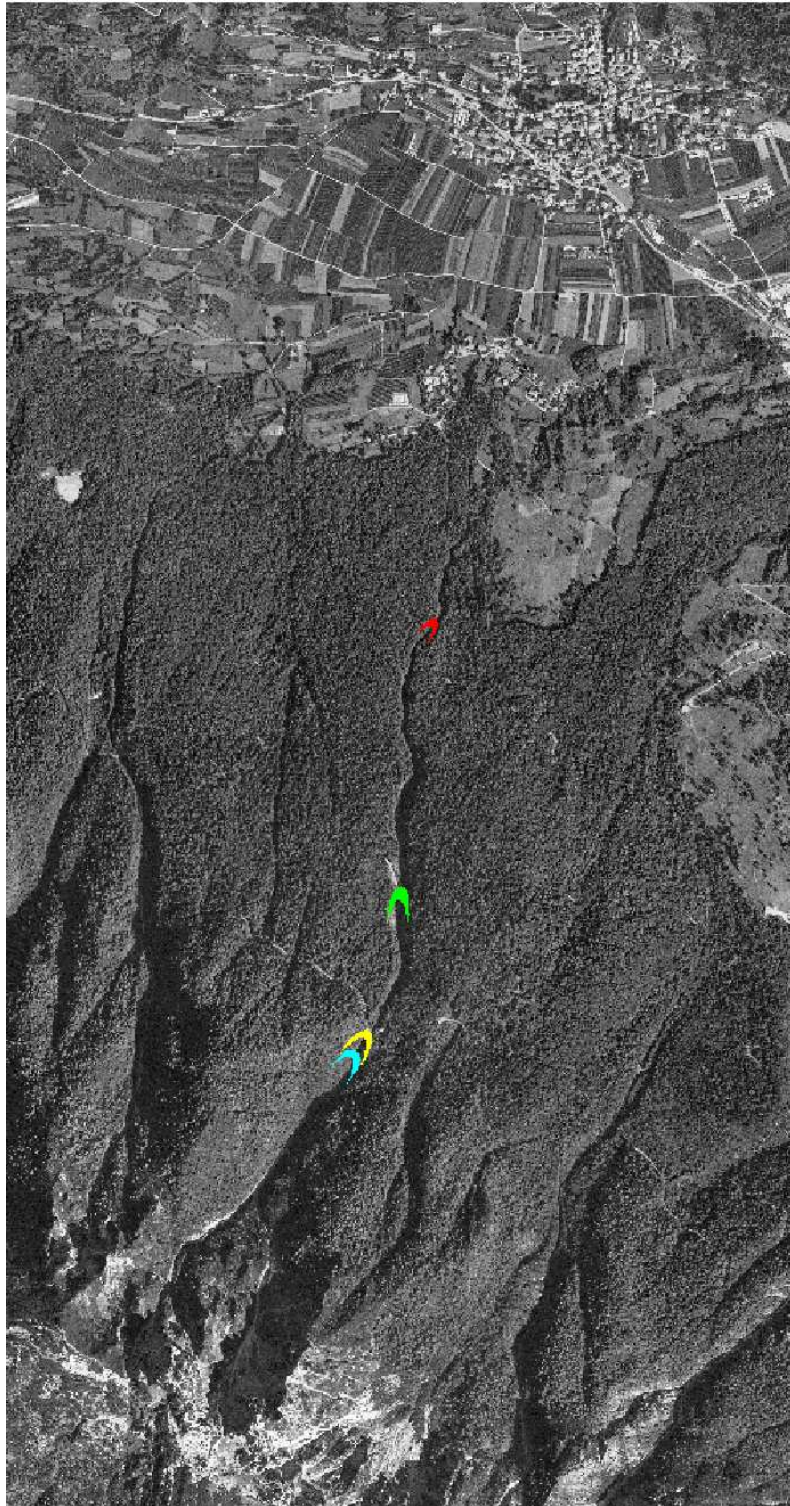


Figure 5.39: The locations of the final deposits of the 4 avalanches occurred during the winter season 2003–2004. In green the granular avalanche of December 2003; in yellow the granular avalanche of February 2004; in red the powder avalanche of March 2004; in cyan the granular avalanche of May 2004.

Autumn–winter 2004–2005

During the autumn 2004, in the night between the 1st and the 2nd of November, during a violent storm, 88 *mm* of rain fell in 11 hours, following two smaller events of 33.6 *mm* and 30.4 *mm*. A debris flow took place in the channel and modified the bed morphology. One deposit formed just over the section of the intermediate chronograph (see Figure 5.40). Big boulders, having diameters of over 1 *m*, occupied the front of the deposit. Other erosion and deposition areas are recognizable along all the channel, up to the lower dirt road (altitude 1110 *m a.s.l.*). In Figure 5.41 is shown the sliding surface of a rotational ground failure that occurred at the base of the road: an erosional mechanism that was found in several other points along the channel.

After an abrupt drop in the temperatures, a first snowfall took place between the 10th and the 11th of November. 30 *cm* and 43 *cm* of fresh snow fell at Bondone Mount and Sommo Pass respectively. A following period of high temperatures caused the snow cover consolidation. A second snowfall occurred between the 30th of November and the 1st of December of 2004. The overload due to the new supplies of fresh snow (38 *cm* at Sommo Pass and 30 *cm* at Bondone Mount), induced the starting of slab avalanches in several points in the right sub-catchment of Lavina Granda (see Figure 5.42). A granular avalanche formed and went over the first dirt road, stopping at the altitude of 1250 *m a.s.l.*, where the channel gets narrower and steeper. The snowballs in the granular deposit had



Figure 5.40: The debris flow deposit that formed opposite the intermediate chronograph during the event of the November 2004 (November 5th 2004).



Figure 5.41: A rotational ground failure at the base of the dirt road at the altitude of 1110 *m a.s.l.*, occurred during the debris flow event of the November 2004 (November 5th 2004).

diameters ranging between 1 *cm* and 20 *cm*, with peaks of 50 *cm*. During the survey of the initiation zone, carried out on December 12th 2004, in several places the fracture lines of still untriggered slab avalanches were recognizable (see Figure 5.43). When the avalanche occurred, only two chronographs were equipped: the intermediate and the lower one. The two chronographs were started by the avalanche. The estimated time interval was of 27 *s*, that means a velocity of 3 *m/s* over a distance of 85 *m*. The measured velocity is very low, but the shape of depositions along the channel suggests that a stop could have occurred between the two chronographs, due to the low inertia of the mass and to the high resistance offered by the bed roughness. In particular a transversal trench, left by the debris flow just above the second chronograph, is the supposed reason for the intermediate stop of the avalanche. In the same section the avalanche deposit showed a similar transversal cut.

The precipitation of the end of November was followed by hot winds from south–west,



Figure 5.42: The crown fractures of two slab avalanches, started in the right sub-catchment. In the lower picture the graduated pole is recognizable (December 12th 2004).

Figure 5.43: The fracture line of a slab avalanche not still triggered (December 12th 2004).

driven by a strong depression in Spain. The high temperatures caused a quick snow metamorphism and consolidation, the formation of slabs in the starting zone and the aggregation of the particles of the first avalanche deposit.

Another intense snowfall occurred on December 26th and 27th (49 *cm* and 41 *cm* of fresh snow respectively at Sommo Pass and Bondone Mount snow stations), followed by strong winds from north, which formed considerable snow drift deposits. A second granular avalanche occurred, arriving a little above the second dirt road (see Figure 5.49). It was likely a slab avalanche: the crown of a slab could be guessed from far away in the right sub-catchment. The avalanche removed the first avalanche deposit and the aggregates of the first avalanche deposit are still recognizable in the new deposit (see Figure 5.44). This time, the segment of the channel opposite to the last chronograph (shown in Figure 5.45) and the one by the higher dirt road (1280 *m a.s.l.*) were full sliding segments. At the higher dirt road the flow was about 3 *m* deep, as shown in Figure 5.47, and released laterally a bank with sub-vertical smooth internal surface and the external face inclined at an angle equal to the internal friction angle ϕ on the horizontal (Figure 5.46). The estimated ϕ is $37^\circ \pm 2^\circ$. In most of the events, the presence of lateral banks left by granular avalanches is observable, where the section gets wide or the channel curves.

The granular intermediate depositions along the channel showed interesting phenomena of slab-type yield on a very smooth sliding surface (Figure 5.48). The corresponding bottom friction angle δ should be very low.

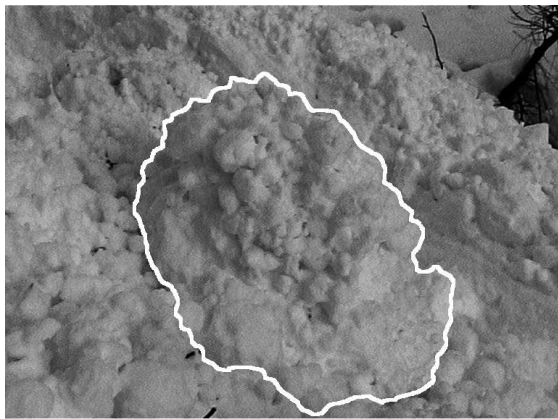


Figure 5.44: Aggregate of particles of a previous deposit, entrained but not broken up by the avalanche of the end of December (January 2nd 2005).



Figure 5.45: The full sliding sections at the lower chronograph (January 2nd 2005).

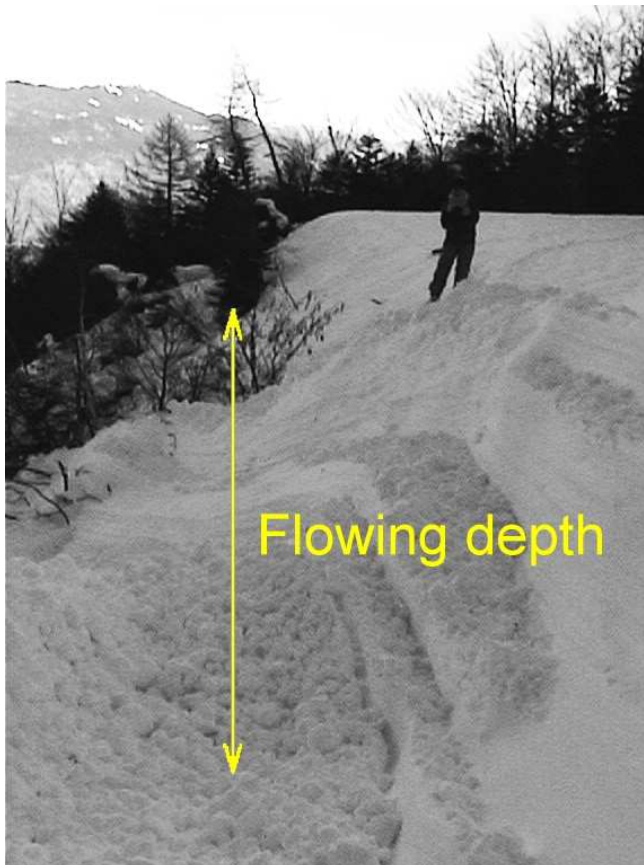


Figure 5.47: The sub-vertical smooth lateral bank left by the avalanche at the upper dirt road 1280 *m a.s.l.*. The flowing depth is about 3 *m* (January 2nd 2005).



Figure 5.46: The external face of the lateral bank, inclined at ϕ on the horizontal (January 2nd 2005).

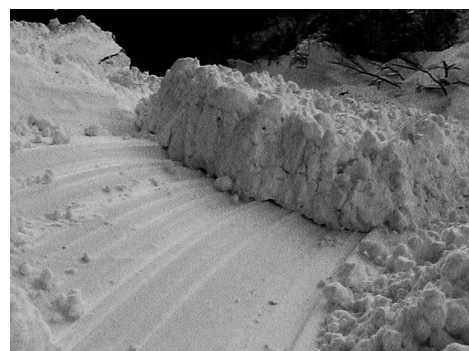


Figure 5.48: A slab-type movement of the granular material deposited by the avalanche along the channel. The smooth sliding bottom appears on the surface (January 2nd 2005).

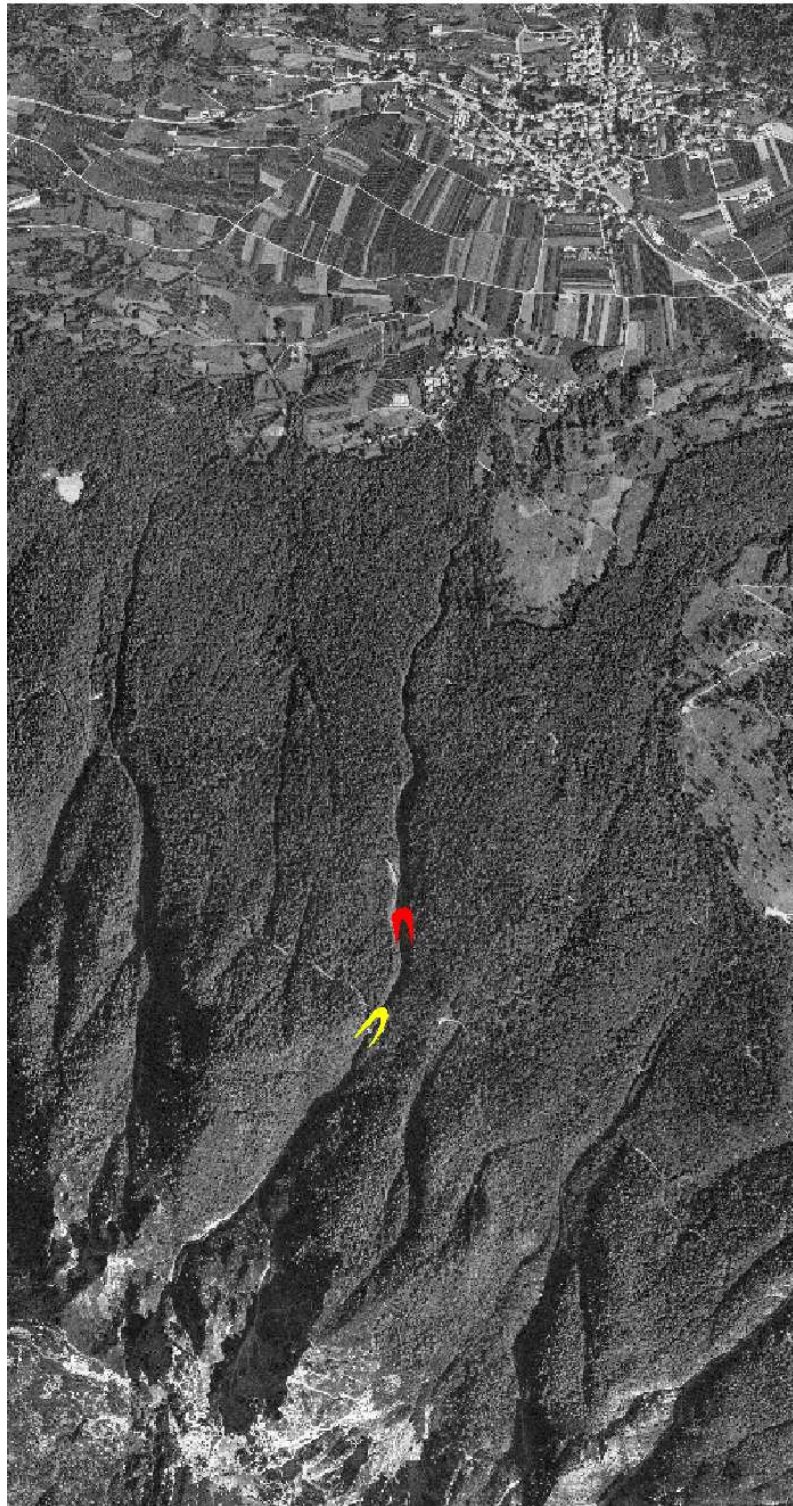


Figure 5.49: The locations of the final deposits of the 2 avalanches occurred during the winter season 2004–2005. In yellow the granular avalanche of the beginning of December 2004; in red the granular avalanche of the end of December 2004.

5.5 Final considerations

During two years of surveys at the Lavina Granda Valley, we have collected a large amount of qualitative and quantitative data about the behaviour of the avalanches occurring in the site.

The feature that more arises is the great variability of the initial and boundary conditions and of the events which took place in the Lavina Granda channel. The definition of the initial snowcover depth, that can be carried out through statistical analysis, is likely one of the smallest causes of uncertainty. The area that can potentially feed the avalanche is very large, but various sub-catchments contribute following different detachment mechanisms, which normally do not apply simultaneously. Nevertheless, the hypothesis of a crisis of the system that involves the entire area cannot be excluded a priori.

Another considerable source of uncertainty is the ratio between the initial density of the snowcover and the density of the flowing mass. The snowcover features (stratification, density, resistance, type of links between snow grains) and the detachment conditions determine the type of avalanche (wet dense avalanche, dry dense avalanche, powder avalanche) that can evolve during the motion, depending on the topography of the channel and on the properties of the deposits of preceding events. Indeed, these deposits can strongly modify the morphology and the roughness of the channel and can be incorporated by the flowing avalanche, affecting its dynamic.

In the campaign of numerical simulations in design, all these uncertainty factors have to be considered in order to reconstruct all the possible scenarios. Nevertheless, making a statistical analysis on such data to assign a return period to each simulated event is a barely meaningful task, because of the difficulty to evaluate the uncertainty level of the initial conditions.

6 Concluding remarks

In this thesis the one-dimensional model with variable width *1dwvar* for the simulation of confined granular avalanches has been presented. It is based on the theory of Savage and Hutter (27) for granular material, modified in order to represent the stresses between the flowing avalanche and the vertical side walls. The model has been applied to experimental cases with constant width, in order to test the original rheological hypotheses. The back calculation of the experiments through the *1dwvar* model gave noticeably better results than the basic constant width model, *1d*, where the interaction of the avalanche with the lateral wall was simply treated by applying a corrective term to the bottom friction angle δ . A campaign of experimental tests is in design at the Hydraulic Laboratory of the University of Trento, in order to thoroughly investigate the behaviour of the *1dwvar* model with respect to cases where the width of the channel is longitudinally varying and the lateral friction angle is known.

The two-dimensional model, developed at the Department of Civil and Environmental Engineering of the University of Trento by the writer, has been improved, by allowing the rotation of the absolute coordinate system. The “plug-flow” assumption and the hypothesis of hydrostatic pressure distribution along the direction z of the rotated coordinate system is better fulfilled where the outward normal to the bottom surface is better approximated by z . Nevertheless, in this way, only limited area of the slope are well fitted by the xy coordinate plane. A possible solution could be to change the orientation of the absolute coordinate system in order to fit the areas covered by the flowing mass during the subsequent phases of motion. A different approach has been proposed recently by Zwinger et al. (35). They integrate the momentum equation for each node in a local ortho-normal coordinate system relevant to velocity vector, demonstrating that the introduced error in the pressure gradient term of the momentum equation is of order $\varepsilon^{3/2}$. The two-dimensional model showed strong instabilities due to the deformation of the mesh in presence of complex topographies of the sliding surface. Re-meshing algorithms are computationally expensive and generally produce a loss of accuracy, due to the re-mapping of the field variables. It's possible to remedy to this last deficiency by applying finite volume schemes based on

the use of Voronoi cells (see Zwinger et al. (35)). We have undertaken a different way, by focusing our attention on meshless methods, where the mass is represented through a set of not connected nodes. The Moving Least Square Particle Hydrodynamics (MLSPH) scheme by Dilts (7), (8), has been applied to the one-dimensional model with constant width, in order to get indications on the advisability of its extension to the two-dimensional case. The resulting numerical model *MLSPH1d* showed less accurate and definitely more time expensive than the original model. Nevertheless the application of meshless schemes to the two-dimensional case, where the constraints imposed by the mesh are stronger, is still promising. Furthermore, new meshless methods have been recently developed, faster than the MLSPH scheme, like the normalized Smoothed Particle Hydrodynamic scheme. The application of Riemann solvers to this meshless scheme, to substitute the traditional viscosity term, source of accuracy loss, has been recently tested, as reported by Vila (33).

The avalanche site of Lavina Granda has been surveyed in order to get informations and measures relevant to the behaviour of snow confined avalanches. Simple measure devices have been installed in order to collect measures of flowing depth, of velocity, of the initial snow cover depth and to monitor the avalanche activity in the starting zone. A quick topographic survey method, suitable for the assess of involved volumes and of morphological modifications induced by the avalanche deposits, has been tested. Six avalanches occurred during two winter seasons (2003–2004 and 2004–2005), one powder avalanche and five dense granular avalanches, started as both cohesionless and slab avalanches. Mainly due to the high risk of access to the site during the winter, few quantitative measures could have been taken. Nevertheless, a great amount of qualitative observations has been collected, useful to characterise the phenomena which take place in the Lavina Granda Valley. What clearly arises is their extreme variability and the consequent uncertainty of evaluation of the possible scenarios that can occur. The evaluation of the detachment area and of the ratio between the initial density and the flowing density dramatically affects the assessment of the involved volumes. The features of the initial snowcover as well as the state of the channel (e.g. presence of more or less consolidated deposits) influence the type of flux and its evolution during the motion. Knowing the behaviour of the avalanche site, it is possible to simulate the different possible scenarios by means of a numerical model, but it's very difficult to assign them a return period.

References

- [1] M. Barberi. Bacino valanghivo della valle della mite. 1999-2001. rilievi ed osservazioni. Technical report, Studio Tecmo S.n.C, 2002.
- [2] S. Benfatto. Il sito valanghivo della lavina granda. Degree thesis, Faculty of Engineering, University of Trento, 2004–2005. Under elaboration.
- [3] E. Bertolazzi and G. Manzini. Algorithm 817 p2mesh: generic object-oriented interface between 2-d unstructured meshes and fem/fvm-based pde solvers. *ACM Transactions on Mathematical Software*, 28(1):101–132, 2002.
- [4] M. D’Accordi. Studio di un sito valanghivo: dati di campo e modellazione numerica. Degree thesis, Faculty of Engineering, University of Trento, 1998–1999.
- [5] S. De Toni. Modello matematico e numerico bidimensionale per lo studio delle valanghe di neve densa. Degree thesis, Faculty of Engineering, University of Trento, 2000–2001.
- [6] S. De Toni, P. Scotton, and E. Bertolazzi. Modello matematico e numerico bidimensionale per lo studio delle valanghe di neve densa. University of Trento, Department of Civil and Environmental Engineering, "Quaderni del Dipartimento", IDRA 2, http://www.ing.unitn.it/dica/tools/download/Quaderni/IDR_2.pdf, 2004.
- [7] G. A. Dilts. Moving-least-squares-particle hydrodynamics i. consistency and stability. *International Journal for Numerical Methods in Engineering*, 44:1115–1155, 1999.
- [8] G. A. Dilts. Moving least-squares particle hydrodynamics ii: conservation and boundaries. *International Journal for Numerical Methods in Engineering*, 48:1503–1524, 2000.

- [9] J. Gray, M. Wieland, and K. Hutter. Gravity driven free surface flow of granular avalanches over complex basal topography. *Proceedings of the Royal Society of London*, 342:573–600, 1993.
- [10] R. Greve and K. Hutter. Motion of a granular avalanches in a convex and concave curved chute: experiments and theoretical predictions. *Phil. Trans. R. Soc. Lond. A*, 342:573–600, 1993.
- [11] O. Hungr and N. Morgenstern. Experiments on the flow behaviour of granular materials at high velocity in an open channel. *Geotechnique*, 34(3):405–413, 1984.
- [12] K. Hutter, T. Koch, C. Plüss, and S. B. Savage. The dynamics of avalanches of granular materials from initiation to runout. part ii: experiments. *Acta Mechanica*, 109:127–165, 1995.
- [13] K. Hutter, M. Siegel, S. Savage, and Y. Nohguchi. Two dimensional spreading of a granular avalanche down an inclined plane. part i: Theory. *Acta Mechanica*, 100:37–68, 1993.
- [14] R. Jingold and J. Monaghan. Smoothed particle hydrodynamics: theory and application to non-spherical stars. *Monthly Notices of the Royal Astronomical Society*, 181:375–389, 1977.
- [15] G. Johnson and S. Beissel. Normalized smoothing functions for sph impact computations. *International Journal for Numerical Methods in Engineering*, 39:2725–2741, 1996.
- [16] P. Lancaster and K. Salkauskas. Surfaces generated by moving least squares methods. *Geotechnique*, 37(155):141–158, 1981.
- [17] G. Liu. *Mesh free methods: moving beyond the finite element method*. CRC Press LLC, 2002.
- [18] L. Lucy. A numerical approach to the testing of fusion process. *The Astronomical Journal*, 88:1013–1024, 1977.
- [19] D. McClung and P. Schaerer. *Manuale delle Valanghe*. Zanichelli Editore, 1996.
- [20] J. Monaghan. Smoothed particle hydrodynamics. *Annual Review of Astronomy and Astrophysics*, 30:543–574, 1992.

- [21] J. Morris. Overview of the method of smoothed particle hydrodynamics. Preprint of Arbeitsgruppe Technomathematik (ATGM) Kaiserslautern University, 1995.
- [22] L. Musner. Applicazione dei metodi numerici meshless allo studio monodimensionale delle valanghe di neve densa. Degree thesis, Faculty of Engineering, University of Trento, 2003–2003.
- [23] S. Pudasaini and K. Hutter. Rapid shear flows of dry granular masses down curved and twisted channels. *Journal of Fluid Mechanics*, 495:193–208, 2003.
- [24] P. Randles and L. Libersky. Smoothed particle hydrodynamics: some recent improvements and applications. *Computer Methods in Applied Mechanics and Engineering*, 139:375–408, 1996.
- [25] B. Salm, A. Burkard, and H. Gubler. Berechnung von fließlawinen, eine anleitung für praktiker mit beispielen. Technical Report 47, Mitteilungen des Eidgenössischen Institutes für Schnee und Lawinenforschung, Davos, Switzerland, 1990.
- [26] J. Sanfilippo. Distribuzione della neve al suolo in Provincia di Trento. Degree thesis, Faculty of Engineering, University of Trento, 2001–2002.
- [27] S. Savage and K. Hutter. Motion of granular material down a rough incline. *Journal of Fluid Mechanics*, 199:177–215, 1989.
- [28] S. B. Savage and K. Hutter. The dynamics of avalanches of granular materials from initiation to runout. part i: analysis. *Acta Mechanica*, 86:201–223, 1991.
- [29] P. Scotton. Alcune sperimentazioni sulla dinamica di ammassi granulari lungo piani a forte pendenza. In *Atti del Convegno di Idraulica e Costruzioni Idrauliche, 1*, pages 223–234. Dipartimento di Difesa del Suolo, University of Calabria, 1990.
- [30] P. Scotton. Studio dei fenomeni valanghivi della val dei spini. (comune di pejo, trento). relazione finale. Technical report, Contract between University of Trento and Regional Council of Trento n. 3579/97-C33-N, 1998.
- [31] J. Simmonds. *A Brief on Tensor Analysis*. Springer Verlag, 1982.
- [32] S. Stoer and R. Burlisch. *Introduction to numerical analysis*. Springer Verlag, 1983.
- [33] J. Vila. On particle weighted methods and smooth particle hydrodynamics. *Mathematical Models and Methods in Applied Sciences*, 9(2):161–209, 1999.

- [34] M. Wieland, J. Gray, and K. Hutter. Channelized free–surface flow of cohesionless granular avalanches in a chute with shallow lateral curvature. *Journal of Fluid Mechanics*, 392:73–100, 1999.
- [35] T. Zwinger, A. Kluwick, and P. Sampl. Numerical simulation of dry–snow avalanche flow over natural terrain. In K. Hutter and N. Kirchner, editors, *Dynamic response of granular and porous materials under large and catastrophic deformations*, pages 161–194. Springer, Heidelberg/Berlin, 2003.